Magnetodielectric Effect and Conduction Mechanism in BFO-REMO Multiferroics

Thesis submitted in partial fulfillment of the
requirements for the degree of Doctor of Philosophy

Roberto Masso Ferret

Department of Physics
University of Puerto Rico -Rio Piedras Campus
San Juan, Puerto Rico

Submitted August 3, 2021

Magnetodielectric Effect and Conduction Mechanism in BFO-REMO Multiferroics

Accepted by the Faculty of the Doctoral Program in Chemical Physics of the University of Puerto Rico, Rio Piedras Campus, in partial fulfillment of the requirements for the degree of Doctor of Philosophy.

Dr. Ratnakar Palai

Thesis Advisor

Dr. Ram S. Katiyar

Thesis committee member

Dr. Carlos R. Cabrera

Thesis committee member

August 3, 2021

Abstract

We report herein the synthesis and suitable approach to improve the magnetoelectric (ME) coupling of Bismuth ferrite oxide (BFO) by fabrication of BFO_{1-x}-GMO_x and BFO_{1-x}-DMO_x solid solutions for $0.0 \leq x \leq 0.2$ by the auto-combustion method. The materials have been systematically characterized and examined to study the possibility of the compositional driven structural phase transition and its correlation with the ME coupling. Detail of the structural, microstructural, thermal, dielectric, ferroelectric, magnetic, magneto-dielectric, and magneto-impedance properties will be shown in the light of the bring down of magnetic ordering temperature of $BiFeO_3$ towards room temperature as a function of increasing $GdMnO_3$ and $DyMnO_3$ concentration. The dielectric and electrical properties as a function of the magnetic field indicated the signature of ME coupling in samples with increased $GdMnO_3$ and $DyMnO_3$ composition, suggesting an optimization of functional properties of lead-free doped $BiFeO_3$. In pure $BiFeO_3$ and all the combinations of BFO_{1-x}-GMO_x and BFO_{1-x}-DMO_x was found that the transport mechanism is a Space-Charge-Limited mechanism. We performed our measurements in a temperature range of 100-500K. The Fowler-Northeim Conduction Mechanism fit was used but we found that it does not describe or fit the data. The same happened with Schottky Barrier- and Pool-Frenkel fitting. We determined that the relaxation process occurring in our samples is of the kind of space charge polarization. The charge carrier density and the general density of state decreases with increasing temperature, but not the mobility of the samples, suggesting a hopping mobility type of small polaron.

Acknowledgements

I will use this opportunity to express my deep and sincerest gratitude towards my Ph.D. research supervisor Dr. Ratnakar Palai for his great guidance, invaluable support, inspiration, and encouragement during this work. Providing me with his profound insight, and scientific thinking.

I would like to express my gratitude and special thanks to Dr. Satya N. Tripathy, and Dr. Dillip K. Pradhan from the Department of Physics, National Institute of Technology (NIT), Rourkela, Odisha, India for the excellent collaborative work with our research group and for providing us with the samples used in this work. Thank you for your kindness and generosity.

I would like to express my gratitude for the excellent support, invaluable help, and suggestions of Dr. Ricardo Martinez during the last years of my work.

I am thankful to the National Science Foundation (NSF), Center for Innovation, Research and Education in Environmental Nanotechnology ($CiRe^2N$), Research in Puerto Rico (EPSCOR), Alliance for Minority Participation (AMP) and the Department of Physics for their financial assistantship during my research.

My special thanks to Dr. Ram Katiyar, Dr. Luis Fonseca, Dr. Eduardo Nicolau, and Dr. Gerardo Morell for providing their research facilities. I am deeply grateful to Dr. Carlos Cabrera, and Dr. Ram Katiyar for accepting to be in my thesis committee.

Throughout this work, I had the fortune of working with great colleagues like Fernando, Jaime, Bibek, Dr. Javier Wu, Sita, and Yamile. Thanks for your

unconditional support.

Special thanks to my girlfriend Denisse, to my great kids Roberto, and Michelle and special to my mother Gloria, and my brother Ronald for their help, encouragement and unconditional love towards me throughout these years.

Roberto Masso Ferret

List of Symbols

The following symbols are used throughout this thesis. Other symbols have been used occasionally and are introduced as needed.

Å	Angstrom
a, b, c	Lattice constants
d	Interplanar spacing
BE	Binding Energy
C	Capacitance
C_0	Capacitance with no Dielectric
E_0	External Electric Field
f, v	Frequency
h	Planck's constant
λ	Wavelength
ρ	Charge Density
θ	angle
ϕ	Spectrometer Work Function
KE	Kinetic Energy
n	Integer
ε_0	Optical or Electronic Dielectric Constant
$\varnothing_0$	Schottky Barrier
$\varnothing_t$	Trap Ionization Energy
$\varnothing_i$	Potential Barrier
m^*	Effective Electron Mass

List of Acronyms

The following acronyms are used throughout this thesis. Other acronyms have been used occasionally and are introduced as needed.

BFO	$BiFeO_3$ (Bismuth ferrite oxide)
REMO	$REMnO_3$ (Rare-earth manganese oxide)
GMO	$GdMnO_3$ (Gadolinium manganese oxide)
DMO	$DyMnO_3$ (Dysprosium manganese oxide)
BFO-GMO	BFO_{1-x}-GMO_x (BFO doped GMO)
BFO-DMO	BFO_{1-x}-DMO_x (BFO doped DMO)
a.u	Arbitrary unit
dc (DC)	Direct current
DI	Deionized Water
MOS	Metal-Oxide-Semiconductor
MOSFET	Metal-Oxide-Semiconductor Field-Effect Transistor
PLD	Pulsed laser deposition
PVD	Physical Vapor Deposition
R&D	Research and Development
UB	Ultrasonic Bath
UHP	Ultra-High Pure
XPS	X-Ray Photoelectron Spectroscopy
XRD	X-Ray Diffraction

atm	Atmosphere/atmospheric
ac (AC)	Alternating current
AFM	Atomic force microscopy
EDS	Energy dispersive X-ray spectroscopy
FWHM	Full-width at half-maxima of a diffraction peak
I-V	Current vs. voltage
IR	Infrared
rf (RF)	Radio frequency
SEM	Scanning electron microscopy
SQUID	Superconducting Quantum Interference Device
UV	Ultraviolet
vs.	Versus
RT	room temperature
RE	rare-earth
HRTEM	high resolution transmission electron microscopy
RF	radio frequency
rms	root mean square

Contents

List of Figures

List of Tables

Chapter 1

Introduction

1.1 Aims and outline of this thesis

The application of new materials has always been the driving force behind the progress and prosperity of society and symbol of the civilizations (e.g., Stone Age, Bronze Age, Iron Age, *etc.*). The development, integration, and application of multifunctional materials would be an important aspect of the 21st century. Oxide materials are of great scientific and technological importance because of their complex and multifunctional properties. The understanding of the magnetoelectric (ME) coupling in nanostructured single-phase multiferroics and ferroelectric/ferromagnetic heterostructures are very important for the realization of novel magnetoelectric and spintronic devices. The main goals of the present study are to enhance, control, and understand the origin of magnetoelectric (ME) and magnetodielectric (MD) coupling [1, 2] in multiferroics materials. Almost all the single-phase multiferroics show weak ME and MD coupling. To enhance the ME coupling, the present work is focused on multiferroics rare-earth (RE) manganite composites.

In pursuit of the above aims, the main objectives of the present work are:

1. Synthesis of multiferroics- rare-earth manganite solid-solutions and composites, such as BFO_{1-x}-GMO_x and BFO_{1-x}-DMO_x, x=(0.0,0.025,0.05,0.075,0.1,0.15, and 0.2)

2. Study of structural, microstructural, dielectric, ferroelectric, electrical,

magnetic, and spectroscopic properties for better understanding of the structure-property relationship and conduction (leakage current) mechanism.

3. Study of magnetodielectric effects (magnetocapacitance, magnetoimpedance, and magnetophase) to improve the understanding of magnetoelectric coupling.

Chapter 1 describes the most important theoretical foundations related to the material used in this work and an introduction to perovskite, specially of $BiFeO_3$ doped with $REMnO_3$. We describe the synthesis of the samples and the properties of $BiFeO_3$-$REMnO_3$ composite. Chapter 2 describe the experimental techniques used to characterize our samples. Chapter 3 describes the structural and magnetodielectric properties of $BiFeO_3$-$GdMnO_3$ multiferroics. Chapter 4 and 5 focuses on the conduction mechanism most suitable for our experimental data and the dielectric, activation energies, mobility, and general density of state of BFO_{1-x}-GMO_x and BFO_{1-x}-DMO_x as well. Chapter 6 is about the conclusion and future work proposed by us in the present work.

1.2 General background

Ceramics are materials with many applications since the late palaeolithic period. [3]

The use of ceramics has evolved over the years, but it still carries great importance in today's industry. Some of the most predominant uses of ceramic materials nowadays are for the manufacture of electronic and magnetic components [4]. It can have, due to its ionic or covalent bonds, a high or fragile

hardness [5]. Multiferroics are a type of ceramic that combines two or more ferroics properties such as ferroelectricity, ferromagnetism, and ferro-elasticity [6]. These materials have been the subject of much research since the combination of these properties can provide new data storage components, multiple state memory elements, new types of piezoelectric, spintronics devices, and transducers [7,8]. The most important theoretical foundations related to our materials are described herein. More specifically, the properties of perovskite ferrite bismuth.

In the present work we use the combination of two very well-known perovskite, one with excellent ferroelectric properties, Bismuth ferrite $BiFeO_3$ with a high Curie temperature and antiferromagnetic Neel temperature and the other with ferromagnetic properties, rare-earth manganite $REMnO_3$ (RE = Gd_3 and Dy_3). We will find a single-phase multiferroics material that has better property than both parents separately, improving the coupling of these two properties, the so call magnetoelectric coupling. We want to bring the ferroics transition temperature towards room temperature. To achieve this, the solid solution method [9,10] was used, which is very effective in achieving our goal. The study of the phases in our material were accomplished using the X-Ray Diffraction (XRD) technique. Therefore, we were able to define the best concentration of doped BFO to obtain an optimal result of magnetoelectric coupling. The structural parameters of our samples were calculated through the Rietveld refinement, and it was determined that for low concentrations the structure was rhombohedral with spatial group R3c. The other studies performed as magnetoimpedance, type of conduction mechanism of the samples and the calculations of some parameters such as mobility, the density of charge carriers, vibrational frequency of the electrons in the traps as well as their effective mass was made according to the characteristics of our samples.

Thus-far, increased attention persists on the study of multiferroics materials due to their commercial importance in present science and technology [11]. Multiferroics are multifunctional materials that exhibit simultaneous (anti) ferroelectric, (anti) ferromagnetic, and ferroelastic behaviors [60] even at and above room temperature (RT) as is the case of the single perovskite phase $BiFeO_3$ whose Curie temperature (T_c) and Neel temperature (T_N) are $\sim$ 857°C and $\sim$ 370°C respectively [13]. However, the single-phase multiferroics are rare in nature and although (BFO) is the ideal prospect of multiferroics materials, the compound is found to exhibit weak ferromagnetic properties at RT. It is also difficult to synthesize an ideal perovskite phase of pure BFO due to the comparable thermodynamic stability of Fe^{3+} and Fe^{2+} states of iron in the compound. This also results in the relatively low electric polarization and high leakage current in prepared materials. To solve these problems and enhance electric resistivity and multiferroics behavior, other ABO_3 perovskite compounds, such as $PbTiO_3$, $BaTiO_3$, $SrTiO_3$ $PrFeO_3$, $DyMnO_3$, $YMnO_3$ among others, have been combined with $BiFeO_3$ to form solid solutions with spontaneous polarization and magnetization [14–18]. Solid solutions of magnetic (magnetostrictive) and ferroelectric (piezostrictive) materials are a likely alternate approach to achieve multiple types of couplings and highs magnetoelectric coefficients with fast switching abilities for a wide range of applications [19]. In such a solid solution material, the field conversion is a two-step process: magnetostriction induced mechanical deformation resulting in a spin-electric dipole coupling and induced electric fields. Many of these solid solution multiferroics materials have already proven the conversion of energies between magnetic and electric fields and their potential use for magneto-electric (ME) based memory elements, smart sensors, and transducers. A strong ME coupling has been observed in orthorhombic rare-earth (RE) man-

ganite $REMnO_3$ (RE= Dy, Sm, La, Gd, Y, etc) [20]. It has also been reported that substitution with RE at Bi-site stabilize the perovskite structure, reduce the leakage current, and suppress the spiral spin structure which in turn leads to the release of latent magnetization [17, 18].

$GdMnO_3$ a well-known manganite material, which has an orthorhombic-orthoferrite structure and a ferromagnetic phase transition at $T_N \sim$ -230°C , presents the necessary properties to enhance the ME coupling of $BiFeO_3$. Since the T_N of $GdMnO_3$ is very low, so it is also probable that the solid solution of $BiFeO_3$ with $GdMnO_3$ could bring down the magnetic ordering temperature of $BiFeO_3$ towards the room temperature. According to the Goodenough−Kanamori rule that suggests a strong ferromagnetic interaction is expected between the empty Mn^{3+} orbital and filled Fe^{3+} orbital. Eventually, a decrease in T_N toward RT could be achieved by substitution of Mn^{3+} ions at the Fe^{3+} site of $BiFeO_3$ [21]. Several reports have also demonstrated the enhancement in multiferroic properties of $BiFeO_3$ by the substitution of Gd^{3+} at Bi-site is expected to switch off the lone pair activity of Bi leading to shifting the ferroelectric transition towards RT [22]. We report herein the synthesis and a suitable approach to improve the magnetoelectric coupling of $BiFeO_3$ by fabrication of BFO_{1-x}-GMO_x solid solutions for $0.0 \leq x \leq 0.2$ by auto-combustion method. The materials have been systematically characterized and investigated with the purpose of study the possibility of the compositional driven structural phase transition and its correlation with the ME coupling. Detail of the structural, microstructural, thermal, dielectric, ferroelectric, magnetic, magneto-dielectric and magneto-impedance properties are shown.

Multiferroic materials offer great potential application because of the combination of two or more ferroics properties like ferroelectricity, ferromagnetism and

ferroelasticity [23–25]. Bulk $BiFeO_3$ is a single-phase multiferroic that has a very high ferroelectric (FE) transition (Curie temperature of 1103K) and weak antiferromagnetic (AFM) Neels-temperature (643K) [26–29], it shows great promise because it can function at high temperature range [30,31]. Example of this application are nonvolatile ferroelectric random-access memory, magnetic data storage, high-sensitivity ac magnetic field sensors and electrical tunable microwave devices like filters, oscillators and phase shifters [23, 32, 33]. We muss emphasize that $BiFeO_3$ is lead-free, and it will help to avoid toxicity in the ferroelectric products. However, $BiFeO_3$ has a high leakage current density and different conduction mechanisms in ion-substituted $BiFeO_3$ bulk and films have been reported. In the last years researchers have been trying to solve this problem by the substitution of suitable elements at Bi/Fe-site of $BiFeO_3$ or to fabricate composites [34, 35]. Enhanced dielectric and magnetic properties of Gd- or Dy-doped $BiFeO_3$ have been reported [36, 37]. Not only Gd and Dy have been used but rare-earth elements in general because it helps to eliminate the impurity phase in $BiFeO_3$ materials and composite and enhance the magnetic properties of it [38]. In our case we report the conduction mechanism behavior of $GdMnO_3$ and $DyMnO_3$ doped $BiFeO_3$ with x = (0,0.025,0.05,0.075,0.1,0.15 and 0.2) synthesized by solid-state reaction technique. Because of the high conductivity in bulk $BiFeO_3$ it can be used to create a magneto-electric Access Memory (MERAM) [39] and can be integrated into microelectronic devices. [40] Ohmic-, Space charge conductivity- and Hopping-mechanism are present in all of our samples. Other conduction mechanisms were not present, we believe it is because of the moderate field we used.

We also study different conduction mechanisms in the samples. The conduction mechanism found in the literature for $BiFeO_3$ and another similar perovskite

are interface limited (ILC) and bulk limited conduction (BLC). In Matsuo *et al* [41] the Space Charge Limited Conductivity (SCLC) for $BiFeO_3$ and Ohmic conduction for BFMO were reported. Considering the first one (ILC) we have fitted Schottky emission. The dielectric constant values we extracted from the slopes of these plots are three orders of magnitude less than expected (ϵ_r= 0.028) and in our case is approximately ϵ_r=40 for this sample in agreement with the literature [42, 43]. If the electronic mean free path in the insulator is less than the thickness of the dielectric film, we have to fit Schottky emission modified for thicker samples [44], but we get the same result of the dielectric constant because the slope is the same as normal Schottky. Other possible mechanisms are Fowler-Nordheim tunneling and we fitted this model to our data. Our temperature was not low enough for suppressing of the thermionic emission. The thermionic emission is dominant at this high temperature (500°C or more). [45] To identify electron effective mass and barrier height, is useful to measure the thermionic emission at high temperature and the tunneling current at low temperature, both at high electric field [46, 47]. In bulk limited conduction mechanisms we fit Ohmic conduction at low temperature and voltage. SCL-conduction at middle voltage, and Pool-Frenkel (PFC) and Hopping conduction (HC) at high voltage. At high temperature we extract the hopping distance 2 microns (long-range hopping), the frequency of the thermal vibration (f=82MHz) and the effective mass (m_{eff}) which is similar to the mass of the electron (m_e) for 300, 400, and 500K (m_{eff}= 1.036m_e), this is due to the size of our samples which are far beyond 4nm of thickness [48, 49], but it turned out that PFC does not fit our experimental data. In general, t is found in the literature that in band to band transport the mobility is larger than 1cm^2/Vs, independent of electric field and decreases with increasing temperature while in hopping transport the mobility

is smaller than 10^{-2}cm^2/Vs, depends on the electric field and increases with increasing temperature. In our case the mobility is low, in order of 10^{-3}cm^2/Vs and inversely proportional to the temperature [45]. Therefore we can conclude that the kind of mobility we have in our sample is a hopping Mobility and of course a hoping transport and not a band transport. For semiconductors in general if the conductivity $\sigma \geq 10^{-2}$ Ω^{-1}cm^{-1} is too conductive and for $\sigma \leq 10^{-8}\Omega^{-1}$cm^{-1} is too insulating. The conductivity results of our samples are in between these values. We performed our measurement in a temperature range from 100-500 K.

The perovskite are ceramic with the ABX_3 formula. X can be fluorine forming complex halide perovskite or it can be oxygen forming oxides. This last group is the group we are focusing in this work with the general formula ABO_3. In general, a perfect perovskite has a cubic structure with a special group Pm-3m, where the cation A is surrounded by twelve oxygen atoms (anion) forming a octahedron cube and it is electropositive and bigger than a cation B. Cation B is located in the center of the octahedron surrounded by six oxygen. The oxygen has a coordination number of 2 to the B cation and 4 to the A cation.(Figure 1.1).

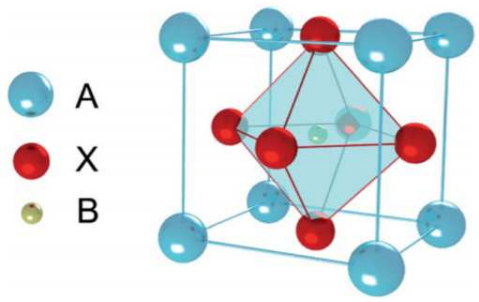

Figure 1.1: Perovskite structure ABX_3. [50]

Outside the ideal symmetry, the perovskite can have a tetragonal, orthorhombic and monoclinic structure as they are distorted. In general, the

value τ, called the tolerance factor of Goldschmidt, is used to recognize whether the perovskite structure is formed or not. This tolerance factor has the form represented in the formula 1.1 [51] and the perovskite structure will form if $0.8 \leq \tau \leq 1.0$.

$$\tau = \frac{r_A + r_O}{\sqrt{2}\,(r_B + r_O)} \tag{1.1}$$

Where r_A, r_B and r_O are the ionic radius of the cations A and B and the anion O^{2-} respectively. If the tolerance factor is greater than unity, the trigonal and orthorhombic structure prevail and if the tolerance factor is less than 0.75, the hexagonal structure predominates.

These perovskite-like structures have special properties due to the presence of defects in their crystalline network. These compounds in general are insulators but can change their properties due to a different kind of doping to semiconductors and even superconductors. These properties are determined by their stoichiometric relationship and by the different preparation methods used in their synthesis. In our current work, the interest we have in these structures is especially the combination of two well-known perovskites. Each has known ferroelectric- and ferromagnetic properties. We predict that our material formed by these two materials of different properties has multiferroic properties. In our case, we look for a strong magnetoelectric coupling in this new material.

1.3 Magnetism

Another extremely important materials are magnetic materials. In magnetic materials, we have that the sum of the spins of the electrons in the same energy level is not canceled. According to Pauli's exclusion principle, two electrons

can never occupy the same energy level. In the case of magnetic materials, the magnetic dipoles are oriented in groups called magnetic domains that differ in orientation to other domains within the material. These magnetic domains are separated by zones called Bloch zones. Depending on the intensity of the external magnetic field applied, these domains will be oriented more and more in the opposite direction to this field, thus creating the magnetic polarization. There are three fundamental forms that cause magnetic moments in atoms or ions. The first is due to the spin of electrons, the second magnetic moment is due to the orbital angular momentum of the electron around the nucleus and the third is due to the deformation caused by an external magnetic field at the angular magnetic moment.

First, we have the unpaired electron spin. If we have two or more electrons with spin in the same direction, or that they are not paired, the magnetic field that those electrons create adds up. In this case, we have a paramagnetic material. In the case that one has a material with two or more electrons, which are paired, that is one with its spin up and the other with its spin down, then the magnetic fields that these two paired electrons create cancel each other out. This is the case of a diamagnetic material. The total spin angular momentum is defined by formula 1.2

$$\vec{S} = \sum_i \vec{s}_i \tag{1.2}$$

Second, we have the spin-orbit coupling interaction to form the total angular momentum (Formula 1.3)

$$\vec{J} = \vec{L} + \vec{S} \tag{1.3}$$

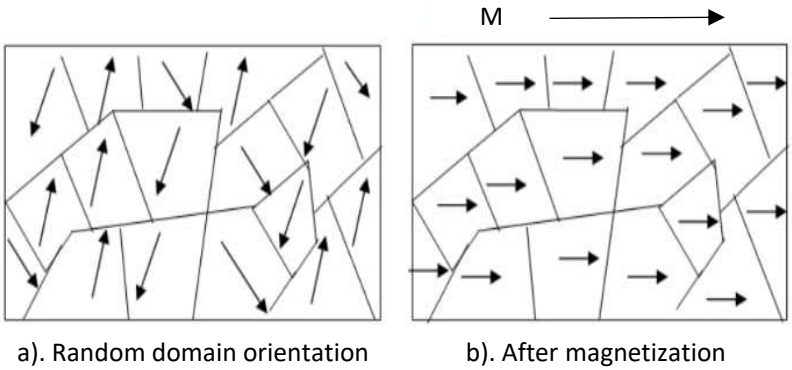

Figure 1.2: Magnetic Domain. A. Random domain orientation, B. After magnetization

This kind of coupling can be applied to most magnetic atoms and its call Russell-Saunders coupling. $\vec{J}$ take values from (L-S), (L-S+1), to (L-S-1), (L+S). The vector $\vec{L}$ and $\vec{S}$ exert a torque on each other which causes them to precess around the constant vector $\vec{J}$. The total momentum:

$$\vec{\mu_{tot}} = \vec{\mu_L} + \vec{\mu_S} \tag{1.4}$$

is not collinear with $\vec{J}$ [52].

Third, we have the Heisenberg exchange interaction. This interaction is because of quantum-mechanical exchange interaction between the atomic spin. The interaction depends on the distance between the two atoms and often it is sufficient to consider only the exchange interaction between spins on nearest-neighbor atoms. That can lead to parallel and antiparallel spin states. The antiparallel alignment of spin favoring a negative exchange or antiferromagnetic state and the parallel alignment of spins favoring a positive exchange or ferromagnetic state.

1.3.1 Diamagnetism

The magnetic moment of a free atom is caused mainly by three fundamental sources which are: The own spin of the electrons, the angular momentum of these around the nucleus, and the change in the orbital moment induced by applying an external magnetic field. The magnetic susceptibility per unit volume is defined as:

$$\chi = \frac{\mu_0 M}{B} \tag{1.5}$$

Here B is the intensity of the external or macroscopic field and M is the magnetic moment per unit volume. Magnetic susceptibility can have positive and negative values. Those substances with a positive value of magnetic susceptibility are defined as paramagnetic and those with a negative value, as diamagnetic. In atoms, the magnetic field induced by the movement of electrons due to the existence of an external magnetic field is diamagnetic and they induce a precession frequency ω equal to:

$$\omega = \frac{eB}{2m} \tag{1.6}$$

Lamor's theorem explains this phenomenon very well and from here the induced current I can be derived, which is:

$$I = (-Ze)(\frac{1}{2\pi} * \frac{eB}{2m}) \tag{1.7}$$

Remaining at the end, a magnetic moment that is the product of the current and the area of the loop. Taking into account that the area of the loop with radio ρ is $\pi\rho^2$, it gives a magnetic moment equal to:

$$\mu = -\frac{Ze^2B}{4m}\left\langle \rho^2 \right\rangle \tag{1.8}$$

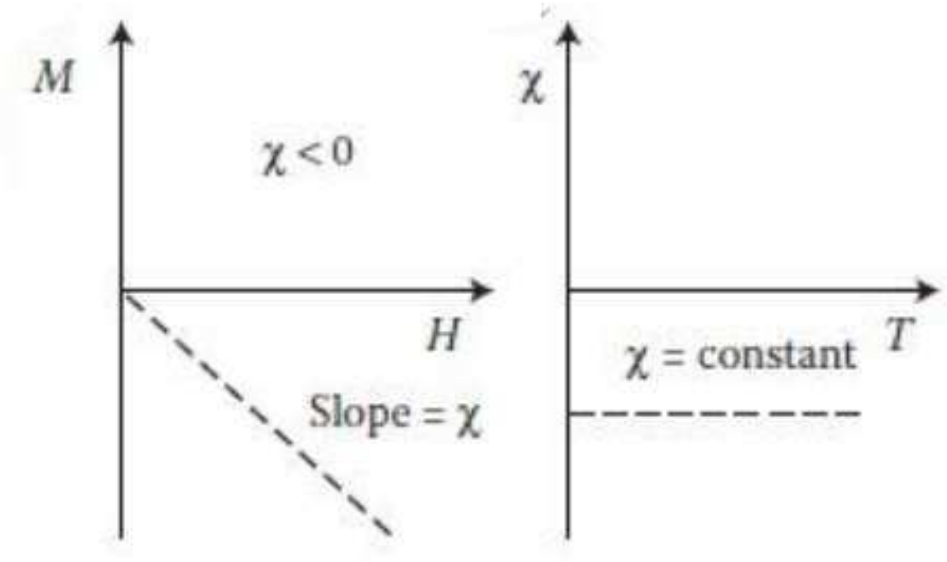

Figure 1.3: Diamagnetic material behavior depending of an external magnetic field and temperature [53].

We know that the diamagnetic susceptibility per unit volume for spherically symmetry distribution of charge $\langle r^2 \rangle = \frac{3}{2}\langle \rho^2 \rangle$:

$$\chi = \frac{\mu_0 N \mu}{B} = -\frac{\mu_0 N Z e^2}{6m} * \left\langle r^2 \right\rangle \tag{1.9}$$

Where N is a number of atoms per unit volume. This is the classical Langevin result. In dielectrics, the diamagnetic contribution of the core ions is accurately described by this Langevin result.

1.3.2 Paramagnetism

Paramagnetic materials are those materials that have an odd number of electrons in atoms, molecules, and lattice defects. This way the total spin of the system is different from zero. It can also be found in free atoms and ions with partially occupied internal orbital and in some compounds with even numbers of electrons such as molecular oxygen and especially paramagnetism can be found in metals.

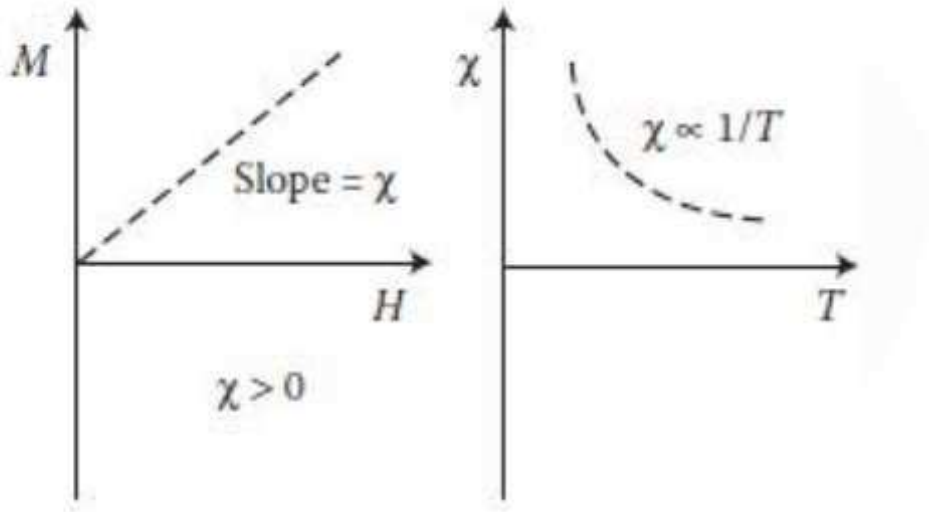

Figure 1.4: Paramagnetic material behavior depending of an external magnetic field and temperature [53].

1.3.3 Ferromagnetism

We also have ferromagnetic materials, which we can describe for a better understanding as an alignment of the magnetic dipoles that resemble the alignment explained above of the electric dipoles in the ferroelectric (see Figure 1.2). According to the theory of mean-field approximation, we have that each spin

sees the average magnetization of all other spins. The temperature for which spontaneous magnetization is completely lost from it is called Curie temperature T_c. For temperatures higher than T_c, we find a disordered paramagnetic phase, and for lower temperatures an ordered ferromagnetic phase in the material. Here we have the Curie-Weiss law of magnetic susceptibility which is equal to:

$$\chi = \frac{C}{T - T_c}$$

having this a singularity where the temperature T is equal to T_c.

In Figure 1.5 we can see a typical non-linear M-H hysteresis loop. In this curve, we can observe that for larger values of the magnetic field (H), the magnetization (M) also increases until it is saturated. This saturation point is called magnetic saturation F. When the value of the field (H) decreases, the path of the magnetization (M) is another and for H = 0, M is equal to B shown in the graph, this point is called remnant magnetization.

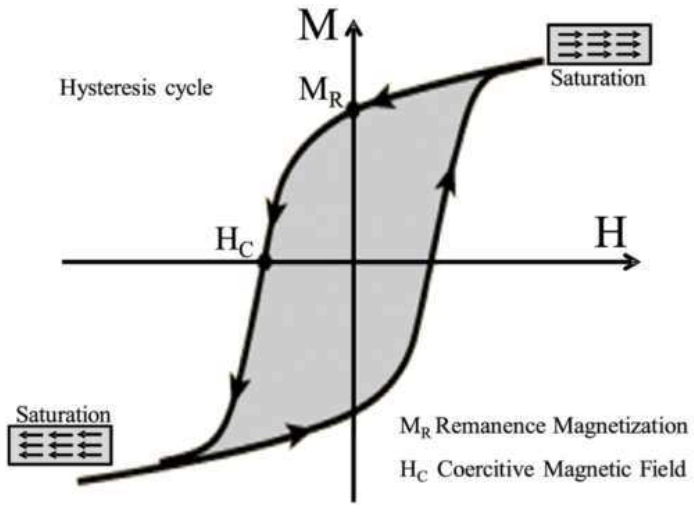

Figure 1.5: Ferromagnetic Hysteresis. M_R remanent magnetization, H_C Coercitive Magnetic Field [57].

The Figure 1.6 shows the order of spin when J > 0 (ferromagnets) and when J< 0 (antiferromagnets) [52].

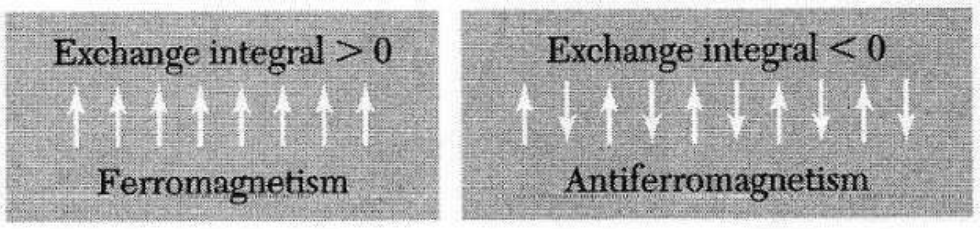

Figure 1.6: Spin for J>0 and J<0.

1.3.4 Antiferromagnetism

A simple antiferromagnet can be viewed as a material made up of two magnetic sublattices. The magnetic moments of the two sublattices are of equal magnitude but have opposite directions.

This causes the total magnetization of an antiferromagnetic to equal zero. An example of this is represented in Figure 1.7 which shows a YMn_2Ge_3molecule below its Neel temperature.

Figure 1.8 shows the dependence of the temperature that is observed in the magnetic susceptibility for the different cases.

1.3.5 Ferrimagnetism

This state appears when most of the magnetic moments (ex. Fe^{3+}) of the ions are antiparallel to each other. In this way, the net magnetic moment is due only to those of other ions (Fe^{2+}). This was observed especially in the magnetic oxides known as ferrites. The term ferrimagnetic is used to define the magnetism in compounds where some ions have magnetic moments antiparallel to other ions.

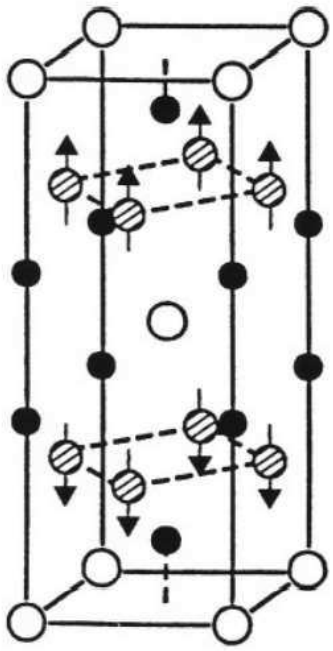

Figure 1.7: Magnetic moments in the unit cell of the antiferromagnet YMn_2Ge_2 [53].The dashed circles are the magnetic Mn atoms

1.4 Multiferroics and magnetoelectrics

These days it is very important to develop materials that have more than one function in the same compound. These materials can be single-phase or composed of two or several phases. Our objective is to develop a material with a single-phase and that is multiferroic as we have described before [58, 59]. The properties that we want to combine are ferromagnetism and ferroelectricity. There are materials with special properties such as ferroelectrics, which are materials that have a spontaneous polarization that can be modified with an external electric field. There are also ferromagnetic ones that have spontaneous magnetization and similar with the ferroelectric ones. These can modify their magnetization with an external magnetic field as well as the ferroelastic, which

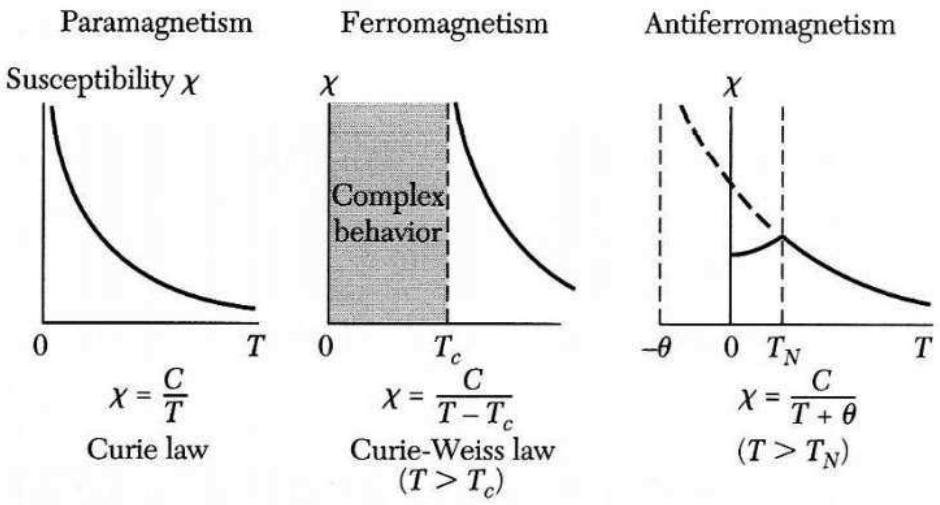

Figure 1.8: Temperature dependence of the magnetic susceptibility.

are nothing more than materials that when deformed can create differences in voltage and vice versa.

In other words, a ferromagnetic crystal is one that has a switchable and stable magnetization due to the mechanical-quantum phenomenon of exchange. Ferroelectric crystal has a switchable and stable electrical polarization that manifests itself in the atomic displacement within the unit cell. Thus, it must be said that very few multiferroic materials exhibit these two properties. At the same time, the magnetoelectric coupling in a material is a more general phenomenon to find that has its beginnings around the 50s and 60s of the last century [60].

Ferroelastic materials have spatial inversion symmetry like Ferromagnetic materials. On the other hand, Ferroelectric and multiferroic materials do not have spatial inversion symmetry. However, Ferroelastic and Ferroelectric materials have time-reversal symmetry that ferromagnetic and multiferroic materials do not.

There are several conditions that must be met for a material to be [61]

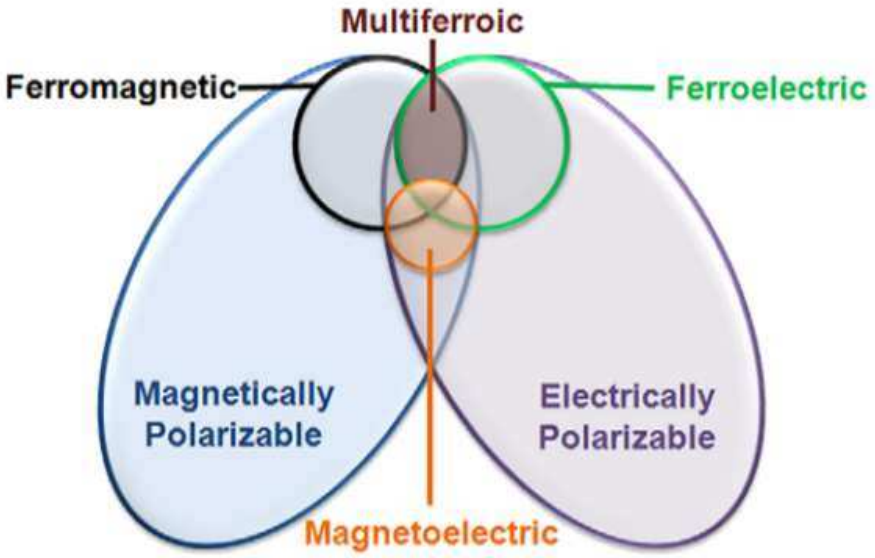

Figure 1.9: Multifferoic Magnetoelectric relationship. Ferromagnets (ferroelectrics) form a subset of magnetically (electrically) polarizable materials such as paramagnets and antiferromagnets (paraelectrics and antiferroelectrics). Magnetoelectric coupling is an independent phenomenon that can, but need not, arise in any of the materials that are both magnetically and electrically polarizable. In practice, it is likely to arise in all such materials, either directly or via strain. Adapted from [60].

magnetoelectric. The material must have a high resistivity to avoid leakage current. Some symmetries are necessary for these materials. It is necessary to change the electrical polarization with a magnetic field and change the direction of magnetization with an electric field. In our case, we are combining a well-known ferroelectric ($BiFeO_3$) with a good ferromagnetic ($GdMnO_3$ or $DyMnO_3$).

We must solve the compatibility between ferroelectricity (insulating materials with full d orbital) and ferromagnetism (need for conduction electrons and incompletely filled d shells). That is the main problem finding these materials and why are they so scarce. The most important thing to achieve synthesizing a magnetoelectric material is to accomplish a strong magnetoelectric coupling to manufacture devices that are more energy-efficient and have a greater resistance to temperature changes.

1.5 Dielectric materials

There is currently a great interest in the field of electronics to reduce the size of the devices considerably. Therefore the dielectric and magnetic properties of ceramic materials are so important [54]. There are different types or methods of polarization of matter, more specifically, the polarization of a dielectric. The dielectric polarization is the displacement of electrical charges in the material due to the external electric field, see Figure 1.10. The electronic cloud around the core runs in the opposite direction to the applied external field. This makes one part of the atom slightly positive and the other slightly negative. Ferroelectricity is the property of some dielectrics of having a spontaneous electrical polarization, as the separation of positive and negative charges, causing the crystal to have a positively charged moiety and a negatively charged moiety. This spontaneous polarization can be reversed in the direction with the application of an external electric field.

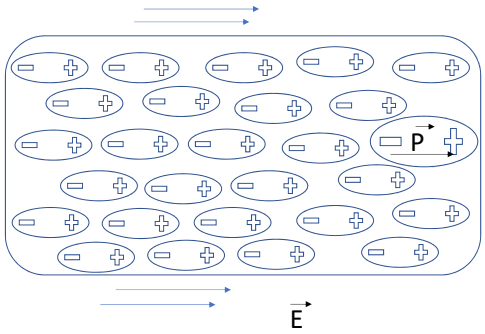

Figure 1.10: Dielectric polarization.

In Figure 1.10 $\vec{P}$ is the polarization vector with a negative charge to positive charge direction in dielectric and $\vec{E}$ is the external electric field. The macroscopic effect observed in the polarization phenomenon is like a displacement of the

positive charges in relation to the negative charges. In these cases, it is better to work with the $\vec{P}$ total polarization that is not more than the sum of the electrical dipole moments in a small volume in the dielectric. This process is described in the formula (1.10).

$$\vec{P} = \sum \frac{\Delta \vec{p}}{\Delta v} \tag{1.10}$$

where Δv is a volume element.

There are other types of polarization in a dielectric and each polarization has a range of frequencies where it manifests itself and there may be more than one type of polarization in the same material. In Figure 1.11 can we see another type of polarization. As stated earlier, another polarization is the displacement of negative and positive ions away from each other. We also find polar materials that in the presence of an external electric field reoriented themselves to minimize the potential energy in the system, thus giving rise to a polarization of orientation. We can also find space charge polarization in the materials interface. This polarization has as a result an increment in the capacitance of the dielectric. The total polarization of the system is the sum of all polarization process present in the dielectric. See equation 1.11.

$$P_T = P_e + P_i + P_o + P_s \tag{1.11}$$

Where P_e is the electronic polarization, P_i the ionic-, P_o the orientation- and P_s the space charge polarization.

We can also find spontaneous polarization. Electronic polarization is present in all kinds of materials and ionic polarization only in materials made of two or more different kinds of atoms. In both polarization phenomena, the dipole

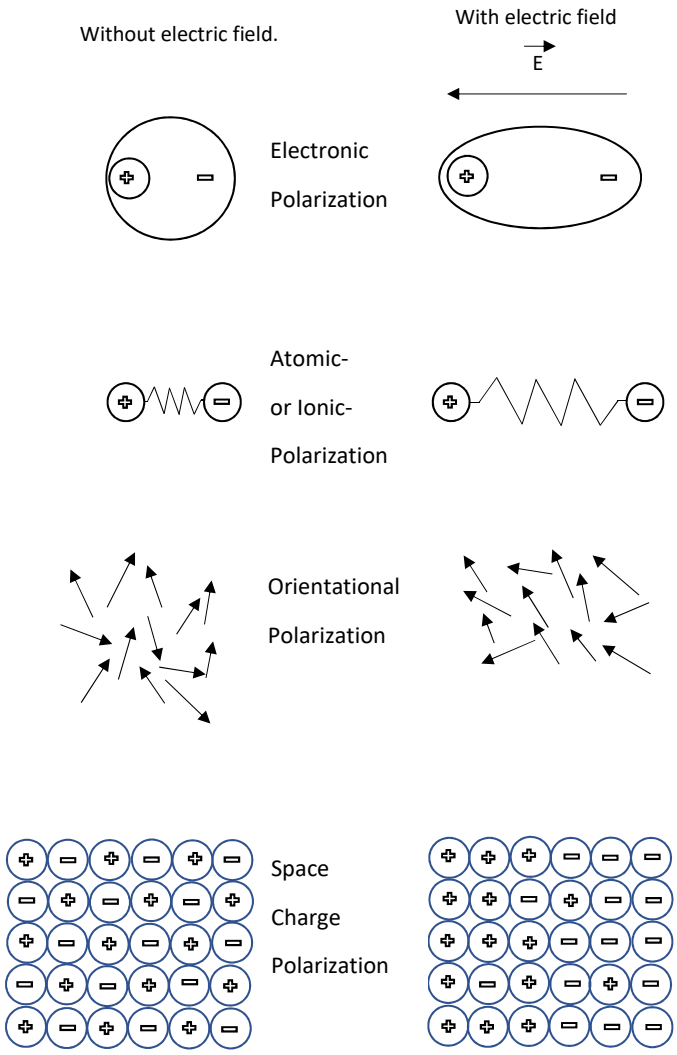

Figure 1.11: Different type of polarization. Left without and right with electric field.

moment is induced by an electric field. For this type of polarization, the dependence on temperature is almost neglected. Orientational polarization only occurs in materials with permanent dipole moment in absence of an external electric field. However, these dipoles are randomly oriented so the material will show an orientational polarization only in the presence of an external electric field. After removing of the external electric field, the net polarization, because of the ther-

mal excitation, will return to zero. Therefore, the polarization decreases with rising in temperature. In other cases, we can find a spontaneous polarization in the absence of an external electric field. Similar to ferromagnetic polarization we can find a ferroelectric polarization with a very high polarizability. This kind of polarization only occurs in materials with noncentrosymmetric structure [55] So the term ferroelectric come from the analogy to ferromagnetic.

We can find electric polarization associated with mobile and trapped charges, this kind of polarization is the space charge polarization (P_s) and can be separated in hopping polarization and interfacial polarization. Injected charge carriers from the electrical contact may be trapped at the interfaces or at the bulk impeding more injected carriers to go in the material. Because of the charge accumulation, the dielectric constant will be affected. The hopping dipole moment is a different type of dipole to the orientational dipole moment because it is not a permanent dipole moment formed by bound charges. Instead, the hopping dipole is formed by the hopping of a charged particle from one potential well into another. (see Figure 1.12)

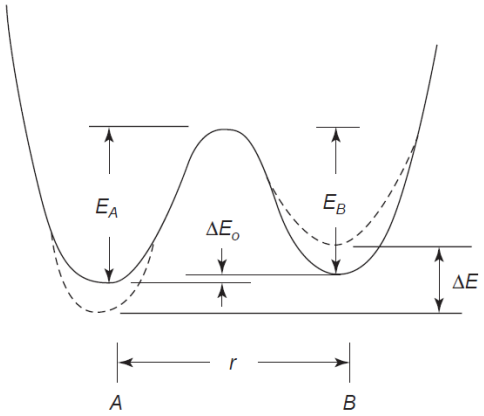

Figure 1.12: Hopping of a charge particle from one potential wall into another [55]

.

The space charge, or interfacial polarization, is produced by the separation of mobile positively and negatively charged particles under an applied field, which form positive and negative space charges in the bulk of the material or at the interfaces between different materials [55].

1.5.1 Ferroelectric material

Ferroelectric materials possess a reversible spontaneous polarization in a specific temperature range. At a specific temperature, called Curie Temperature (T_C), occurs a phase transition. The polarization can be associated with a hysteresis (see Fifure 1.13). The shape in the hysteresis depends on the change in polarization orientation.

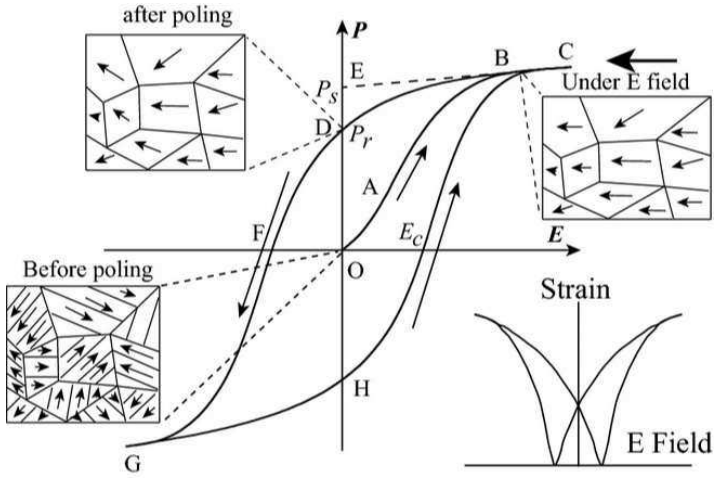

Figure 1.13: Ferroelectric Hysteresis and corresponding domain reversal and strain-electric field curve [56]

Here P_s is the spontaneous polarization and the strain-electric field has like butterfly form. For the ideal ferroelectric system, the hysteresis loops should be symmetric, so the positive and negative E_c and P_r are equal. The most important in the hysteresis loop is to understand the relationship between microscopic

structures and macroscopic properties [56].

There are parameters that define what is the quality of a ferroelectric. Among these parameters are the dielectric constant (ϵ), the energy loss factor ($\tan \delta$), the spontaneous or saturation polarization, the remaining polarization, and the energy necessary for the polarization to occur as well as the orientation change of the dipoles. This energy is described by the area within the curve of the hysteresis cycle. The dielectric constant ϵ is the relation between the electrical energy stored in a material (E) depending on a voltage applied with respect to that stored in the vacuum (E_0). This dielectric constant is derived from the different contributions of polarization existing in the material and the equation that describes it is the equation (1.12). The energy stored in the material is always greater than that of the vacuum. Therefore, the dielectric constant will always be greater than one and specific to each material. In this way, we can relate a large dielectric constant with a greater amount of electrical energy stored in the material.

$$\epsilon = \frac{E_0}{E} \tag{1.12}$$

The energy losses in the dielectric described by $\tan \delta$ can appear from one or several of three fundamental processes. The first process would be due to ionic migration in the material due to ion jump or dipole relaxation. The second of these processes would be due to the vibrations in the crystal and its deformations. the third energetic loss would be due to the electronic polarization because of the adsorption and the heat energy in the visible spectrum [54]. The loss of energy that affects mostly the use of ferroelectric in electronics is the migration of ions at low frequencies and with the increase in temperature. The energy loss factor ($\tan \delta$) can be written in terms of electrical conductivity, see equation (1.13)

$$tan\delta = \frac{\sigma}{2\pi f k' \varepsilon_0} \tag{1.13}$$

Where σ is the conductivity, f is the frequency of the external electric field, k' the dielectric constant of the material and ε_0 the permittivity in vacuum.

1.6 Bismuth ferrite (BFO)

$BiFeO_3$ is a single-phase material that represents multiferroics very well. It is considered to be the first modern useful multiferroic material [62]. In the literature, it has been reported that $BiFeO_3$ has 8 forms of structural transitions. Fe^{3+} Is a very good material for the magnetic cation, its has five 3d electrons. Each of these electrons occupies its own d orbital and are aligned parallel to the others. This way these electrons proportion the largest possible spin moment of 5 μ_B. Bi^{3+} has a active lone pair of electrons, this way its 6s 2 valence electrons localize and generate a polar structural distortion around the A site [63].

The structure of the BFO is shown in Figure (1.14). Here the cations are displaced along the [111] direction relative to the anion. The oxygen octahedral rotates with alternating sense around the [111] axis.

$BiFeO_3$ has ferroelectric properties at temperatures lower than the curie temperature (Tc = 820 - 850°C) with a perovskite structure and spatial group R_{3C} at room temperature [65]. $BiFeO_3$ also has a G-type antiferromagnetic order, in which the Fe magnetic moment are ferromagnetically within [111] aligned and antiferromagnetically between adjacent [111] shown in Figure (1.15) at temperatures below its Neels temperature (Tn = 350 - 380°C) [66, 67]. Therefore we have a perfect antiferromagnet. Antiferromagnetism in this particular case happened because of the double exchange mechanism so called the superexchange

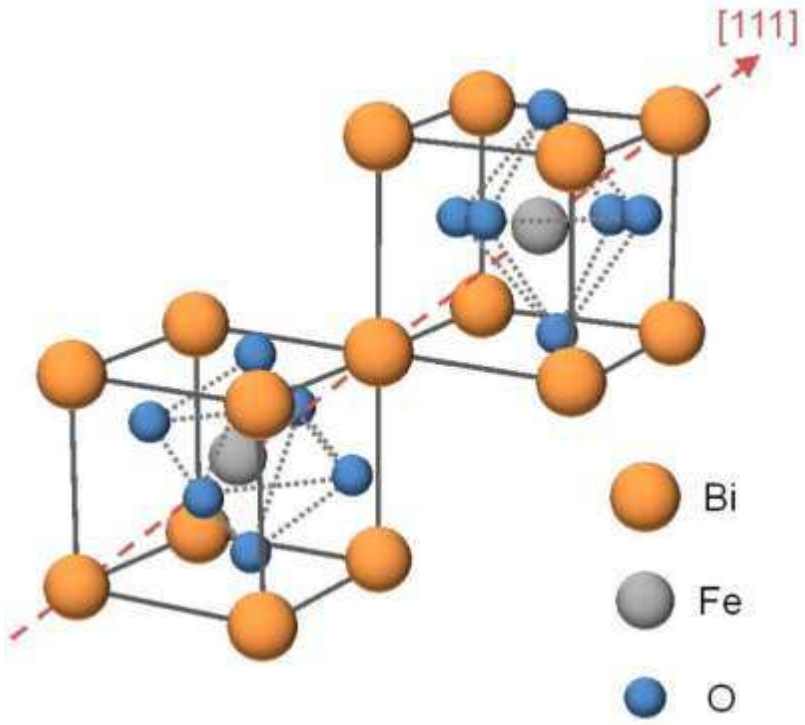

Figure 1.14: Schematic of the R_{3C} structure from two cubic perovskite $BiFeO_3$ unit cell [64].

mechanism, here you have a virtual hopping of electrons. $BiFeO_3$ also has a spin cycloid structure in the bulk [68] showing a preferred orientation od the aligned AFM spins in the [111] direction. This way Antiferromagnetism is coupled to the ferroelectric polarization [69].

One of the main problems of $BiFeO_3$ is the formation of parasitic phases ($Bi_2Fe_4O_9$, $Bi_{25}FeO_{40}$ and $Bi_{36}Fe_{24}O_{57}$) [70, 71]. Mixing $BiFeO_3$ with rare-earth help stabilize the phase of the materials as well as improve the magnetoelectric coupling of the material. The sol-gel method is the method we used for this study, with which we were able to obtain a single-phase material for low doping and a compound for higher doping of our samples [72, 73]. Our goal is to achieve a single-phase material by making a substitution in both part A and part B of the $BiFeO_3$ with $ReMnO_3$ where Re= Dy, and Gd. In this way we have managed

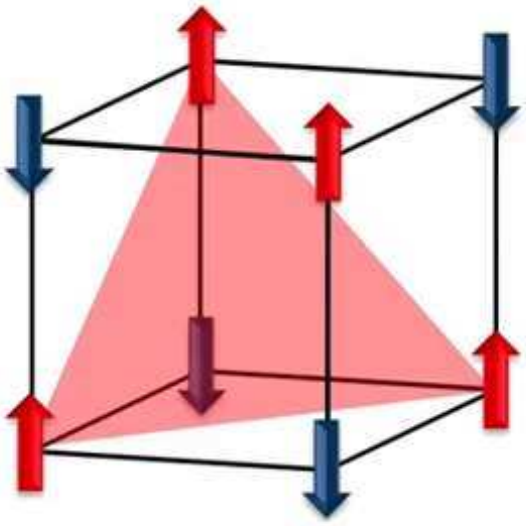

Figure 1.15: Schematic of the G-type AFM order in cubic perovskite $BiFeO_3$ unit cell in Figure (1.14).

.

to improve the magnetic and electrical properties of the $BiFeO_3$ as well as the magnetoelectric coupling in a single-phase material BFO_{1-x}-GMO_x.

1.7 Solid solution of BFO-REMO

One of the most important parts in the process of creating a multiferroic material is its synthesis [60]. For this synthesis, high purity material was used to achieve the shape of the polycrystalline ceramic. Oxide precursors with high purity (99.9%) were mixed with the necessary stoichiometry in methanol by hand and then with the high-energy ball milling for 10h. After mixing the product was dried at low temperature and then calcined at 875°C to obtain the desired phase. The product was put back in the high-energy ball milling for 6h. Then it was filtered by a 45 micron filter to do the XRD analysis. After verifying the result

of the XRD as a positive one, the pellet was press with 8g of the material at 6 psi using polyvinyl alcohol as a binder. In the end, the Sintering process of the pellet was carried out at a temperature of 875°C for 6h following a rate when the temperature rose by 5°C per min. The final pellet was painted with silver paint to have the electrodes to perform the electrical and capacitance measurements. These samples were heated at 200°C for 1 hour to remove all moisture in them.

1.8 Materials in the present work

To develop materials for new devices, we are using ferroelectric and ferromagnetic materials with perovskite structures to achieve an improvement of the magnetoelectric coupling and study the types of conduction mechanism existing in this new multiferroic material. Here we have studied the solid solution of the synthesis of $BiFeO_3$ with RMnO3 in different concentrations to be able to choose which is the best relation of the material and thus be able to obtain improvements in the magnetoelectric properties near the phase change. Usually for this material the change of the phase occurs for x = 0.1% to 0.15% [74–76]. The synthesized materials for the research of this thesis are, BFO_{1-x}-GMO_x and BFO_{1-x}-DMO_x with a concentration of $0.0 \leq x \leq 0.2$.

References

[1] A. Pimenov, A.A. Mukhin, V. Yu. Ivanov, V.D. Travkin, A.M. Balbashov, and A. Loidl, Possible evidence for electromagnons in multiferroic manganites, Nature Phys., 2, 97-100 (2006)

[2] G. Lawes, A. P. Ramirez, C. M. Varma and M. A. Subramanian, Magnetodielectric effect from spin fluctuations in isostructural ferromagnetic and antiferromagnetic systems, Phys. Rev. Lett. 91, 257208-1-4 (2003)

[3] Ceramic and Glass material role in civilazation,(https://ceramic.org/about/what-are-engineered-ceramics-and-glass/brief-history-of-ceramic-and-glass (Accessed 05/15/2021))

[4] V.A Khomchenko, J.A. Paixao, V.V. Shvartman, P. Borisov, Sci. Mater. 62, 238-241, (2010)

[5] J. Ryu, S. Priya, K. Uchino, J. Electroceram. 8, 107-119, (2002)

[6] H. Koizumi, N. Nirizaki, T. Ikeda, J. Appl. Phys. 3, 495-496, (1964)

[7] S. Karimi, I.M. Reaney, I. Levin, I. Sterianou, Appl. Phys. Lrtt. 94, 112903, (2009)

[8] Y.E. Roginska, Y.Y. Tomashpo, Y.N. Venevtse, V.M. Petrov, G.S. Zhdamov, Sov. Phys. JETP USSR 23, 47, (1966)

[9] A.V. Zalesskii, A.A Frolov, T.A. Khimich, A.A. Bush, Phys. Solid-State 45, 141-145, (2003)

[10] F.Gonzalez-Garcia, C.S. Riccardi, A.Z. Simoe, Mater. Chem. Phy. 116, 305-309, (2009)

[11] M. Fiebig, T. Lottermoser, D. Meier and M. Trassin, Nature Reviews Materials, Vol 1, 16046 (2016)

[12] W. Eerenstein, N. D. Mathur and J. F. Scott, Nature, Vol 442, 17 (2006)

[13] D. Pang, C. He, X. Li, S. Han,S. Pan, X. Long,Ceramics International 42, 9347-9353 (2015)

[14] M.M. Kumar, A. Shrinivas, S.V. and Suryanarayana. J Appl Phys 87, 85562 (2000)

[15] T.L. Ivanova and V.V. Gagulin. Ferroelectrics 10, 265:2416 11 (2002)

[16] V.S. Sunder, A. Halliyal, A.M. Umarji. J Mater Res 10, 13016 (1995)

[17] S. N. Tripathy, K. K. Mishra, S. Sen, B. G. Mishra, Dhiren K. Pradhan, R. Palai and D K. Pradhan, J Appl Phys 114, 144104 (2013)

[18] S. N. Tripathy, Dhiren K. Pradhan, Karuna K. Mishra, Shrabanee Sen, Ratnakar Palai, Marian Paulch, J. F. Scott, RS. Katiyar and D K. Pradhan. J Appl Phys 117, 144103 (2015)

[19] P. Haribabu, A. Venkateswarlu, P. Shashank and R. Jungho. Actuators 5, 9 (2016)

[20] F. Schrettle, P. Lunkenheimer, J. Hemberger, V. Yu. Ivanov, A. A. Mukhin, A. M. Balbashov, and A. Loidl, Phys. Rev. Lett. 102, 207208 (2009)

[21] C.H. Yang, T.Y. Koo and Y.H. Jeong, Solid-State Communications 134, 299 (2005)

[22] S. M. Selbach, T. Tybell, M. Einarsrud, and T. Grande, Chem. Mater.19, 6478 (2007)

[23] S. Pattanayak, R. Choudhary and R. Das, Journal Of Advanced Dielectric,4,2, (2014)

[24] T. Zhao, A. Scholl, F. Zavaliche, K. Lee, M. Barry, A. Doran, M. Cruz, Y. Chu, C.Ederer, N. Spalding, R. Das, D. Kim, S. Baek, C. Eom and R. Ramesh,Nat. Mater. 5, 823 (2006)

[25] R. Ramesh and N. Spaldin, Nat. Mater. 6, 21 (2007)

[26] S. Karimi, I. M. Reaney and Y. Han, J. Mater. Sci.44, 5102 (2009)

[27] S. Satpathy, N. Mohanty, A. Behera, K. Patra, B Behera and P. Nayak, Front. Mater. Sci., 7 295, (2013)

[28] S. Kiselev, R. Ozerov, and G. Zhdanov, Soviet Physics Doklady. 7 742, (1963)

[29] N. Spaldin, S. Cheong and R. Ramesh, Physics Today 63 38, (2010)

[30] Z. Zhong and H. Ishiwara, Appl. Phys. Lett. 95, 112902 (2009)

[31] G. Smolenskii and I. Chupis, Sov. Phys. Usp. 25, 475 (1982)

[32] J. Rehspringer, J. Bursik, D. Niznansky and A. Klarikova, J. Magn. Magn. Mater. 211, 291 (2000)

[33] A. Mousse, J. Herbert,(Chapman and Hall, London), p.390 (1990)

[34] J. Xu, G. Wang and Y. He, Mater. Lett. 63, 855 (2009)

[35] M. Vopsaroiu, M. Cain, G. Sreenivasulu, G. Srinivasan and A. Balbashov,Mater. Lett. 66, 282 (2012)

[36] A. Julian, S. Dalber and B. Elisa, J. Phys.: Conf. Series 200, 012134 (2010)

[37] A. Lahmar, S. Habouti, M. Dietze, C. Solterbeck and M. Es-Souni, Appl. Phys. Lett. 94,012903 (2009)

[38] F. Kubel and H. Schmid Acta. Crystallogr. B 46 698 (1990)

[39] M. Bibes and A. Barthlmy, Nature Mater 7425 (2008)

[40] G. Catalan and J F Scott, Adv. Mater. 21 2463 (2009)

[41] H. Matsuo, Y. Kitanaka, Y. Noguchi, M. Miyayama, J. of Asian Ceramic Sosieties, (2015)

[42] R. Masso, S.N. Tripathy, F. A. Aponte, D. K. Pradhan, R. Martinez, and R. Palai

[43] S. Godara, N. Sinhaa, G. Ray, B. Kumar, Journal of Asian Ceramic Societies 2, 416421, (2014)

[44] J. Simmons, Physical Review Letters, vol. 15, no. 25, pp. 967968, (1965)

[45] Fu. Chiu, Advances in Materials Science and Engineering, ID 578168, (2014)

[46] F. Chiu, Journal of Applied Physics, vol. 100, no. 11,Article ID 114102, 5 pages, (2006)

[47] D. Schroder, John Wiley and Sons, New York, NY, USA, 2nd edition, (1998)

[48] M. Stadele, F. Sacconi, A. Di Carlo, and P. Lugli, Journal of Applied Physics, vol. 93, no. 5, pp. 26812690, (2003)

[49] B. Brar,G. Wilk, and A. Seabaugh, Applied Physics Letters, vol. 67, no. 7, pp. 10311033, (1995)

[50] Yichuan Chen, Linrui Zhang, Yongzhe Zhang, Hongli Gaoa and Hui Yan, RSC Adv. 8, 10489, (2018)

[51] V. M. Goldschmidt, Geochemische Verteilungsgesetze der Elemente VII-VIII Skrifter Norske Videnskaps Akademi, Oslo, (1926)

[52] C.Kittel, Introduction to Solid-State Physics, 8 Edition, (2005)

[53] E. Motovilova, S. Huang, "Magnetic Materials for Magnetic Resonance and Magnetic Resonance Imaging", Ad. in Mag. Mat., (2017)

[54] W.D.Kingery, Wiley and Sons (1960)

[55] K. Chi Kao,Dielectric phenomena in solid, Elsevier, ($\mathbf{2-3-5}$), 75, (2004)

[56] L. Jin, F. Li and S. Zhang, J. Am Soc, 97, 1-27, (2013)

[57] R. Caraballo-Vivas, Magnetism from intermetallics and perovskite oxides, Thesis, (2017)

[58] H. Schmid, 162 317-338, (1994)

[59] S. Picozzi, C. Ederer, J. Phys. Condens Matter 21, 303201, (2009)

[60] W. Eerenstein, N. D. Mathur and J. F. Scott, Nature, Vol 442, 17 (2006)

[61] M.E. Fentes-Montero, E.A. Macias-Rios, C.O. Contreras-Vega, Tecnociencia Chihuahua, 27-35, (2007)

[62] J. Wang , J.B. Neaton , H. Zheng , V. Nagarajan , S.B. Ogale , B. Liu , D. Viehland , V. Vaithyanathan , D.G. Schlom , U.V. Waghmare , N.A. Spaldin , K.M. Rabe , M. Wuttig , R. Ramesh , Science 299 , 1719 (2003)

[63] N.A. Spalding, Frontiers of Materials Research, MRS Fall Meetting in Boston, (2016)

[64] C. Michel, et al., Solid-State Commun. 7, 701, (1969)

[65] L. Chia-Ching, W.U. Jenn-Ming, Appl. Surf. Sci. 253, 7069-7073, (2007)

[66] F. Kubel, H.M. Schmid, Acta Cryst. B46, 698, (1990)

[67] C. Blaauw, F.V.D. Woude, Solid-State Phys. 6, 1422-1431, (1973)

[68] I. Sosnowska, et al., J. Phys. C 15, 4835, (1982)

[69] C. Ederer, and N. A. Spaldin, Phys. Rev. B 71, 060401(R), (2005)

[70] P. Fischer, M. Polomska, I. Sosnowska, J. Phys. C: Solid-State Phys. 13, 1931-1940, (1980)

[71] A. Maitre, M. Francois, J.C. Gachon, J. Phase Equilib. Diffus. 25, 59-67, (2004)

[72] G.D. Achenbach, W.J. James, R. Gerson, J. Am. Ceram. Soc. 50, 437-1437, (1967)

[73] J.K. Kim, S.S. Jim, Won-Jeong K., mat. lett. 59, 4006-4009, (2005)

[74] R. V. Shpanchenko, V. V. Chernaya, A. A. Tsirlin, P. S. Chizhov, D. E. Sklovsky, and E. V. Antipov, Chem. Mater., 16, 3267 (2004)

[75] D. C. Arnold, K. S. Knight, F. D. Morrison, and P. Lightfoot, Phys. Rev. Lett. 102, 027602 (2009)

[76] J. Lee, M. Oak, H. Choi, J. Sonc and H. M. Jang, J. Mater. Chem., 22, 1667 (2012)

Chapter 2

Experimental Techniques

Studies of the physical properties (*e.g.* structural, microstructural, electrical, thermal, magnetic, magnetoelectric) of materials under various experimental conditions are useful in predicting their possible applications. In order to get a better understanding of structure-property relationships, various experimental techniques have can be used. In the present work I used X-ray diffraction (XRD) for structural studies, Energy Dispersive Spectroscopy (EDS) for composition, scanning electron microscopy (SEM)for morphology studies, X-ray photoelectron spectroscopy (XPS) for qualitative and quantitative analysis of composition and fundamental excitations, electrical and dielectric measurements for the understanding of conduction mechanisms of BFO_{1-x}-GMO_x and BFO_{1-x}-DMO_x . The underlying principles and experimental setup of each technique are briefly discussed in the following sections.

2.1 Synthesis of nanomaterials

Currently, there are many ways to synthesize a nanomaterial. Among these forms, we find the Sol-gel synthesis method, the combustion method, the hydrothermal method, the co-expression method and the method we use in this work, the solid-state method. This method is the most used in the synthesis of polycrystalline solids from the mixture of oxides. For this chemical reaction of solid precursors to be carried out it is necessary to introduce heat. This method is explained in section 1.7 with details.

2.2 Characterization techniques

2.2.1 X Ray diffraction

X-Ray Diffraction (XRD) is an important analytical technique primarily used for phase identification of crystalline material. This technique provides information about crystal structure, lattice parameter, the orientation of the thin films and strain and particle size of the crystalline structures. There are two processes that occur when the X-ray beam hits an atom, the first is that the beam is absorbed and ejects an electron from the atom, of the beam can be scattered. The primary beam utilized is generated by a cathode ray tube with a heated filament which produces electrons, then these are accelerated toward a target by an applied potential difference, and bombarding the target material with electrons. This beam is an electromagnetic wave with an electric vector that varies sinusoidally with time and perpendicular to the propagation of the beam itself. The electric field applies a force on the electrons of the atom which produces an acceleration of the electrons, this makes radiation. This radiation spreads in all directions from the atom, it has the same frequency as the primary beam and it is referred to as the scattering radiation.

From theoretical and experimental research it is known that there are two kinds of scattering; unmodified scattering (which has the same wavelength) and modified scattering known as Compton (with a longer wavelength). Using a crystal as an example gives an unmodified scattering. The unmodified scattering from an atom can be calculated with considering that each electron is a spread-out diffused cloud of negative charge with a density ρ. The ratio of charge in a volume dV to the charge of one electron is ρ dV. Now for each electron is:

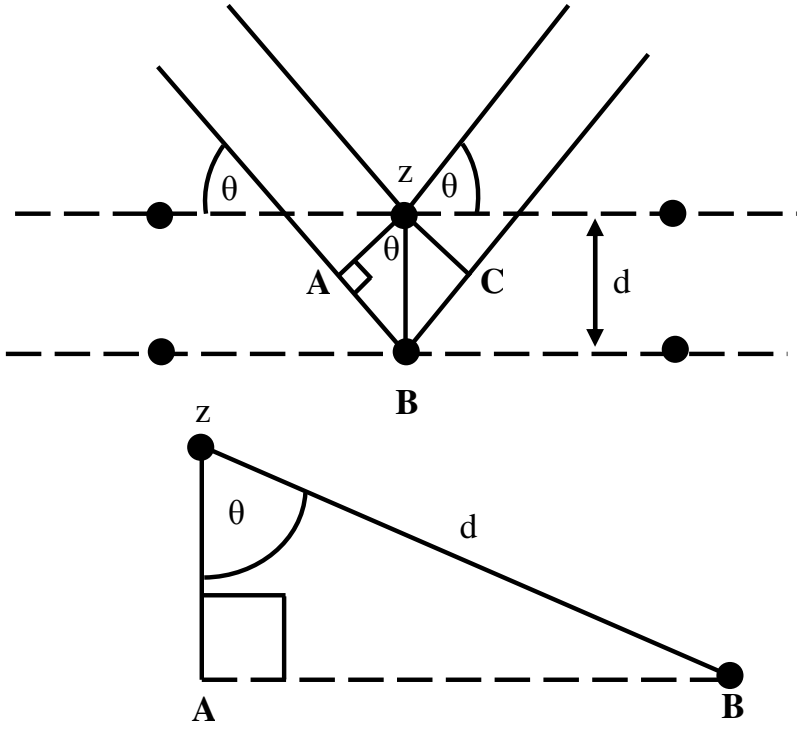

Figure 2.1: Schematic of X-ray diffraction by a solid.

$$\int \rho dV = 1. \tag{2.1}$$

To obtain the total amplitude of the unmodified scattering for one electron, we must integrate over the whole volume that the electron occupies, doing this we make proper allowance for the phase of the contribution from each element of ρ dV. Followed, we have the quantity represented by the integral f_e as the scattering factor.

$$f_e = \int e^{(2\pi \mathrm{i}/\lambda)(\mathrm{s}-\mathrm{s}_0)^{\mathrm{r}}} \rho dV. \tag{2.2}$$

As can be seen, f_e is the ratio of the amplitude from one electron with unmodified scattering to the amplitude scattered by an electron according to classical theory. In other words, f_e is the amplitude of unmodified scattering per electron and it is expressed in units of the electron. Even though we know that the charge distribution for each electron in the atom is spherical, but for closed groups of inner electrons, spherical symmetry exists, and with this, we can work with the combined charge distribution for the electron of a closed group.

The most important principle in X-ray diffraction is Bragg's law. Bragg's diffraction occurs when electromagnetic radiation or subatomic particle waves with wavelength comparable to the atomic spacings, are incident upon a crystalline sample, scattered by the atoms in the system, and undergo constructive interference in accordance to Bragg's law.

To consider the necessary conditions for Bragg's law, we must assume that the phases of the beams coincide when the incident angle equals and reflecting angle (see Figure 2.1) The rays of the incident beam are always in phase and parallel up to the point at which the top beam strikes the top layer at atom z. The second beam continues to the next layer where it is scattered by atom B. The second beam must travel the extra distance AB + BC if the two beams are to continue traveling adjacent and parallel. This extra distance must be an integral (n) multiple of the wavelength (λ) for the phases of the two beams to be the same:

$$n\lambda = AB + BC. \tag{2.3}$$

As we recognize that d is the hypotenuse of the right triangle AB_z, we can

use trigonometry to relate d and θ to the distance (AB + BC). The distance AB is opposite θ so we have:

$$AB = d \sin \theta. \tag{2.4}$$

And because AB=BC then we have that equation 2.4 becomes:

$$n\lambda = 2AB. \tag{2.5}$$

Then, substituting the equation 2.4 in equation 2.5 we have:

$$n\lambda = 2d \ \sin \theta \tag{2.6}$$

This is known as Bragg's law and can be used to understand the diffraction pattern. Since this example only uses two rows of atoms, the transition from constructive to destructive interference as θ changes is gradual. However, if interference from many rows occurs, then the constructive interference peaks become very sharp with mostly destructive interference in between. This sharpening of the peaks as the number of rows increases is very similar to the sharpening of the diffraction peaks from a diffraction grating as the number of slits increases. With this, a diffraction pattern is obtained from the measurements of the intensity of scattered waves as a function of the scattering angle. The very strong intensities that are seen are known as Bragg peaks and these are obtained in the diffraction pattern when scattered waves satisfy Bragg's Law [1].

2.2.2 Raman Spectroscopy

Raman spectroscopy is a powerful technique for studying the correlation of electrons in multiferroic materials. This technique is non-invasive that helps

determine the temperature of the transition, the size of the crystals, the doping, phase change, and elasticity of ferroelectric. This technique is based on irradiating the sample with photons from a monochromatic laser source. Elastic dispersed photons leave the sample (see Figure 2.2 a)), or inelastic (see Figure 2.2 a) and b)). The process where scattered electrons have the same frequency as the source electrons is called Rayleigh scattering and the inelastic processes where the frequency of the output photon is less than the frequency of the source photon is called Stokes Raman scattering and the process where the frequency is higher than that of the source photon is called Anti-Stokes Raman scattering. The difference in frequency in this technique is named as Raman shift.

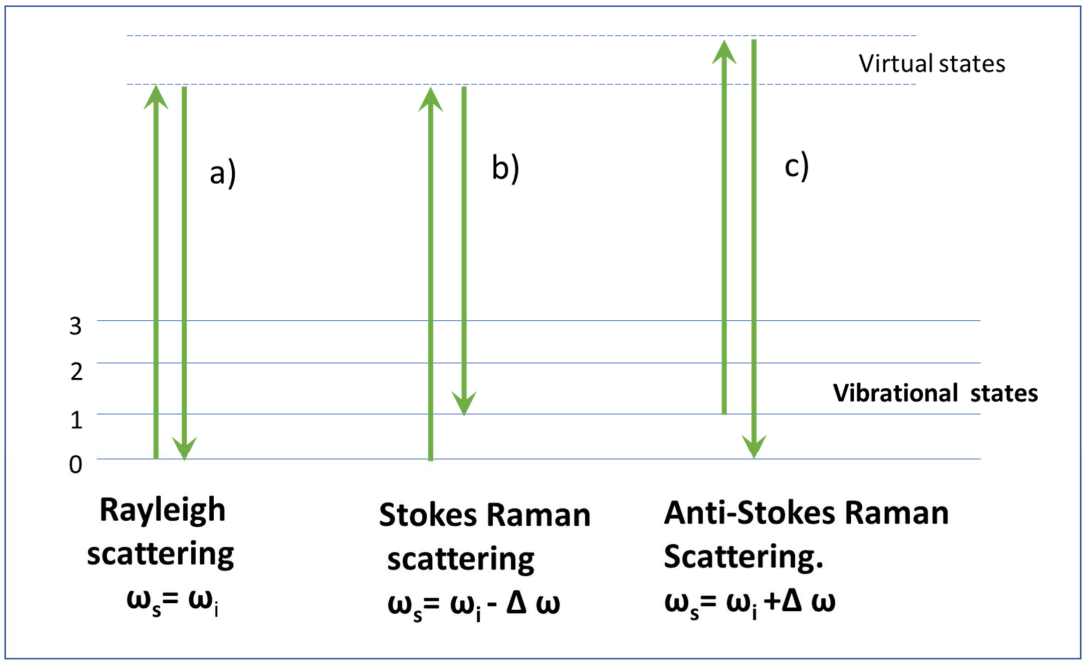

Figure 2.2: Diagram of Raman and Rayleigh scattering processes.

When an alternating electromagnetic field (photon) collides with the sample, the molecules in this sample deform and change their dipole moment depending on how the electronic cloud reacts around them. The polarization of the molecule

depends on the electric field as follows:

$$P = \alpha E \tag{2.7}$$

where α is the dipole moment polarizability and E is the electric field. The Raman scattering process can be explained by classical theory.

The alternating electromagnetic field of the incident radiation in the sample can be represented as:

$$E = E_0 cos(2\pi\nu_0 t) \tag{2.8}$$

Here ν_0 is the frequency of the field and substituting 2.8 in 2.7 we have:

$$P = \alpha E_0 cos(2\pi\nu_0 t) \tag{2.9}$$

We cannot forget that polarizability depends on the type of bond as well as the structure of the material. This is why the material has its own vibrational frequency (ν_v) in response to the frequency of the external field. So the displacement of the atoms from the equilibrium of a particular vibrational mode can be written as:

$$dq = q_0 cos(2\pi\nu_v t) \tag{2.10}$$

where q_0 is the vibrational amplitude and the vibrational energy of this particular vibrational mode is:

$$E_v = (J + 1/2)\hbar\nu_v \tag{2.11}$$

where J is the vibrational quantum number. For very small displacement

we can use a Taylor series expansion to approximate the polarizability and we keep only the first term of it.

$$\alpha = \alpha_0 + \frac{\partial \alpha}{\partial q} dq \tag{2.12}$$

Where α_0 is polarizability at equilibrium position. Solving and combining the equations 2.9, 2.10, 2.11 and 2.12 give us:

$$P = \alpha_0 E_0 cos(2\pi\nu_0 t) + (\frac{\partial \alpha}{\partial q}\frac{q_0 E_0}{2})[\cos 2\pi(\nu_0 + \nu_v) + \cos 2\pi(\nu_0 - \nu_v)] \tag{2.13}$$

In the equation 2.13 we can find three different frequency of the different king of scattering. The frequencies ν_0 correspond to Rayliegh-, $\nu_0 + \nu_v$ to anti-Stokes- and $\nu_0 - \nu_v$ to Stoke- scattering. The samples are Raman active only if $\frac{\partial \alpha}{\partial q} \neq 0$ [2,3]. In general, the Raman spectrometry technique has four main parts. The laser, which is the source of photons that excite the sample, the lighting system of the sample and the optics needed to collimate the laser, the wave filter to use monochromatic light, and the detector of the photons diffracted by the sample. The sample is illuminated by a wave of monochromatic light from a laser with energy in the infrared, visible, or ultraviolet spectrum. The Raman spectrum is obtained from the process of scattering of the incident rays in the sample in backscattering geometry through a microscope.

2.2.3 Scanning Electron Microscopy (SEM)

Scanning electron microscopy is the technique used in our work to study morphology, topography and using this technique in another mode (EDS), it also gives us the chemical composition of the material with a high resolution. In

the Figure(2.3) you can see a diagram of the principal parts of the SEM where the electron beam of the source is accelerated in a high electric field in the direction of the sample [4].

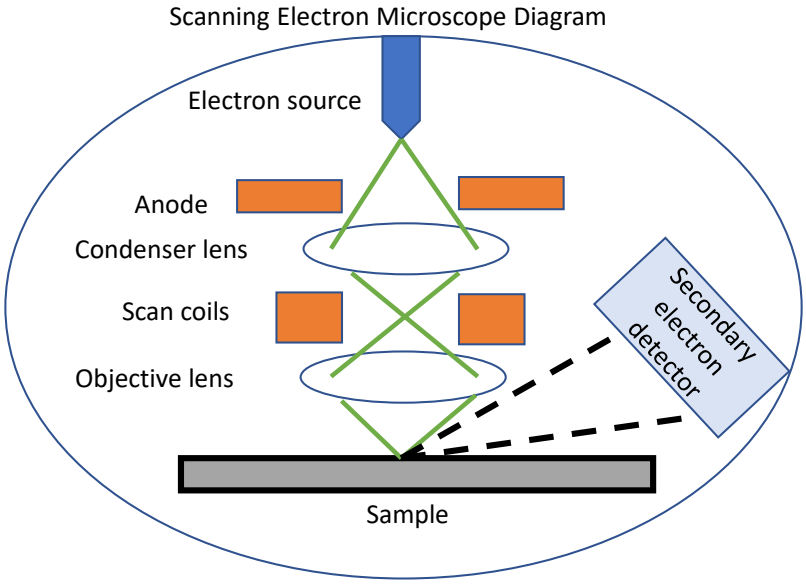

Figure 2.3: Scanning electron microscope diagram.

These electrons, which are at high vacuum, are focused by electric lenses to concentrate the electron beam when interacting with the object. This interaction between the electrons and the sample can be seen in Figure(2.4).

The voltage between the cathode and the anode is 0.5 to 30 kV. In the interaction of the electron beam with the object studied excitation of different types of signals occurs. The scattered secondary electrons emitted by the sample are collected in a detector that simultaneously produces an electronic signal. This signal is amplified and transformed in a scan image that is seen on the monitor.

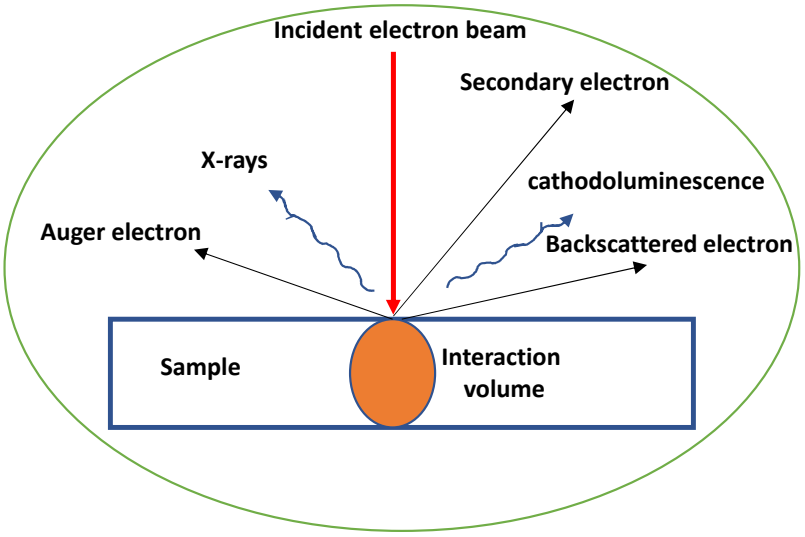

Figure 2.4: Electron-sample interaction in SEM.

2.2.4 Energy Dispersive Spectroscopy (EDS)

The EDS technique is used to identify and quantify the elementary composition in our material. This sample is a special case of SEM, and an X-ray detector can analyze all emissions diffracted by the sample. This technique is a surface analysis technique and making an analysis of the energy of the diffracted X-rays can be attributed to the atoms that are in the sample and thus the composition of it.

2.2.5 X-ray Photoelectron Spectroscopy (XPS)

X-ray Photoelectron Spectroscopy (XPS) is a surface-sensitive technique which is also well known as electron spectroscopy chemical analysis (ESCA), is the most widely surface analysis technique because it can be applied for a broad range of materials and provides the information about the chemical composition and quantitative information from the surface of the material [5, 6]. It works

on basis of the photoelectric effect (Figure 2.5) and the corresponding relation between the kinetic energy (KE) and binding energy (BE) is showed in Equation 2.14. The surface analysis by XPS is typically done by the sample irradiation with a monochromatic x-ray source. The x-ray sources like Al Kα (1486.7 eV) and Mg Kα (1253.6 eV) are typically used for the XPS analysis. The average penetration depth of analysis is limited by 5 nm and the lateral space resolution is as small as 7-8 μm. The penetration depth also depends on the angle of incidence, material, and incident photon energy. The irradiated photons will interact with the atoms on the surface and emit the electrons by means of the photoelectric effect. The KE of the emitted electrons is analyzed by the electron spectrometer which is also dependent on the incident photon energy.

$$BE = h\nu - KE_K - \phi, \tag{2.14}$$

where ϕ is the work function of the spectrometer, $h\nu$ is the incident photon energy, E_B is the binding energy or ionization potential, and E_K is the kinetic energy of the ejected electrons. The basic requirements for the XPS measurements are

(i) fixed-energy radiation source, an x-ray source of Al Kα or Mg Kα is needed.

(ii) An electron energy analyzer, to disperse the emitted electrons according to their KE, and to measure the flux of emitted electrons of any specific energy.

(iii) ultra high vacuum environment, the typical vacuum in the XPS chamber is below 10^{-9} Torr. This high vacuum environment is required in the XPS chamber to avoid contaminations on the active surface, to extend the life of the X-ray source and other electronic optics inside the chamber, and also to enable the emitted photoelectrons to be analyzed without interference from the gas

phase collisions.

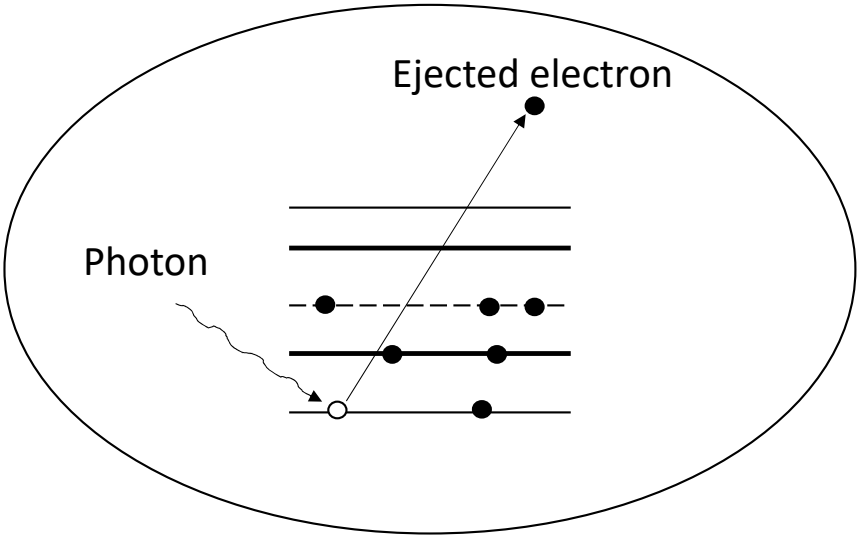

Figure 2.5: Typical photoexcitation process.

The typical XPS spectra is a plot of the emitted photoelectron intensity as a function of the binding energy. The step-like background is very common in the XPS spectra and a series of peaks will be observed on the background. The XPS spectra generally show the step-like increase in the background is due to the Bremsstrahlung radiation. Each XPS peak has a higher background at the high binding energy side compared with the low binding energy side, which confirms the asymmetric nature of the peak. The origin of the XPS background is extrinsic and intrinsic losses and is important to study the depth and lateral distribution of elements. The peaks from C1s are considered as the reference peak in all cases irrespective of the material type and system. The change in the binding energy of a core electron of an element is due to the change in the chemical bonding of that particular element. The shift in the XPS peak and full width at half maxima (FWHM) are the interesting features in XPS spectra

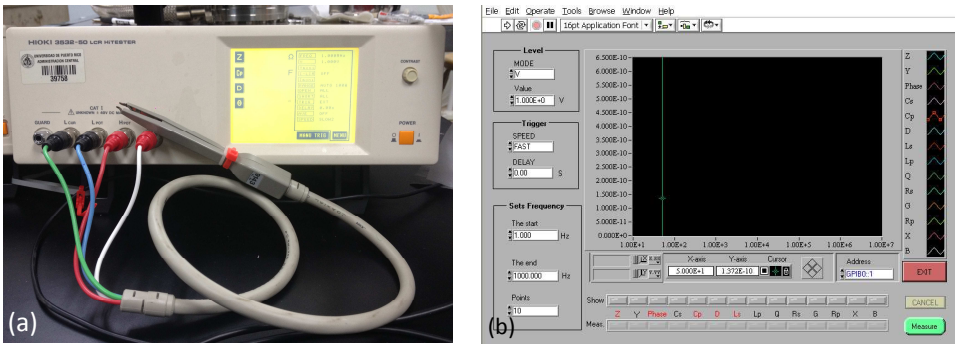

Figure 2.6: (a) HIOKI LCR meter (b) LABVIEW program used for electric and dielectric measurements.

which depend on the various factors like nature of the bonding, type of analyzer, material, and type of the incident wavelength, etc. The broadening of the XPS peaks can be minimized by using the monochromator by which the FWHM can reduce by more than half. Insulating samples give broader peaks in XPS and high background due to the charging effects. The lifetime of core-hole created, inhomogeneity in the samples are very-well known intrinsic properties apart from the before mentioned extrinsic factors which cause the broadening in the XPS peaks.

The recorded spectra are imported into CASAXPS software and analyzed the data. The quantitative analysis and elemental composition was studied by using the CASAXPS. The XPS analysis is a surface characterization technique that does not cause any damage to the surface under irradiation for the investigation; thus this technique is found to be ideal and suitable to examine the surfaces of our samples.

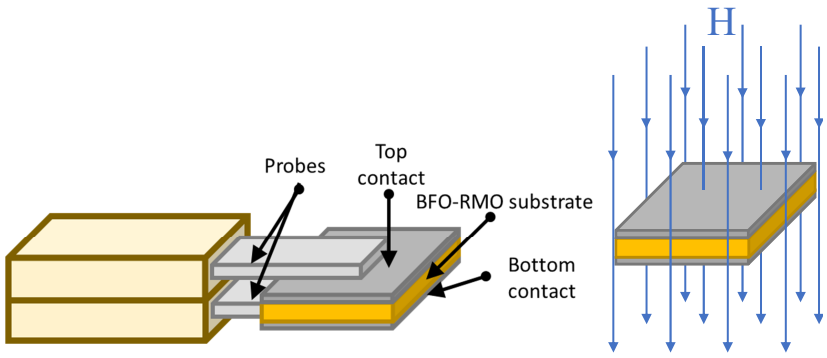

Figure 2.7: (left) Schematic of dielectric measurement using parallel plate capacitor configurations and (right) the capacitor inside an applied magnetic field.

2.2.6 Dielectric properties

The samples were measured using the HIOKI 3532-50 LCR HiTESTER from the HIOKI E.E. Corporation with tweezers probe as shown in Figure 2.6. The HIOKI 3532-50 LCR HiTESTER is an impedance meter that uses a touch panel as a user interface and has PC connectivity through GP-IB. The equipment has a frequency range of 42 Hz up to 5 MHz at high resolution. The values measured were capacitance, impedance, dielectric loss, and phase angle. It performs all the measurements simultaneously. The sample was mounted on the tweezers, as shown in the diagram (left) of Figure 2.7 and as well subjected to magnetic fields [7].

The dielectric permittivity measurements were obtained from the capacitance measurement.

$$C = \kappa' C_0 \tag{2.15}$$

As we know, the HIOKI 3532-50 LCR HiTESTER measures the overall capacitance of the sample, where we want to obtain the dielectric permittivity of the sample. For this we have to use the relation with Equation 2.15 and solving

for κ' we have:

$$\kappa' = \frac{C}{C_0} \tag{2.16}$$

Considering that the capacitance of a capacitor with an area 'A' and a plate separation of 'd', with the separation being vacuum, we have:

$$C_0 = \frac{\epsilon_0 A}{d} \tag{2.17}$$

Inserting Equation 2.17 into Equation 2.16, we have the dielectric permittivity of the material with respect of the measured capacitance 'C', the area 'A', and space between plates 'd' obtaining:

$$\kappa' = C\frac{d}{\epsilon_0 A} \tag{2.18}$$

These are all obtainable values, with the dielectric constant of vacuum being ϵ_0=8.854×10^{-12} F/m, the capacitance is obtained from the HIOKI 3532-50 LCR HiTESTER capacitance output, the distance between plates is obtained from the sample size values and the area obtained by measuring the sputtered area on the sample.

Dielectric materials have been studied extensively because of their applications in electronic devices, data, and energy storage. Some of the applications for which dielectric materials are being studied and utilized include, dielectric resonators, protective industrial coatings, cooling, and insulator for capacitors and other materials [8]. The most basic shape of a capacitor is two metal plates divided by either space (air or vacuum), or a non-conductive insulating material; as shown in Figure 2.8. This insulating material can be such as paper or plastic between the plates. Such material, called a dielectric, can be used to maintain

a physical separation of the plates. There are two types of dielectrics. The first type is polar dielectrics, which are dielectrics that have permanent electric dipole moments. The orientation of polar molecules is random in the absence of an external field. When an external electric field $\mathbf{E_0}$ is present, a torque is set up and causes the molecules to align with $\mathbf{E_0}$. However, the alignment is not complete due to random thermal motion. The aligned molecules then generate an electric field that is opposite to the applied field but smaller in magnitude. The second type of dielectrics is non-polar dielectrics, which are dielectrics that do not possess permanent electric dipole moment. Electric dipole moments can be induced by placing the materials in an externally applied electric field.

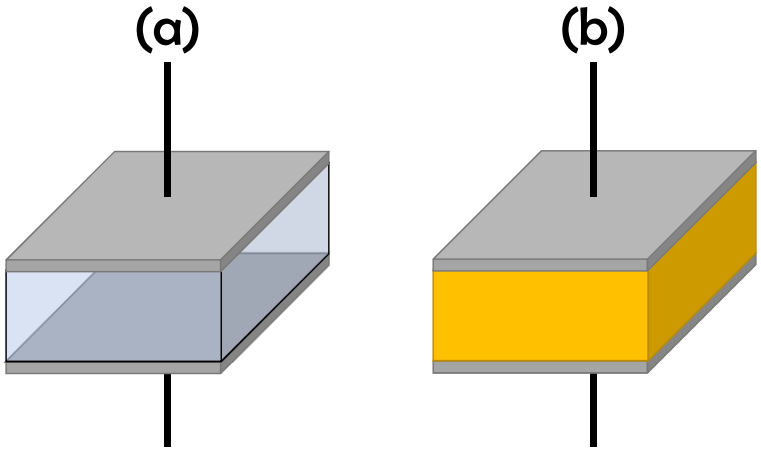

Figure 2.8: Basic capacitor structure with (a) free space between plates and (b) a dielectric material between plates.

There are certain properties for a dielectric material within a capacitor that are of interest to determine the compatibility of the dielectric for certain applications and its value for it as a viable solution to certain utilities within those applications. The properties that were specially measured and studied in detail were basic frequency-dependent measurements for dielectrics in capacitors, such as dielectric permittivity, phase angle, impedance, and loss coefficient ($\tan(\delta)$).

Each property will be discussed further in this chapter and the importance of their behavior with frequency dependency.

2.2.6.1 Dielectric Permittivity

The definition of dielectric constant relates to the permittivity of the material itself. The symbol commonly use is the Greek letter ϵ, with ϵ_0 being the dielectric permittivity constant in vacuum, which has a value of ϵ_0=8.854x10^{-12} F/m. This is the lowest value possible. The permittivity tells us how the polarization of material responds when a field it's applied. The dielectric permittivity corresponds to the ratio of the permittivity of the dielectric material to that of the permittivity of vacuum. This means that the greater the polarization that the material can achieve within an applied field of a certain magnitude, the greater the dielectric constant will be. This means that greater the dielectric permittivity of the material will give us a better ability to store energy inside the capacitor, in other words, better capacitance [9]. Analyzing a simple capacitor that is connected to a sinusoidal voltage source (AC source) we have:

$$\mathbf{V} = \mathbf{V}_0 e^{j\omega t} \tag{2.19}$$

Having an angular frequency of ω=$2\pi\nu$, when the capacitor has a vacuum as the separation between the plates [Figure 2.8(a)], then it will store a charge Q=$C_0\mathbf{V}$, and draw a charging current as:

$$I_c = \frac{dQ}{dt} = j\omega C_0 \mathbf{V} \tag{2.20}$$

This current, to be a true capacitor, leads the voltage by a temporal phase of 90°. In Figure 2.9 we can visualize this as vectors. C_0 is the capacitance

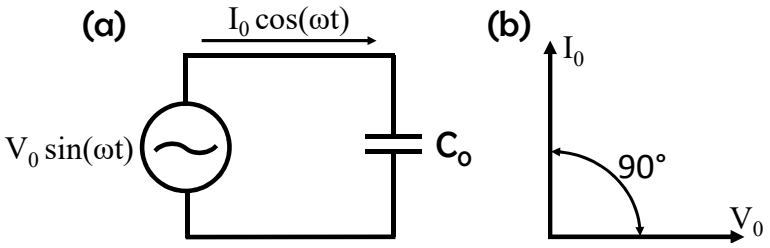

Figure 2.9: The current-voltage relationship of an ideal capacitor.

in vacuum, of the capacitor. When the capacitor has a material, other than vacuum, then the capacitance increases to:

$$C = C_0 \frac{\epsilon'}{\epsilon_0} = C_0 \kappa' \tag{2.21}$$

Here we designate ϵ' as the real dielectric permittivity or dielectric constant of the dielectric and ϵ_0 of vacuum. Their ratio is κ', which is the relative dielectric constant of the material. Utilizing the relative permittivity ϵ^*=ϵ'-jϵ", we can calculate the electric modulus, where we have [10]:

$$M^* = M' + jM'' = \frac{1}{\epsilon^*} \tag{2.22}$$

With this we simplify the modulus in terms of the dielectric permittivity:

$$M^* = \frac{1}{\epsilon^*} = \frac{1}{\epsilon' - j\epsilon''} \cdot \frac{1}{1} = \frac{1}{\epsilon' - j\epsilon''} \cdot \frac{\epsilon' + j\epsilon''}{\epsilon' + j\epsilon''} = \frac{\epsilon' + j\epsilon''}{\epsilon'^2 + \epsilon''^2} \tag{2.23}$$

This gives us the complex modulus in terms of the dielectric permittivity with the real and imaginary parts as:

$$M^* = \frac{\epsilon'}{\epsilon'^2 + \epsilon''^2} + j\frac{\epsilon''}{\epsilon'^2 + \epsilon''^2} = M' + jM'' \tag{2.24}$$

Utilizing the complex modulus formula we can conveniently use this tool as

an alternative for impedance spectroscopy with some additional advantages compared to what we can find with complex impedance spectroscopy, which helps in determining, analyzing, and interpreting the dynamical aspects of electrical transport phenomena. This tool provides an insight into the electrical processes characterized by the smallest capacitance of the material. To truly analyze and interpret the experimental data, it is important to have a model equivalent circuit that will provide a realistic representation of the electrical properties of the sample. The complex modulus representation helps suppress the unwanted effects of extrinsic relaxation, which is often used while analyzing the dynamic conductivities of ionic conducting glasses and in the analysis of dielectric data of ionic conductors [11]. The advantage of adopting complex electrical modulus spectra is that it can discriminate against electrode polarization and grain-boundary conduction process [12, 13].

2.2.6.2 Phase angle

As it was observed in Figure 2.9(b), when capacitors, and similar to inductors, are connected to a sinusoidal voltage source, the current and voltage crests don't peak at the same time. There is a fraction of a temporal phase difference between the peaks of the voltage and current. This is expressed in degrees and is referred to as a phase difference. This phase angle is ≤ 90 degrees. Normally, the point of reference is the angle by which the voltage leads the current. This translates to having a negative phase angle for circuits with the presence of a capacitor since the current leads the voltage. The phase angle becomes positive when the circuit system has the presence of an inductor, where the voltage leads the current. This is visualized in Figure 2.10.

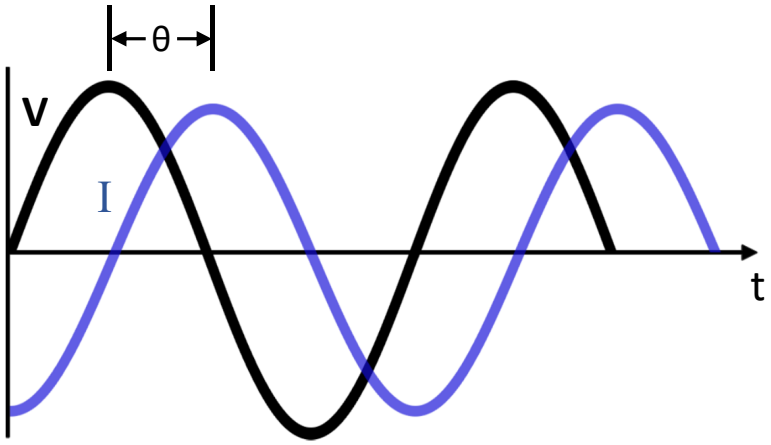

Figure 2.10: Phase angle shift between the voltage and current.

2.2.6.3 Loss coefficient

Alongside the charging current component I_c, we have a loss current component (I_l=$G\mathbf{V}$) in phase with the voltage. G represents the conductance of the dielectric. Then, the total current of the capacitor becomes:

$$I = I_c + I_l = (j\omega C + G)\mathbf{V} \tag{2.25}$$

This current is inclined a power factor angle $\theta < 90°$ against the applied voltage $\mathbf{V}$. This is the loss angle δ against the $+j$-axis. If we consider that the dielectric material acts upon the system as a circuit of a capacitor paralleled by a resistor (RC) then the frequency response of the circuit is expressed as the ratio of the charging current and loss current. In this case, we call the dissipation factor D, or as well as the loss tangent:

$$D = \tan\ \delta = \frac{I_l}{I_c} = \frac{1}{\omega RC} \tag{2.26}$$

This dielectric loss results from the inability in the polarization process with

the molecules to follow the rate in which the oscillating applied field changes. This comes with the relaxation time (τ) of the material. This is the time taken for the dipoles to return to their original orientation, in simple terms, the time for the material to relax after the applied field is gone or changed. If the relaxation time is smaller or comparable to the rate of the oscillating electric field, then there would be no or minimum loss. Then, if the rate of change of the electric field oscillates faster than the relaxation time of the material, then the polarization cannot occur completely and can't follow the oscillating frequency resulting in energy absorption and dissipation as heat.

Important relations that we can have from the loss coefficient are as well:

$$\tan\ \delta = \frac{\epsilon''}{\epsilon'} = \frac{M''}{M'} = \frac{Z'}{Z''} = \frac{Y''}{Y'} \tag{2.27}$$

2.2.6.4 Impedance

Circuits that are based on Direct Current (DC) sources, can be described only by the resistor elements within. Capacitors on a DC circuit are basically open connections, as an infinite value resistor, and an inductor is simply a short connection that acts as a resistor of zero value. When we enter to AC circuits, when an element opposes the current flow, the measure of this is called impedance. We have again the play between the current-voltage ratio with frequency dependence. The impedance has to be expressed as a complex quantity, meaning it has a real and imaginary part as:

$$Z = R + jX \tag{2.28}$$

The real part of the impedance is the resistance (R) and the imaginary part is the reactance (X). Here the resistance is always positive, where the reactance

can be either positive or negative. Where the resistance dissipates power as heat, the reactance stores energy as an electric or magnetic field. In a capacitor, as observed in Figure 2.10, representing the fact that in a capacitor the current leads the voltage by 90°, then the impedance can be represented as:

$$Z_C = -j\frac{1}{\omega C} \tag{2.29}$$

Here Z_C is the impedance of the capacitor, ω is the angular frequency, where $\omega = 2\pi f$, and f is the frequency of the signal. The capacitance of the capacitor is C. With this we can observe that the resistance of an ideal capacitor should have a value of zero, the reactance is negative for all frequency. The effective impedance of a capacitor is dependent on the frequency, and for an ideal capacitor, it should decrease with frequencies.

Furthermore, if we utilize the complex impedance spectroscopy, where we use both real and imaginary parts of the total impedance, we have a powerful tool for characterizing many of the electrical properties of materials and the interfaces with the conducting electrodes. This method can be used to investigate the dynamics of bound or mobile charges in the bulk or the interfacial regions of any kind of solid or liquid material, including insulators (dielectrics). With the complex impedance spectroscopy we can find an equivalent circuit based on impedance and electric modulus spectra which provides an idea of the physical processes that occur inside the sample. Most of the known ceramics contain grains and grain-boundary regions, this has very different physical properties individually. These regions can be observed within the impedance and modulus spectra. The electrical properties of the present material system have been investigated using this complex impedance spectroscopy technique.

2.2.7 Electrical properties

Understanding the current-voltage (I-V) characterizes of BFO_{1-x}-GMO_x and BFO_{1-x}-DMO_x bulk samples is critical for many electronic device applications. The schematic of our electrical measurement is shown in Figure 2.11. The electrical measurement were done using our in-house electrical measurement system (see Figure 2.12)

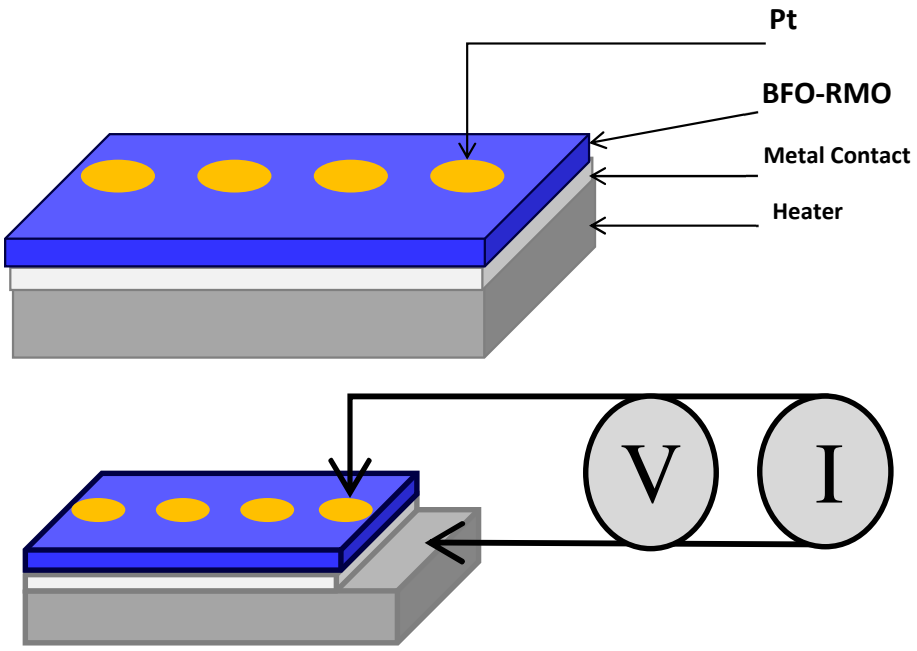

Figure 2.11: Schematic of electrical measurement.

There are different conduction mechanisms depending on the behavior of materials to the current-voltage relationship. The basic mechanism is the ohmic behavior, which is a linear relationship between the current-voltage curve. There are other current-voltage conduction mechanisms, such as Schottky Emission, Poole-Frenkel, Fowler-Nordheim, and the Space-charge-limited current. The mathematical representations of this behavior in the current-voltage curves are:

Schottky Emission:

$$J_{Sch} = A^* T^2 e^{\frac{-q(\Phi_b - \sqrt{\frac{qE}{4\pi\varepsilon_r\varepsilon_0}}))}{K_b T}} \tag{2.30}$$

where

$$A^* = \frac{4\pi q K_b^2 m^*}{h^3}$$

$$A^* = 120\frac{m^*}{m_0}$$

J: leakage current density, E: applied electric field, e: elementary charge, T: temperature, k: Boltzmann's constant, A* is the effective Richarson constant, m_0 the free electron mass, m^* the effective electron mass in the dielectric, $q\Phi_b$ the Schottky barrier high, ε_0 permittivity of free space, and

$$\varepsilon_r = \varepsilon_\infty = n^2$$

is the optic dielectric constant.

Poole-Frenkel:

$$J_{PF} = BEe^{\frac{-(\phi_t - e\sqrt{eE/\pi\varepsilon_r\ \varepsilon_0})}{kT}} \tag{2.31}$$

J_{PF}: leakage current density, B: constant, E: applied electric field, ϕ_t trap ionization energy, e: elementary charge, T: temperature, k: Boltzmann's constant, ε_0: permittivity of free space, ε_r: optical dielectric constant.

Fowler-Nordheim:

$$J_{FN} = \frac{q^2}{8\pi h\phi_b} E^2 e^{\frac{-8\pi(2qm_T^*)^{1/2}}{3hE}\phi_b^{\frac{3}{2}}} \tag{2.32}$$

where m_T^* is the tunneling effective mass in dielectric and h the Planck constant, J_{FN}: leakage current density, E: applied electric field, ϕ_b: potential barrier height, e: elementary charge, m*: effective electron mass, and $\hbar$: Planck's constant.

Space-Charge:

$$J = (9/8)\mu_0\epsilon_s\epsilon_0 E^2/d \tag{2.33}$$

where, J: leakage current density, E: applied electric field, ε_0: permittivity of free space, ε_r: relative dielectric constant of thin film.

Hoping conduction:

$$J_h = qa\eta\nu e^{(\frac{qaE}{k_bT} - \frac{E_a}{k_bT})} \tag{2.34}$$

Where a is the mean hopping distance, η is the electron concentration in the conduction band, ν is the frequency of the thermal vibration of electron, and E_a the activation energy.

2.2.8 Magnetic properties

The magnetic element of new materials has come to a very important level since the same composite material can be "tuned" by just applying a magnetic presence into it. This gives a material that can be switched depending on the presence and strength of this external field, and as well, this material can act as a sensor due to magnetic presence. With this in mind, we need to have a magnetic element present in the material studied, and since this is a Multiferroic, we have two components present: the ferroelectric and the ferromagnetic. Both are coupled and when one is affected the other is too. Iron (Fe), Cobalt (Co), Nickel (Ni), and some rear earth are elements highly affected by the magnetic

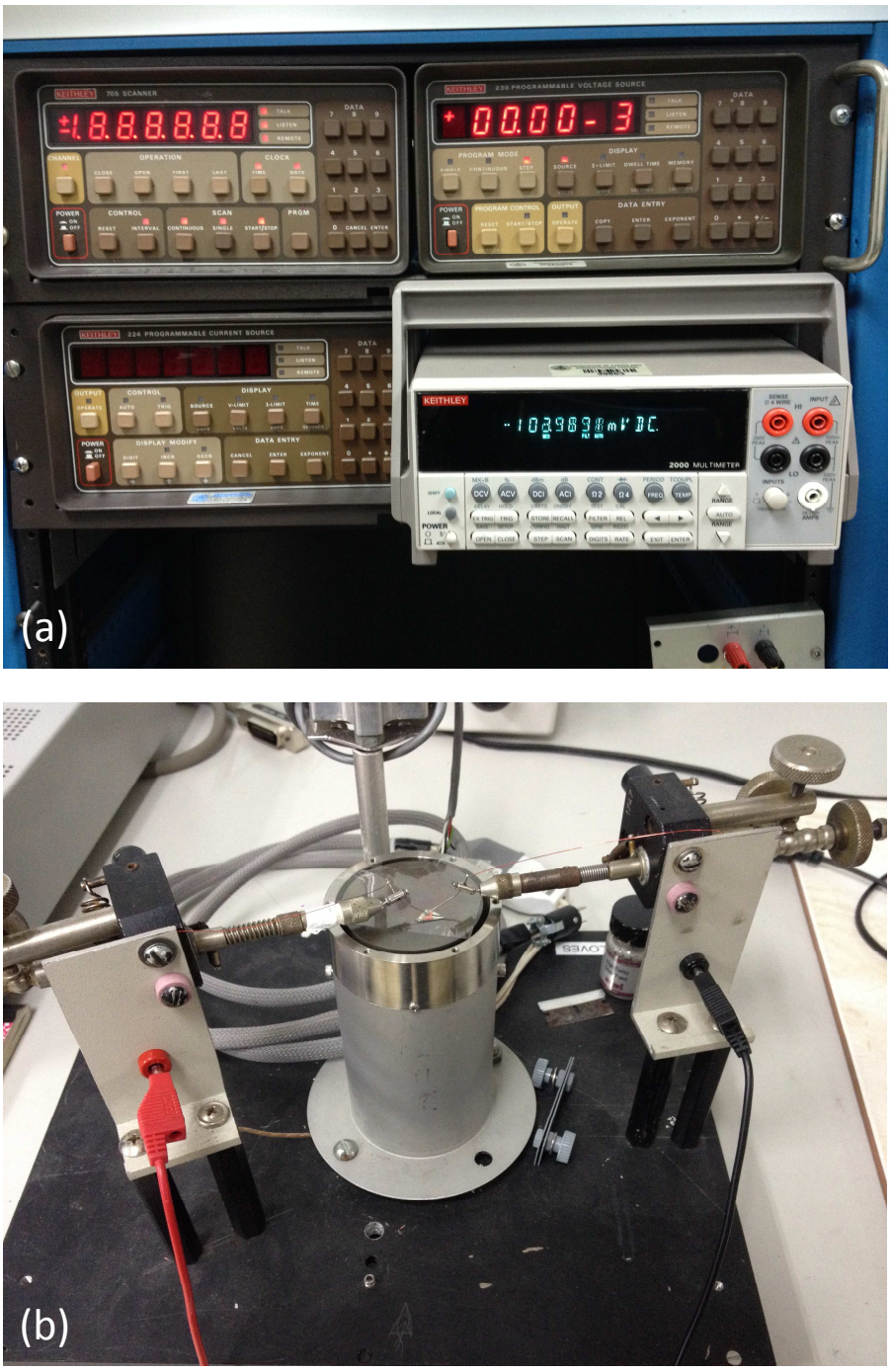

Figure 2.12: The electrical measurement setup in our Laboratory that used in the present work.

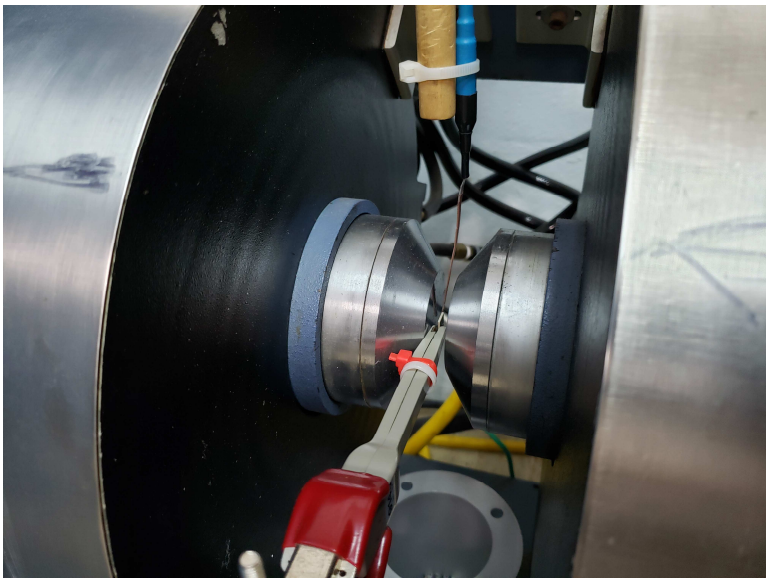

Figure 2.13: HIOKI (frequency dependent measuring machine) with tweezers holder suspending a substrate inside the electromagnet with magnetic field strength sensor.

presence, and coupled with our ferroelectric $BiFeO_3$ we want to know how and how much does the magnetic element coupled interacts with the total outcome of the composite. With this in mind, we place the samples inside a magnetic field that we can control and measure all the data points at different magnetic field strengths to determine the interaction of the magnetic-ferroelectric coupling. In Figure 2.13, we observe a sample being held by the tweezers attachment of the HIOKI Hi-Tester, which does the dielectric measurements, inside the electromagnet that has a maximum magnetic field capacity up to 2 Tesla (T). The measurements were carried out in an up and down magnetic field starting from 0 T (no magnetic presence) up to 2 T, and back down to 0 T with increments of 0.25 T.

References

[1] B. E. Warren. *X-Ray Diffraction*, Courier Corporation, (1969)

[2] John R. Ferraro, Kazuo Nakamoto, and Chris W. Brown, Introductory Raman Spectroscopy, Second edition, Elsevier (2003)

[3] Ewen Smith, Geoffrey Dent, Modern Raman Spectroscopy - A Practical Approach, Wiley & Sons (2005)

[4] P. J. Goodhew, J. Humpphreys and R. Beanland, Electron Microscopy and Analysis, Taylor and Francis (2001)

[5] M. Prutton, *Surface Physics* New York : Oxford University Press, (1983)

[6] J. F. Watts, *An Introduction to surface Analysis by XPS and AES* John Wiley & Sons Ltd.(2003)

[7] HIOKI Instruction Manual, Hioki E.E. Corporation (2008)

[8] A. R. von Hippel, S. O. Morgan, Dielectric Materials and Applications. Journal of The Electrochemical Society. **102** 68C (1955)

[9] A. R. Von Hippel, Dielectric Materials and Applications, MIT Press and John Wiley & Sons inc. (1954)

[10] A.K. Roy, K. Prasad, A. Prasad, Electrical Conduction in $(Na_{0.5}Bi_{0.5})_{1-x}Ba_xTiO_3$(0=x=1) Ceramic by Complex Impedance/Modulus Spectroscopy, ISRN Ceram. **2013** 112 (2013)

[11] N. G. McCrum, B. E. Read, and G. Williams, Anelastic and Dielectric Effects in Polymeric Solids, John Wiley & Sons, New York, NY, USA, (1967)

[12] C. T. Moynihan, Analysis of electrical relaxation in glasses and melts with large concentrations of mobile ions, Journal of Non-Crystalline Solids, vol. 172174, no. 2, pp. 13951407, (1994)

[13] C. T. Moynihan, L. P. Boesch, and N. L. Laberge, Decay function for the electric field relaxation in vitreous ionic conductors, Physics and Chemistry of Glasses, vol. 14, no. 6, pp. 122125, (1973)

Chapter 3

Structural and magnetodielectric properties of BFO-GMO multiferroics

We report on structural, microstructural, spectroscopic, dielectric, electrical, ferroelectric, ferromagnetic, and magnetodielectric coupling studies of $BiFeO_3$-$GdMnO_3$[BFO_{1-x}-GMO_x], where x is the concentration of $GdMnO_3$ (x= 0.0, 0.025, 0.05, 0.075, 0.1, 0.15, and 0.2), nanocrystalline ceramic solid solutions by auto-combustion method. The analysis of structural property by Rietveld refinement shows the existence of morphotropic phase boundary (MPB) at x=0.10, which is in agreement with the Raman spectroscopy and high resolution transmission electron microscopy (HRTEM) studies. The average crystallite size obtained from the transmission electron microscopy (TEM) and X-ray line profile analysis was found to be 20-30 nm. The scanning electron micrographs show the uniform distribution of grains throughout the surface of the sample. The dielectric dispersion behavior fits very well with the Maxwell-Wagner model. The frequency dependent phase angle (θ) study shows the resistive nature of solid solutions at low frequency, whereas it shows capacitive behavior at higher frequencies. The temperature variation of dielectric permittivity shows dielectric anomaly at the magnetic phase transition temperature and shifting of the phase transition towards the lower temperature with increasing GMO concentration. The

Nyquist plot showed the conduction mechanism is mostly dominated by grains and grain boundary resistances. The ac conductivity of all the samples follows the modified Jonscher model. The impedance and modulus spectroscopy show a non-Debye type relaxation mechanism which can be modeled using a constant phase element (CPE) in the equivalent circuit. The solid-solutions of BFO-GMO show enhanced ferromagnetic-like behavior at room temperature. The ferroelectric polarization measurement shows lossy ferroelectric behavior. The frequency dependent magnetocapacitance and magnetoimpedance clearly show the existence of intrinsic magnetodielectric coupling. The BFO_{1-x}-GMO_x solid solutions with x= 0.025-0.075 show significantly higher magnetocapacitance and magnetoimpedance compared to the pure BFO.

3.1 Introduction

Multiferroic materials are attracting a great deal of interest because of their unusual interesting physical properties, such as coexistence of multiple switchable states (polarization, magnetization or strain), magnetoelectric (ME) coupling, structural phase transitions, and their potential applications in secure data storage, spintronics, and novel multifunctional devices [1–8]. The information stored by splitting data in multiferroic memory over two mediums (half stored electrically and half stored magnetically) could be encrypted in such a way that makes it for more secure than is currently possible, which will open up a new era in data storage.

$BiFeO_3$ (BFO) is a rare Pb-free room temperature (RT) single-phase multiferroic (ferroelectric T_c = 850°C and antiferromagnetic T_N = 370°C [4–6]. However, high leakage current, weak magnetoelectric coupling, presence of cy-

cloidal spin spiral, and critical structural stability of BFO are the bottlenecks for practical applications [9, 10]. BFO, which is Type-I multiferroics, showed large ferroelectric polarization due to *charge ordering* and displacement of ions because of lattice distortion, but it shows weak ME coupling. However, in Type-II multiferroics, the polarization is due to certain *magnetic ordering* and is of electronic in origin, but it shows stronger ME coupling than Type-I multiferroics [11]. The objective of this present work is to affect the ferroic orderings of BFO to enhance the ME coupling.

It has been found that solid-solutions of BFO with rare-earth (RE) manganite $REMnO_3$ (RE= Dy, Sm, La, Gd, Y, *etc.*) [4] can stabilize the crystal structure, reduce the leakage current, suppress the spiral spin structure of BFO, and can facilitate the release of latent magnetization [1, 2]. RE elements show a large net magnetic moment which originates from the electrons of unfilled $4f$ shells due to both orbital and spin magnetic moments. The $4f$ electrons (deep shell) are very localized and shielded by s and p orbital from other ions in the field. Therefore, the orbital moments of rare-earth ions remain unquenched. $GdMnO_3$ (GMO), a magnetoelectric with an incommensurate antiferromagnetic phase transition at $T_N \sim$ -230°C (43 K), which is associated with the sinusoidal antiferromagnetic ordering of the Mn^{3+} ions magnetic moment. GMO shows a strong lattice modulation due to the correlation between electric and magnetic orders and strong spin-lattice coupling between Gd $4f$-spin sublattice with Mn $3d$ spin. As the ME coupling interlinked with spin-charge-lattice interactions, it is expected that the substitution of Gd^{3+} (effective magnetic moment, $\mu_{\text{eff}} = 7.9\mu_B$) at Bi-site of the BFO can switch off the lone pair activity of Bi leading to shift the ferroelectric phase transition towards closer to (anti)ferromagnetic phase transition and resulting a stronger ME coupling [6].

A strong ME coupling between magnetization (M) and polarization (P) has not been achieved in BFO because of the problem to sustain the high electric field necessary to switch the magnetization. The enhancement in multiferroic properties of BFO has been observed by synthesizing nanoparticles smaller than spin cycloid (60 nm) due to the size effect. In multiferroics, M couples to P and thus to the dielectric constant (ε). We propose to study the ME coupling through the magnetodielectric (MD) effect. The dielectric constant relates to the index of the refraction (η) of the material; $\eta = (\mu\varepsilon)^{1/2}$, where μ and ε are the permeability and permittivity of the material, respectively. The tuning of refractive index by the application of a magnetic field would give rise a novel functionality to magnetoelectric and magneto-optic devices. However, there many unanswered questions need to be addressed: What is the mechanism that gives rise to MD coupling? Why and under what circumstances a large MD coupling should exist and how to control it? What are the effects of temperature, frequency, interface, and electromagnetic field on MD coupling? What is the influence of the strain effect, size effect, and reduced dimensionality on MD coupling? In order to understand and enhance the MD coupling of BFO, we carried out a systematic study of BFO_{1-x}-GMO_x solid-solutions. In this present work, we report on structural, microstructural, spectroscopic, dielectric, electrical, ferroelectric, ferromagnetic, and magnetodielectric properties of BFO_{1-x}-GMO_x, where x = 0.0, 0.025, 0.05, 0.075, 0.1, 0.15, and 0.2, nanocrystalline ceramics by auto-combustion method.

3.2 Experimental details

Nanocrystalline ceramic solid solutions of BFO_{1-x}-GMO_x ($0.0 \leq x \leq 0.2$) were synthesized using analytical grade chemicals of $Fe(NO_3)_3$ $9H_2O$, $Bi(NO_3)_3$ $5H_2O$,

Gd_2O_3 and $(CH_3COO)_2$ Mn $4H_2O$ with urea as a fuel. The homogeneous gel of these reagents were added stoichiometrically to this fuel and later were dissolved in nitric acid and water. The gel was heated to 400°C for 30 min and then the solvent was evaporated and auto-ignited to result in residues that were crushed later. The extracted material from this reaction was milled for homogeneity. The details of the auto-combustion synthesis process are described elsewhere [1,3,17]. The combustion residue of different concentration were calcinated at different temperatures for 3 h; for x=0.0 at 550°C in air, 0.025≤x≤0.1 at 700°C for x=0.15 and x=0.2 at 750°C. After the calcination, the powder was press to 8 x 10^7Kg/m^2 in cylindrical pellets utilizing polyvinyl alcohol as binder. The samples with concentration of 0.0≤x≤0.1 were sintered at 750°C, while samples with concentration of 0.15≤x≤0.2 were sintered at 780°C, for 6 h. The stoichiometry and phase purity of the samples were studied using X-ray diffraction (XRD) (Philips Analytical-PW3040) at 2°/min from 20°≤2θ≤80° using Cu-K_α radiation (λ=1.5405Å). X-ray line-profile analysis of the samples was used to calculated the crystallite size and lattice strain in the samples using BREADTH software [14]. Micro-Raman spectra of the samples were recorded on backscattering geometry using the 514.5nm Ar-ion laser line using Renishaw micro-Raman spectrometer (model-INVIA). Microstructure, distribution of grain growth, and particle size were studied using field emission scanning electron microscope (SUPRA 35VT SEM) and transmission electron microscope (Techo C230 STwin TEM). For the electrical characterization, the pellets were polished and electroded with silver paint and dried at 150°C for 3 h. Ferroelectric polarization measurements were carried out using Marine PE loop tracer. Dielectric and magnetodielectric measurements were carried out in a wide range of frequency (100 Hz-1 MHz) with the Hioki 3532-50 LCR meter and in-house ME measurement setup. Magnetic

properties were carried out at room temperature using a vibrating sample magnetometer (Lakshore 142AVSM) up to a maximum field of ± 2 T at RT.

3.3 Results and discussion

3.3.1 Structural and microstructural properties

Figure 3.1 shows the XRD pattern of BFO_{1-x}-GMO_x 0.0≤ x≤0.2 solid-solutions. The XRD pattern of the samples was analyzed using the Rietveld refinement using FULLPROF 2.2.4 package [17]. The calculated and difference pattern with Bragg's position of the peaks were given for comparison. The peak shapes were refined using a pseudo-Voigt function and background was corrected using a six-coefficient polynomial function. In order to get a better refinement, zero correction, scale factor, background, unit cell parameters, atomic positions, thermal parameters, and half width parameters (U, V, and W) were varied. The occupancy of all the atomic sites was kept fixed during the refinement process. Rhombohedral crystal structure of undoped $BiFeO_3$ in R3c space group was used for Rietveld refinement. From the refinement analysis, it was found that BFO with up to ≤ 7.5% GMO concentration shows single-phase with R3c space group, whereas above it shows a mixed phase (R3c + $Pn2_{1a}$).

As can be seen from Figure 3.1, a good agreement (goodness of fit χ^2 = 1.15-1.30) has been observed between the observed and the calculated patterns for all the samples. No traces of impurity phases (*i.e.*, $Bi_2Fe_4O_9$ and $Bi_{25}FeO_{39}$) were observed in the samples. The difference between the observed and calculated pattern and the Bragg's positions are given below the observed spectrum (Figure 3.1) for comparison. The lattice constant, space group, and goodness of fit obtained from the Rietveld refinement of BFO_{1-x}-GMO_x 0.0≤ x≤0.2 samples

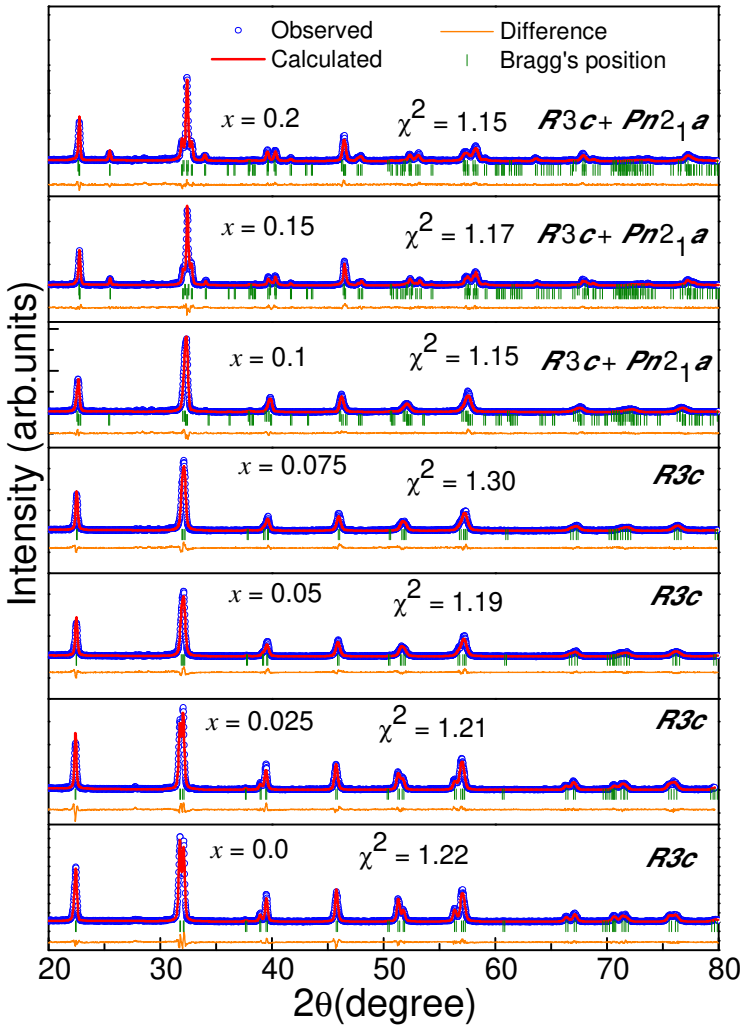

Figure 3.1: XRD pattern of BFO_{1-x}-GMO_x 0.0≤ x≤0.2 solid-solutions. The calculated and difference pattern with Bragg's position of the peaks were given for comparison.

are given in Table 3.1.

The existence of both rhombohedral and orthorhombic structure becomes more prominent with increasing x. For $x = 0.2$, the XRD pattern contains the reflections, which are the characteristics of Pnma/Pbnm space group similar to RE manganite. The polar $Pn2_{1a}$ space group is sub-space group of nonpolar Pnma space group. Therefore, Rietveld refinement was carried out with dual

Table 3.1: Lattice constant, space group, and goodness of fit (χ^2) obtained from the Rietveld refinement of BFO_{1-x}-GMO_x 0.0≤ x≤0.2 samples.

	Space	Lattice Parameters Å			
x	group	a	b	c	χ^2
0.0	R3c	5.5761	5.5761	13.8685	1.22
0.025	R3c	5.5832	5.5832	13.8615	1.21
0.05	R3c	5.5706	5.5706	13.7837	1.19
0.075	R3c	5.5642	5.5642	13.7568	1.30
0.1	R3c+	5.5551	5.55511	13.7113	1.20
	$Pn2_1a$	5.5476	7.78937	5.54864	
0.15	R3c+	5.5571	5.5571	13.4245	1.17
	$Pn2_1a$	5.5866	7.8098	5.45706	
0.2	R3c+	5.5805	5.5805	13.4504	1.15
	$Pn2_1a$	5.6010	7.8093	5.45655	

phase model (R3c + $Pn2_{1a}$). For $x = 0.1$ composition, it is found that around 86% of rhombohedral R3c phase and remaining 14% that of orthorhombic $Pn2_{1a}$ phase. Sample with $x = 0.15$ shows 42% of R3c and 58% of $Pn2_{1a}$ phase, whereas $x = 0.2$, shows 24% of R3c and 76% of $Pn2_{1a}$ phase. The transition from rhombohedral to a mix phase consists of rhombohedral plus orthorhombic phase is expected and can be explained by strong destabilization of R3c structure by Gd^{3+} due to chemical pressure [17].

In order to establish the signature of compositional driven structural phase transition from R3c to R3c+$Pn2_{1a}$, the pseudo-cubic lattice parameter as a function of composition was plotted in Figure 3.2.

Pseudo-cubic lattice parameter is defined as the cube root of the perovskite unit cell volume. It offers a convenient approach because it brings down lattice parameter to the same scale of magnitude for better understanding and is a suitable probe to analyze structural phase transition.

Figure 3.3 shows the average crystallite size of BFO_{1-x}-GMO_x 0.0≤ x≤0.2 samples.

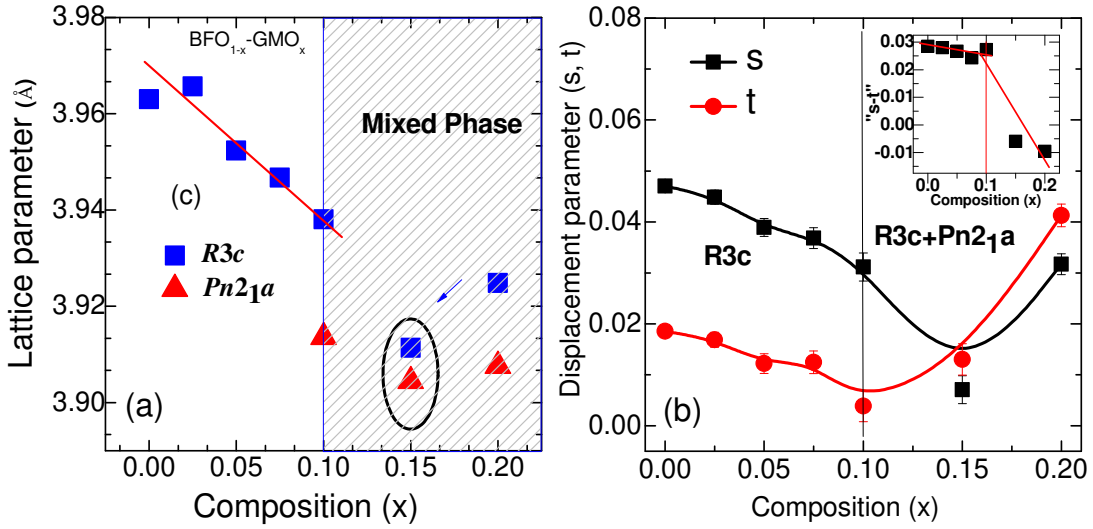

Figure 3.2: (a) Pseudo-cubic lattice parameter as a function of composition of BFO_{1-x}-GMO_x 0.0≤ x≤0.2; (b) Atomic displacement parameters (s, t) as function of composition (Inset- Compositional dependence of "s-t".

The average crystallite size of the samples were calculated using Fourier X-ray line profile analysis (XLPA) based on Double-Voigt method using the program package BREADTH [14]. The average crystallite size of BFO_{1-x}-GMO_x 0.0≤ x≤0.2 solid solutions varies in the range 20 nm to 30 nm. To further support the XLPA analysis, the microstructure of the sample $x = 0.2$ was investigated using high resolution transmission electron microscopy (HRTEM).

Figure 3.4 shows the TEM micrograph (a) and selected area electron diffraction (SAED) pattern (b) of sample $x = 0.2$.

The TEMmicrograph (Figure 3.4a)) shows the average crystallite size of ∼30 nm with some agglomeration, which agrees well with the average crystallite size obtained from XLPA analysis. In order to get the structural insights and the presence of mixed phase, SAED pattern was taken for selected samples. Figure 3.4(b) shows the SAED patterns of sample $x = 0.2$. The presence of set of ring diffraction patterns and absence of spotty diffraction patterns clearly

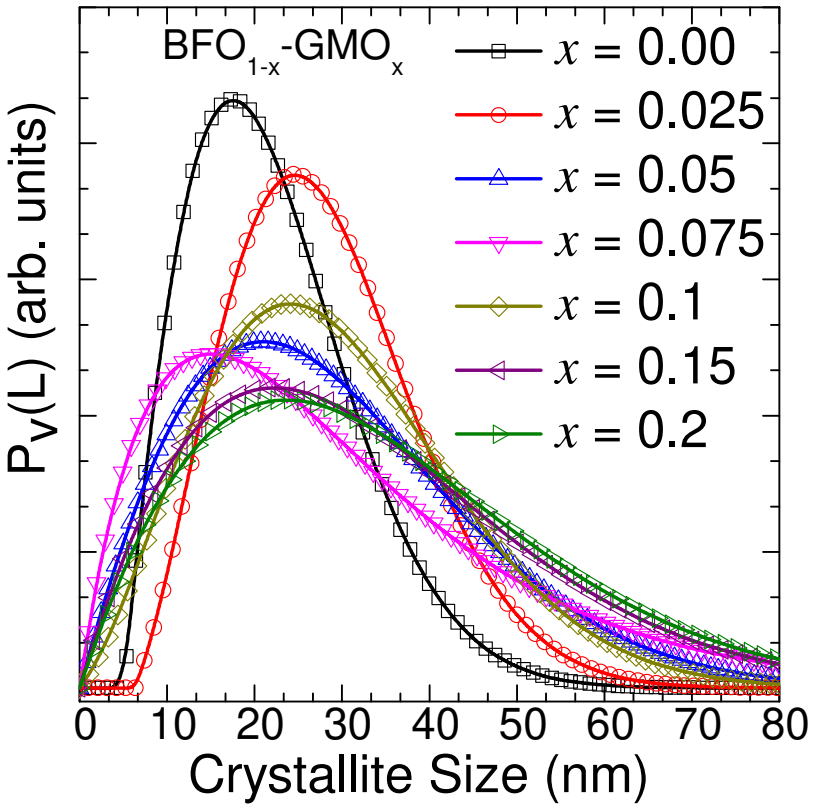

Figure 3.3: Average crystallite size of BFO_{1-x}-GMO_x 0.0≤ x≤0.2.

show the polycrystalline nature of the sample. The indexing of diffraction pattern (Figure 3.4(b)) clearly shows the presence of mixed phases. This observation is in agreement with the XRD Rietveld refinement finding of the presence of the mixed R3c+$Pn2_{1a}$ phase in x=0.2 sample.

For better the understanding of microstructure, the fractured surface of the samples were analyzed with scanning electron microscope (SEM). Figure 3.5 shows the scanning electron micrographs of selected BFO_{1-x}-GMO_x samples (x = 0.0, 0.05, 0.1, and 0.2).

As can be seen from the SEM micrographs, the samples show densely distributed grains with well defined grain boundary without defects and voids. Pure

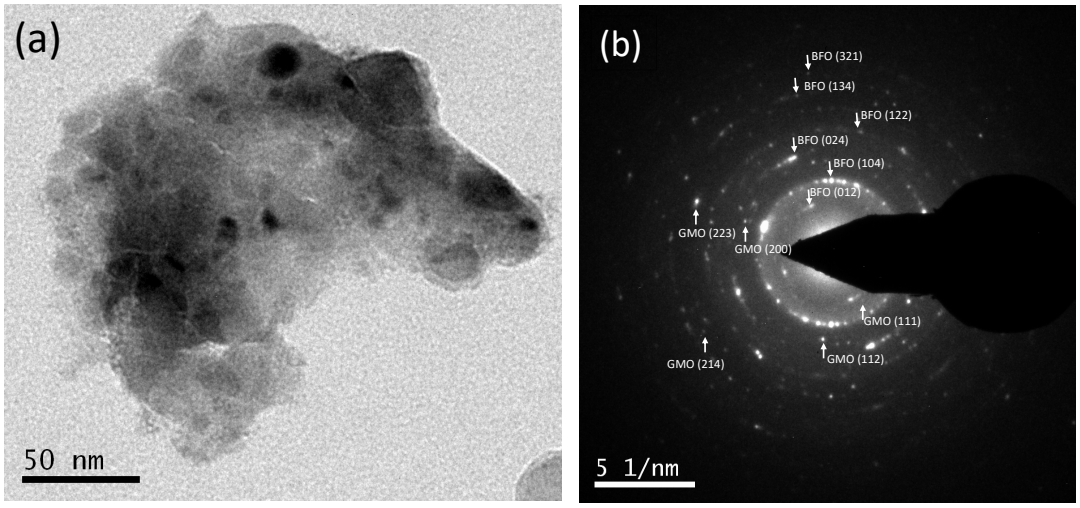

Figure 3.4: Transmission electron microscopy (TEM) of BFO_{1-x}-GMO_x x= 2.0: (a) TEM image showing nanoparticles of average size of 25 nm; (b) the selected area electron diffraction (SAED) pattern showing polycrystalline nature and mixed phase of the sample.

BFO (Figure 3.5a)) shows highly non-uniform grain size distribution ranging from 200 nm-2 μm, whereas samples with x = 0.05, 0.1, and 0.2 (Figure 3.5b)-d)) show distribution of uniform grain size of average 200 nm. A decreasing in grain size was observed in solid solutions with increasing GMO concentration. This observation is not yet well understood, however, it can be attributed to the reduction of electrical resistivity due to the incorporation of rare-earth oxide (GMO) phases into the semiconducting BFO phase which facilitate an enhanced diffusion process and decreasing gain size. The reduction in electrical resistivity by 10 orders of magnitude has been reported in $BaTiO_3$ with rare-earth oxide incorporation [19].

3.3.2 Raman spectroscopy

In order to get the structural insight of the composition driven phase transition and changes in phonon response, micro-Raman spectra were recorded in

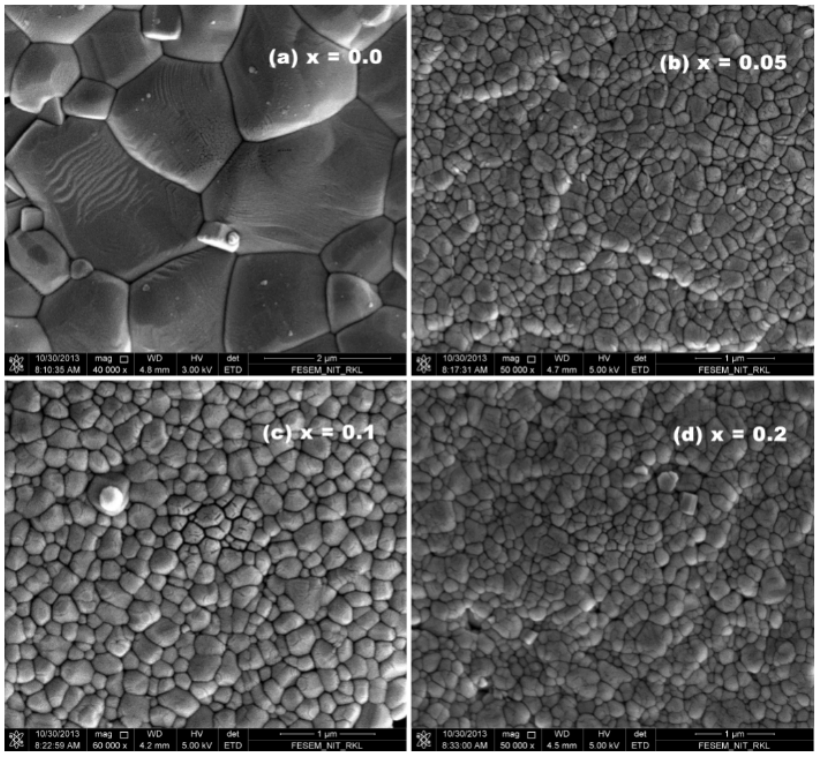

Figure 3.5: SEM micrographs of BFO_{1-x}-GMO_x solid solutions: (a) x= 0.0; (b) x= 0.05; (c) x= 0.1, and (d) x= 0.2.

backscattering geometry using Ar ion laser (λ = 514.5 nm).

Figure 3.6 shows the comparison of Raman spectra of BFO_{1-x}-GMO_x 0.0≤ x≤0.2 samples at RT.

According to the group theory selection rules, the rhombohedral structure of BFO with R3c (C_{3v}) symmetry will give rise to $4A_1$+ 9E Raman active modes [5, 6]. The peaks at low temperature (81 K) in single domain single crystal observed at around 75, 265, 350, and 523 cm^{-1} are assigned as A_1 modes, whereas peaks at around 79, 145, 175, 224, 277, 295, 371, 473, and 553 cm^{-1} are assigned as E modes [6]. Of these 13 single phonon modes of BFO, we observed only eight Raman active modes in BFO_{1-x}-GMO_x 0.0≤ x≤0.2 samples at RT. Some modes are not seen due to thermal broadening effect at RT. As can be seen

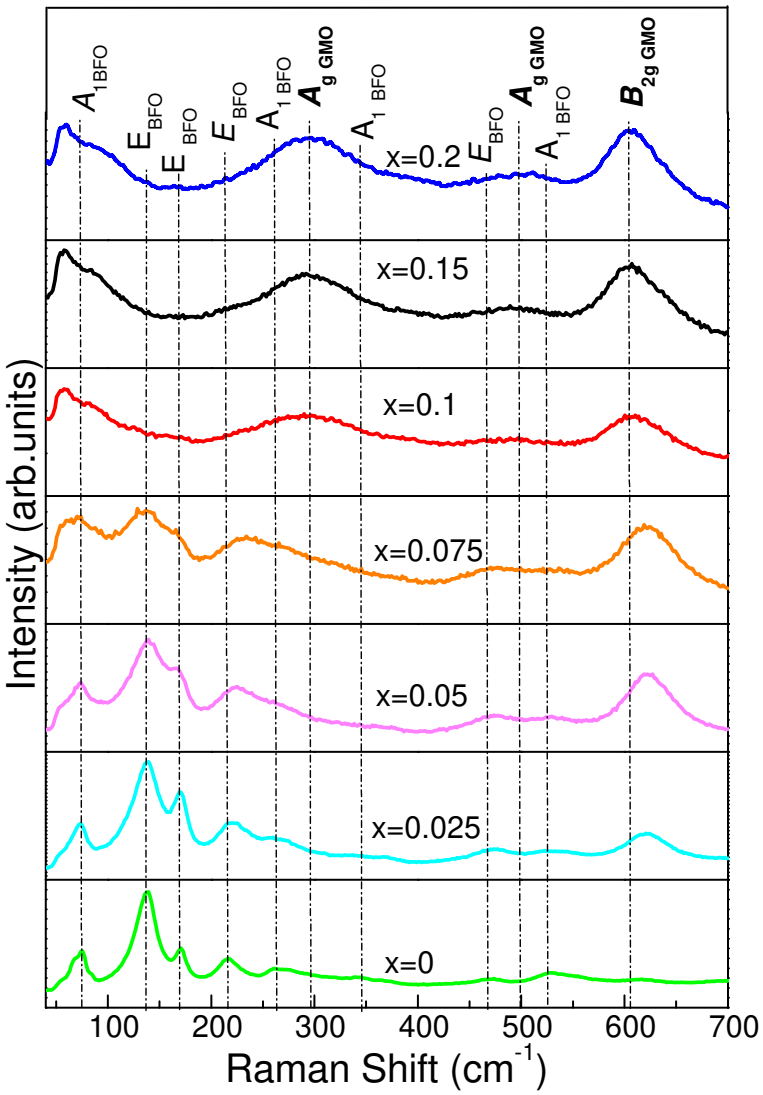

Figure 3.6: Raman spectra of BFO_{1-x}-GMO_x 0.0≤ x≤0.2 solid-solutions. The vertical dotted lines in the figure are a guide to the eye.

from the Figure 3.6, the A_1 modes are observed at around 75, 262, 344, and 530 cm^{-1}, whereas, four E modes are seen at around 139, 171, 370 and 470 cm^{-1} in agreement with BFO single crystal Raman spectra [5, 6].

As GMO concentration increases, we observed some suppression of BFO phonon modes and appearance of three new phonon modes at around 293, 497, and 620 cm^{-1} associated with GMO. The peak at 620 cm^{-1} (B_{2g} (1) mode)

appears from x =0.025 is associated with the in-plane O_2 stretching and called as breathing mode. This mode is shifting to higher frequency with increasing GMO concentration. The mode at 293 cm^{-1} (A_g (2) mode) appears from the sample x =0.1 is related to the in-phase rotation (y-axis) of MnO_6 octahedra and O_2 motion along x-axis. The mode at around 497 cm^{-1} (A_g (3) mode) appears in samples $x \geq 0.15$ corresponds to bending of MnO_6 octahedra and O_2 anti-stretching [20]. As can be seen from Figure 3.6, it is quite evident that BFO_{1-x}-GMO_x up to $x = 0.075$ show phonon features dominated by BFO phase, while samples with higher concentration of GMO ($x \geq 0.1$) show phonon anomalies indicating the existence of mixed structural phase. The observation of mixed phase at higher concentration of x agrees well with the XRD and TEM (SAED) studies.

3.3.3 Dielectric properties

In order to understand the dielectric behavior, the dielectric permittivity (ε), dielectric loss (tan δ), conductivity (σ_{ac}), and phase angle (θ) were measured as a function of frequency and temperature.

Figure 3.7(a) shows the frequency variation of dielectric permittivity. The observation of decrease in permittivity with increasing frequency is the typical behavior of ferroelectrics. The high dielectric permittivity observed at low frequency can be explained by the presence of a potential barrier probably due to the existence of space charge polarization at the grain boundaries. This can lead to the accumulation of charges at the grain boundary, which leads to the high value of dielectric permittivity [21–23]. The decrease in dielectric permittivity with increasing frequency can be attributed to the reduction of space charge polarization [23]. The change in dielectric dispersion behavior (non-exponential)

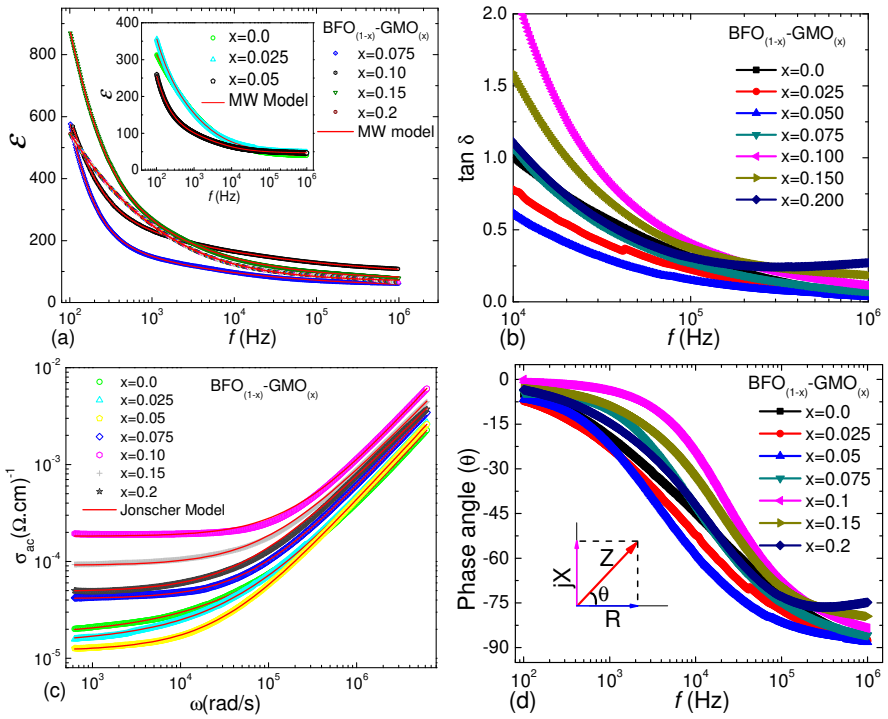

Figure 3.7: Dielectric properties of BFO_{1-x}-GMO_x 0.0≤ x≤0.2 as a function of frequency at RT: (a) Dielectric permittivity (ε); (b) Dielectric loss (tan δ); (c) ac conductivity (σ_{ac}); (d) phase angle (θ), the angle between the real part (Resistance, R) and imaginary part (Reactance, X) of impedance (cf. inset). The *solid-line* in (a) and (c) shows the Maxwell-Wagner (MW) model and Jonscher Model fit to the data, respectively.

with increasing polar phase ($Pn2_{1a}$) upon GMO substitution can be attributed to the presence of morphotropic phase boundary (MPB). No significant change is observed on the values and nature of dielectric dispersion at higher frequencies. However, at low frequency (< 1 kHz) an increase in dielectric permittivity was observed with increasing GMO concentration. This can be explained by the change in conductivity or dipole relaxation phenomena [19].

To understand the nature of dielectric relaxation process, the dielectric dispersion behavior was analyzed with various dielectric relaxation models. As can be seen, the data fits very well with the modified Maxwell-Wagner (MW) relax-

ation model, as described in Equation 3.1 [24–26]:

$$\epsilon'(f) = \epsilon_\infty + \frac{1}{2}(\epsilon_s - \epsilon_\infty)b + Af^{-n} \tag{3.1}$$

and

$$b = 1 - \frac{sinh[(1-\alpha)ln(2\pi f\tau)]}{cosh[(1-\alpha)ln(2\pi f\tau + sin(\frac{1}{2}\alpha\pi))]}$$

Table 3.2: Fitting parameters obtained from Maxwell-Wagner model for BFO_{1-x}-GMO_x 0.0≤ x≤0.2 at RT for dielectric permittivity at lower frequencies (ϵ_s) dielectric constant at higher frequencies (ϵ_∞), polydispersity (α), dispersion parameter of frequency (n), and the relaxation time (τ).

x	ϵ_s	ϵ_∞	α	n	τ(ms)
0.0	220	37	0.43	0.59	0.19
0.025	142	45	0.45	0.55	0.24
0.05	144	42	0.57	1.0	0.29
0.075	185	35	0.81	1.0	0.39
0.1	396	41	0.82	1.0	0.72
0.15	461	67	0.63	0.98	0.73
0.2	688	67	0.48	1.0	0.75

where ϵ_s is the dielectric permittivity at the lowest frequency, ϵ_∞ is the dielectric permittivity at the highest frequency, α is the measure of the polydispersity of the system, τ is the total relaxation time, and n is the dispersion parameter of frequency [32, 33]. The main consideration of the MW effect is the charge accumulation at the interface and their different charge carrier relaxation times [24]. The MW effect is commonly observed in two-material interface, such as metal-insulator, metal-semiconductor, insulator-semiconductor, semiconductor-semiconductor, *etc* [24, 32, 33]. The ratio of dielectric constant to conductivity is the relaxation time associated with the spreading of the ex-

cess free carriers in the materials [24]. The *solid line* in Figure 3.7a shows fits of the modified Maxwell-Wagner relaxation model with the experimentally observed data. The values of ϵ_s, ϵ_∞, α, n, and τ obtained from the MW-model for BFO_{1-x}-GMO_x ($0.0 \leq x \leq 0.2$) solid solutions at RT are given in Table 3.2. As can be seen, the relaxation time increases with increasing x. A significant increase in relaxation time was observed for samples with $x \geq 1$, which can be associated with the increase of polar phase and MPB.

Figure 3.7(b) shows the frequency variation of dielectric loss of BFO-GMO solid solutions. As can be seen, samples with $x \leq 0.05$ show low dissipation compared to BFO in the measured frequency range. The sample with $x = 0.075$ shows low loss at higher frequencies compared to BFO. Samples with $x \geq 0.1$ show no improvement in dielectric dissipation at lower frequencies, but shows slightly higher loss at higher frequencies.

The ac conductivity (σ_{ac}) of the BFO_{1-x}-GMO_x samples obtained from the dielectric measurements using the formula [29, 30] $\sigma = \sigma_0 \omega \epsilon_0 \epsilon \tan \delta$, where σ_0 is the frequency independent conductivity, ω is angular frequency, ϵ_0 is vacuum dielectric permittivity, is shown in Figure 3.7(c). Generally, σ_{ac} of dielectrics increases with increasing both the frequency and the temperature. The frequency variation of ac conductivity was analyzed by universal power law proposed by Jonscher [28]: $\sigma_{ac} = A\omega^n$. This power law is related to the dynamics of the ionic hopping transport between localized sites. The exponent n is the measure of the degree of interaction with the materials conduction environment. The exponent in the range of 0.6 - 1.0 indicates disordered or amorphous systems and the conduction mechanism is mostly associated with diffusion limited hopping. Exponent $n \approx 1$ implies ideal long-range (band-to-band) conduction process, which is normally observed at low temperature, whereas $n > 1$ indicates the presence

of thermally activated hopping process between two sites separated by energy barrier [29]. It also could be due to the presence of two dispersion processes with different relaxation times [32–35]. As can be seen, the ac conductivity σ_{ac} shows an excellent fit (solid line) to the modified Jonscher model, as defined in Equation 3.2 [28, 29]:

$$\sigma_{ac}(\omega) = \sigma_0 + A_1\omega^{n_1} + A_2\omega^{n_2}, \qquad (3.2)$$

Table 3.3: Fitting parameters obtained from the modified Jonscher power law model for BFO_{1-x}-GMO_x ($0.0 \leq x \leq 0.2$) solid solutions at RT.

x	σ_{dc}x10^{-5} $(\Omega$ cm$)^{-1}$	A_1x10^{-9}	A_2x10^{-10}	n_1	n_2
0.0	1.69	131	1.15	0.48	1.06
0.025	1.38	152	3.07	0.42	1.02
0.05	1.11	342	5.19	0.18	0.98
0.075	4.13	0.21	6.65	0.97	0.97
0.1	1.83	0.52	4.66	0.99	0.99
0.15	9.12	1.05	10.5	0.93	0.93
0.2	4.89	1.46	14.7	0.90	0.90

where σ_0 is the frequency independent conductivity (dc conductivity), A_1 and A_2 are the coefficients, and n_1 and n_2 are critical exponents. The universal power law was modified with hopping relaxation model and conduction through grain boundaries. The first exponent is associated with the charge carriers motion due to dc conduction and dispersive ac response. The frequency at which slope changes is known as hopping frequency of the polarons (ω_p) and is temperature dependent. The plateau region corresponds to the frequency-independent

dc conductivity. The rise in the conductivity value with frequency indicates a normal ferroelectric behavior [36]. The conduction parameters and critical exponents obtained from the fitting are given in Table 3.3.

As can be seen, n_1 varies from 0.48 to 0.90 and n_2 varies from 0.90 to 1.06 indicating presence disordered phase and hopping type conduction process. The different n could be indicative of the charge carriers might have translational motion with a sudden hopping and localized hopping [29].

Figure 3.7(d) shows the frequency variation of phase angle (θ), the angle between the real (resistance, R) and imaginary part (reactance, X) of impedance $Z = R + jX$), of BFO-GMO samples. All the samples show a resistivity behavior at low frequency and gradually changes to highly capacitive nature at higher frequencies, which is consistent with the observation of very low dielectric dissipation at high frequency.

Figure 3.8 shows the temperature variation of dielectric permittivity (ϵ_r) and loss ($\tan\delta$) of BFO_{1-x}-GMO_x 0.0$\leq$ x$\leq$0.2 at f=1 MHz.

The dielectric permittivity (Figure 3.8(a)) pure BFO shows an anomaly at around the Neel temperature (T_N = 360°C). Samples with x = 0.025 and 0.05 show behavior similar to BFO showing a very weak anomaly near magnetic transition temperature. However, samples with higher concentration of GMO (x $\geq$ 0.1) show the shifting of anomaly towards lower temperature. Samples with x = 0.075, 0.10, 0.15, and 0.2 show anomaly at around 345, 275, 206, and 212°C, respectively. The observation of the shifting of the anomaly implies the shifting of the magnetic phase transition of the BFO towards the lower temperature. The dielectric loss (Figure 3.8(b)) as a function of temperature shows similar anomaly with increasing x. For pure BFO, the loss was almost constant up to T_N and above T_N it shows very slow increase. As the concentration of x increased in the

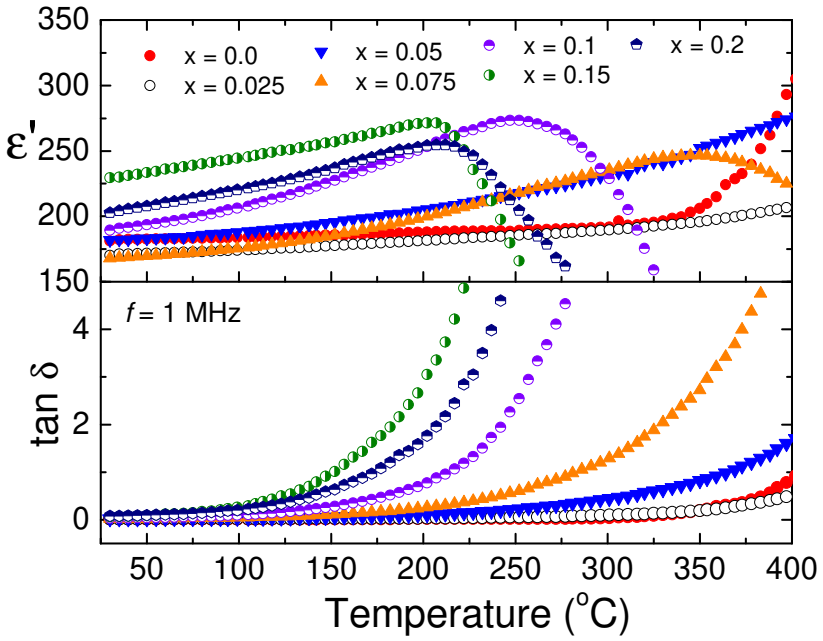

Figure 3.8: Temperature variation of dielectric permittivity (a) and loss (b) of BFO_{1-x}-GMO_x $0.0 \leq x \leq 0.2$ solid-solutions.

solid solution the anomaly of dielectric loss shifted towards lower temperature with faster rate. The observed behavior of dielectric permittivity and loss in BFO is consistent with the reported results [38].

3.3.4 Ferroelectric properties

Figure 3.9 shows the ferroelectric polarization of some unpolled BFO_{1-x}-GMO_x (x =0.0, 0.025, and 0.05) samples at RT.

The absence of saturation of polarization implies the lossy ferroelectric behavior. Decreasing in remanence and coercivity was found with in increasing GMO concentration. Samples with higher concentration of x (> 0.05) show very similar PE loop as sample $x = 0.05$. The observed polarization is very low compared to the values obtained in single crystal and thin film, but it agrees well with the polycrystalline samples [38]. The polarization in BFO is associated with

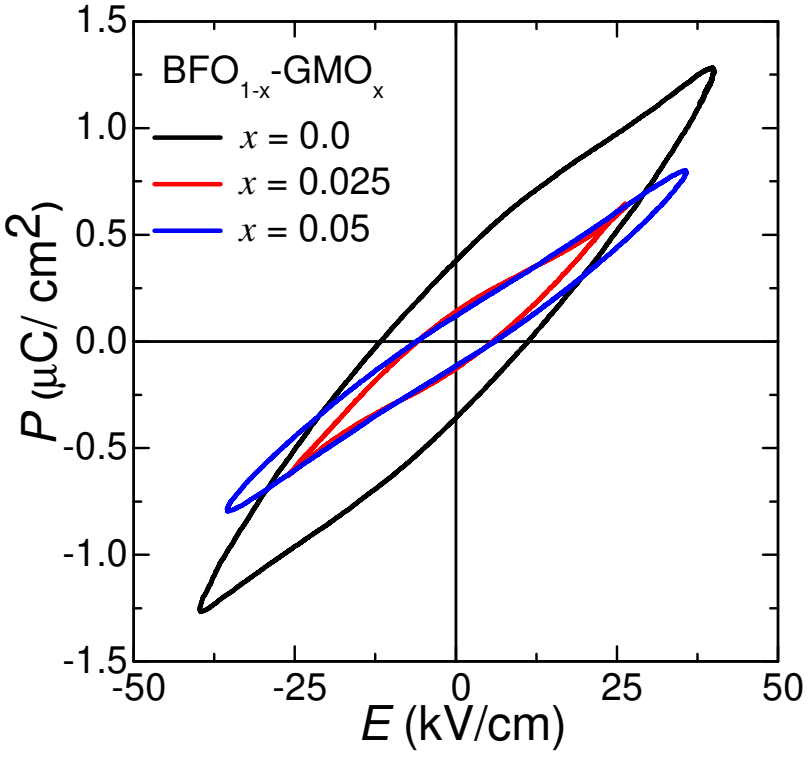

Figure 3.9: Ferroelectric polarization of BFO_{1-x}-GMO_x (x =0.0, 0.025, and 0.05) solid solutions.

the Bi 6s lone pair electrons. However, the high polarization observed in thin films is attributed to the large strain-induced Fe-ion displacement relative to the oxygen octahedra in addition to the contribution of Bi 6s lone pair electrons [39]. The polarization in BFO is also highly dependent on structural phase [39]. The observation of suppression of polarization is attributed to the domain wall pinning [40]. BFO has very complex domain structures (twin 71°, twin 109°, and twin 180°domain walls) [40]. In polycrystalline samples, disorders play a significant role in suppressing polarization. Polycrystalline samples could not sustain the high electric field required for switching the magnetization to study the magnetoelectric effect. So, we focused our magnetoelectric (ME) coupling studies through magnetodielectric effect.

3.3.5 Magnetic properties

Figure 3.10 shows the magnetic hysteresis loop of BFO_{1-x}-GMO_x ($0.0 \leq x \leq 0.2$) solid solutions at RT (25°C) and 2 K (-271.15°C). As can be seen from the RT hysteresis loop (Figure 3.10(a)), pristine BFO and BFO with 2.5% GMO shows no hysteresis loop even up to field of 2 T.

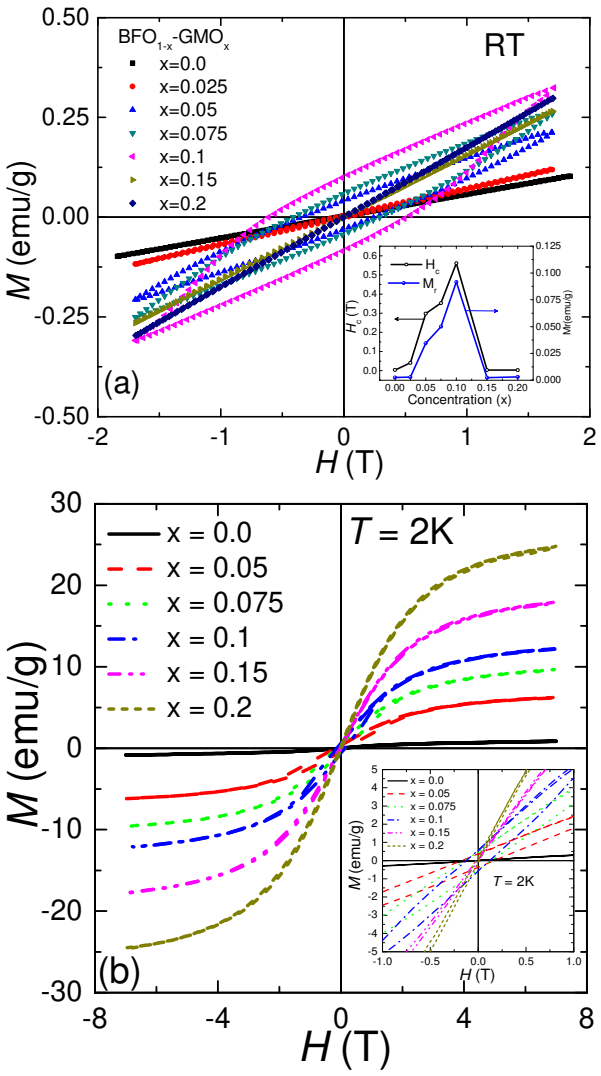

Figure 3.10: MH loop of BFO_{1-x}-GMO_x ($0.0 \leq x \leq 0.2$) solid solutions: (a) room temperature (300 K); (b) 2 K.

This observation is in agreement with the nature BFO magnetic order-

ing [1, 2]. The magnetic nature of BFO is associated with the canted G-type antiferromagnetic ordering with spiral spin modulation of 60 nm [41], due to the combined effect of exchange interaction and spin-orbit coupling. In the case of GMO, the ferromagnetically ordered Gd (T_c = 19.85°C)) spins significantly contribute to the net magnetic moment compared to the antiferromagnetically canted state of Mn (T_N= -173.15°C) spins [6]. The solid solutions with higher concentration of x show ferromagnetic-like hysteresis loop at RT. This could be due to the change in magnetic ordering in BFO from the cycloidal spiral spin structure to a ferromagnetic ordering with increasing GMO concentration. Relatively high value of remanent magnetization and coercivity was observed in BFO with 10% GMO compared to other samples. The inset in Figure 3.10(a) shows the variation of coercivity (H_c) and remanent (M_r) magnetization as the function of x at RT.

Figure 3.10(b) shows the MH loop at 2 K (-271.15°C). As can be seen, no magnetic hysteresis is observed for pure BFO, which is consistent with its intrinsic magnetic ordering. We observed higher magnetization and saturation at 2 K in other samples and the trend is somewhat commensurate with the RT observation that the sample x =0.1 shows higher coercivity compared to other samples. The improved magnetization and coercivity observed in samples with $x \leq 1.0$ can be attributed to the synthesis of nano-crystalline solid solutions of BFO-GMO which might have introduced strain leading to the suppression of spin cycloid modulation of BFO and appearance of uncompensated spins [41–43]. The following possibilities might be responsible for the observed effect: (i) substitution of Gd^{3+} at Bi-site might have facilitated to collapse of space modulated spin structure; (ii) substitution of magnetically active Mn^{3+} at Fe-site of BFO favors ferromagnetic interaction. It is well known that the magnetic properties

can be affected significantly by the nearest and next nearest neighbor exchange interactions. The samples with higher doping concentration GMO concentration ($x \geq 0.15$) shows reduction in coercivity and remanence, which can be explained by the change in neighboring magnetic ions ordering from ferromagnetic to an antiferromagnetic (substitution of ferromagnetic spins of Fe by antiferromagnetic spin of Mn). This can reduce the exchange interactions resulting in lower magnetization.

In order to understand the nature of magnetic ordering and magnetization dynamics, temperature variation of field cooled (FC) and zero field cooled (ZFC) magnetization was carried out from RT down to 2 K (-271.15°C) as shown in Figure 3.11.

As can be seen, the FC and ZFC magnetization show very similar behavior indicating the absence of secondary magnetic phase and magnetic frustrations [44]. The sharp increase of magnetization at low temperature could be related to the presence of paramagnetic cluster or phase [45, 46]. Since the $4f$ electrons of the rare-earth (Gd^{3+}) are very localized, the direct exchange is not a dominating mechanism for the magnetic properties [45, 46]. According to the Goodenough-Kanamori-Anderson (GKA) rules [47–50], the strong superexchange interaction between Mn^{3+} and Mn^{4+} through oxygen (O^{-2}) anion (magnetic ion-ligand-magnetic ion are in 180°) results in antiferromagnetic ordering, whereas, a 90° superexchange interaction between Mn^{3+}/ Mn^{3+} and Mn^{3+}/ Mn^{4+} through vacancies could result in weaker ferromagnetic ordering. The antiferromagnetic coupling between Mn atoms is energetically favored [50]. The observation of ferromagnetic-like behavior and non-saturation of magnetization at low temperature in BFO-GMO solid solution samples could be due to the presence of both the types of superexchanges.

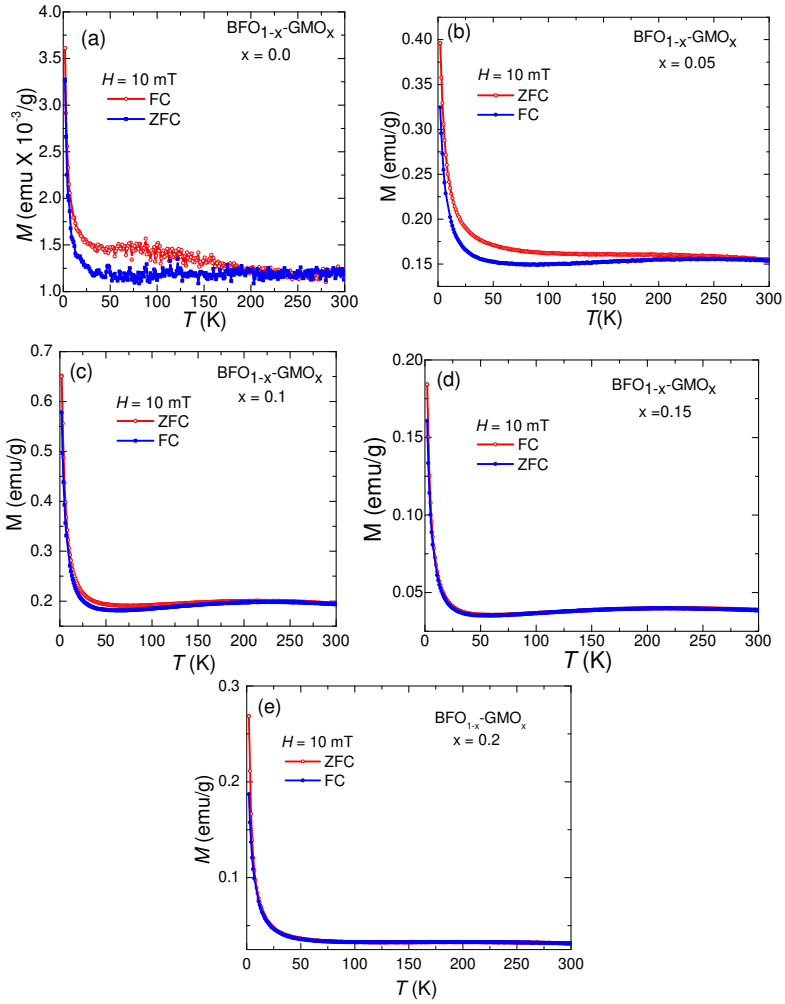

Figure 3.11: Temperature variation of ZFC and FC magnetization of loop of BFO_{1-x}-GMO_x:(a) x = 0.0; (b) x = 0.05; (c) x = 0.10; (d) x = 0.15; (e) x = 0.20.

3.3.6 Magnetodielectric properties

3.3.6.1 Impedance and Modulus spectroscopy

The dynamical features of dielectrics and ferroelectrics are accompanied by the motion of charges, *e.g.* orientation polarization of dipoles and/or the motion of ions. Impedance (Z) and modulus (M) spectroscopy are powerful methods of characterizing the electrical properties of materials and their interface with electrodes. The impedance spectroscopy (IS) allows the separation of resistances

related to grains, grain boundaries, and electrode effects because of their different relaxation times that results in a separate semicircles in impedance spectra [26]. These techniques can also be used to study the dynamics of bound or mobile charge in the bulk or interfacial regions of solids and provide a better insight for understanding the relationship between electrical transport and microstructure in nanocrystalline samples.

In order to understand the dielectric relaxation, *e.g.* long-range conductivity (non-localized) and dipolar (localized) relaxation, we carried impedance spectroscopy of multiferroic solid solutions with and without magnetic field (H).

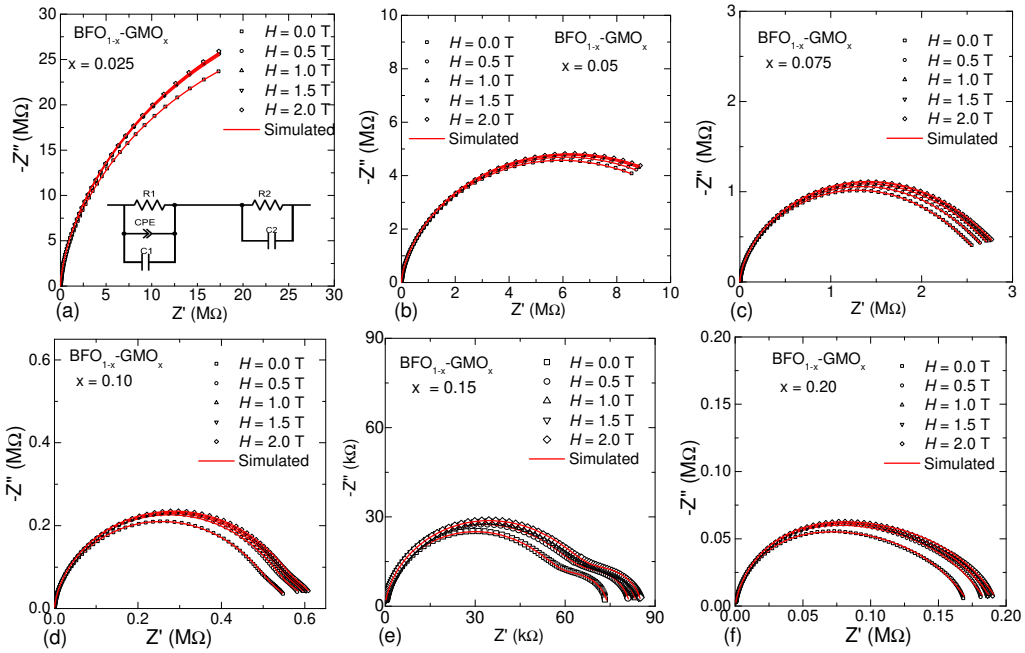

Figure 3.12: Nyquist plot of BFO_{1-x}-GMO_x with different percentage of x; (a) x = 0.025; (b) x = 0.05; (c) x = 0.075;(d) x = 0.01;(e) x = 0.15; (f) x = 0.2. The inset in (a) shows the equivalent circuit consisting of grain and grain boundary effect that was used to simulate the observed data.

Figure 3.12 shows the Nyquist plot of real (Z') and imaginary (Z'') part of the impedance of BFO_{1-x}-GMO_x ($0.025 \leq x \leq 0.2$) solid solutions as a function of magnetic field at RT. As can be seen, the sample with x= 0.025 (Figure 3.12(a))

shows a non-linear behavior, but not semicircular, suggesting an insulating nature. The undoped BFO (not shown) shows very similar behavior as in the case BFO with 2.5% of GMO. The semicircular behavior gradually develops with increasing concentration of x. For $x = 0.05$, a semicircular arc starts forming and became prominent with increasing composition up to x = 0.075. Samples with composition x $\geq$0.1, exhibit the presence of two overlapping semicircular arcs with their centers below the real axis. The high frequency semicircle is attributed to the bulk (grain) property of the material, whereas the low frequency semicircular arc observed at intermediate frequency is attributed to the grain boundary effect. The intercept of the semicircular arcs on the real axis gives rise to grain and grain boundary resistance of the materials. The absence third semicircle rules out the presence of electrode-sample interface effect. As can be seen, all the samples show suppression in resistance with increasing magnetic field.

For quantitative understanding of the impedance behavior and the effect of grain and grain boundary contributions, the data were simulated with the equivalent circuit using a *brick-layer model* for a polycrystalline material [26]. The high frequency semicircular arc was modeled to an equivalent circuit shown in inset Figure 3.12(a). The equivalent circuit contains parallel combination of a bulk resistance (R_1), bulk capacitance (C_1) along with a constant phase element (CPE) [26], whereas the low frequency semicircular arc was modeled for parallel combination of grain boundary resistance (R_2) and grain boundary capacitance (C_2). The CPE admittance is $Y(CPE) = A_0 (j\omega)^n = A\omega^n + jB\omega^n$ [26], where $A = A_0 cos(n\pi/2)$ and $B = A_0 Sin(n\pi/2)$. A_0 and n are frequency independent parameters usually depend on temperature, A_0 determines the magnitude of the dispersion and the n value is 0$\leq$ n $\leq$ 1 [17]. The CPE describes an ideal capacitor

for n=1 and an ideal resistor for n=0 [51–53]. Both the equivalent circuits are connected in series for fitting the impedance data. The *solid line* in Figure 3.12 shows simulated fit of equivalent circuit to the data using an electrochemical impedance spectroscopy (EIS) data analysis software (ZSimpWin) [54]. As can be seen, a good agreement has been found with the equivalent circuit simulated data with the observed data. Tables 3.4 and 3.5 list the bulk capacitance and resistance, respectively, obtained from the Nyquist fittings using the equivalent circuits (Inset Figure 3.12(a)) for BFO_{1-x}-GMO_x ($0.0 \leq x \leq 0.2$) solid solutions. It is observed that for all the compositions the bulk capacitance decreases with increasing magnetic field, while bulk resistance increases, which indicates the presence of magnetoelectric coupling in BFO-GMO solid solutions.

Table 3.4: Bulk capacitance obtained from fitting of magnetic field dependent complex impedance plot of BFO_{1-x}-GMO_x($0.0 \leq x \leq 0.2$) at RT.

Bulk Capacitance (10^{-11}F)							
H(T)	x=0.0	x=0.025	x=0.05	x=0.075	x=0.1	x=0.15	x=0.2
0.0	4.174	2.783	3.578	3.258	3.544	6.305	5.788
0.5	4.145	2.734	3.320	3.188	3.490	6.286	——
1.0	4.152	2.733	3.319	3.187	3.400	6.193	5.562
1.5	4.152	2.734	3.320	3.186	3.380	6.184	5.559
2.0	4.152	2.732	3.316	3.178	3.400	6.188	5.545

Table 3.5: Bulk resistance obtained from fitting of magnetic field dependent complex impedance plot of BFO_{1-x}-GMO_x($0.0 \leq x \leq 0.2$) at RT.

Bulk Resistance (Ω)							
H(T)	x=0.0 10^6	x=0.025 10^7	x=0.05 10^7	x=0.075 10^6	x=0.1 10^5	x=0.15 10^4	x=0.2 10^5
0.0	8.6176	8.238	1.226	2.522	5.415	6.240	1.307
0.5	9.3114	8.812	1.358	2.671	5.761	6.841	1.394
1.0	13.469	8.897	1.379	2.749	5.834	7.021	1.428
1.5	14.609	8.978	1.387	2.792	5.892	7.106	1.446
2.0	15.589	9.007	1.395	2.819	5.965	7.159	1.459

For the better understanding of the relaxation process and dominating

charge transport mechanisms, the dispersion of imaginary part of impedance (Z'') and modulus (M'') of BFO_{1-x}-GMO_x ($0.025 \leq x \leq 0.2$) were measured and compared at a constant magnetic field (2 T) as shown in Figure 3.13.

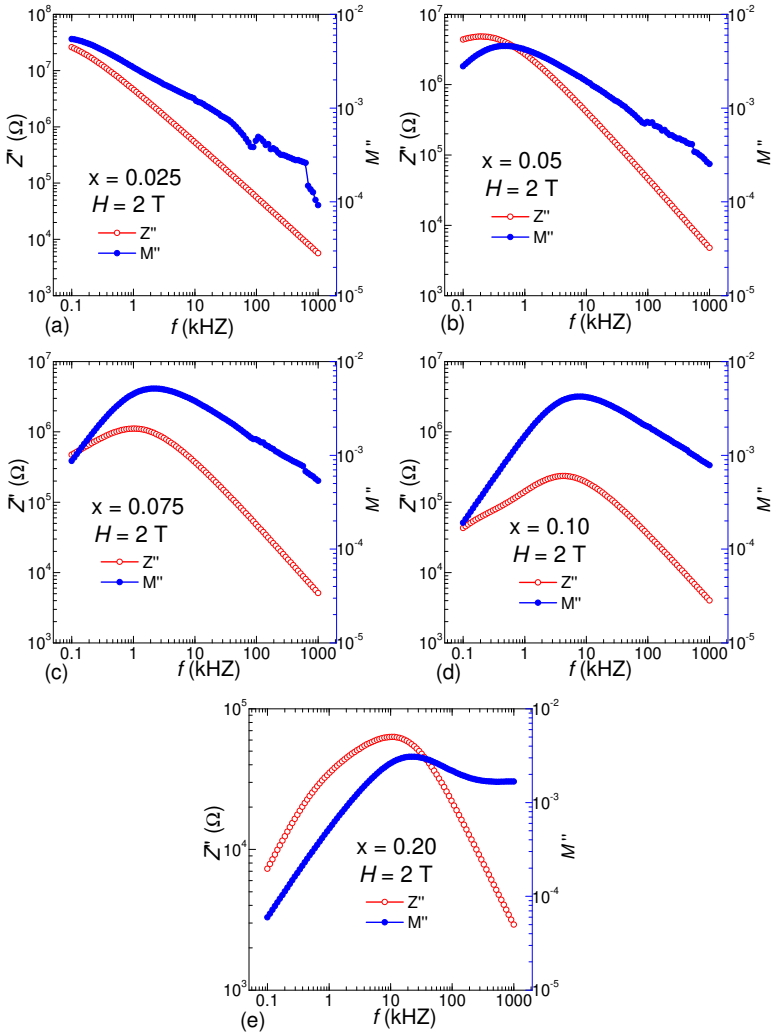

Figure 3.13: Frequency dependent Z" and M" of BFO_{1-x}-GMO_x with different percentage of x; (a) x = 0.0; (b) x = 0.025; (c) x = 0.05;(d) x = 0.075;(e) x = 0.10.

As can be seen, no relaxation peak (maxima) was observed for $x = 0.025$ (Figure 3.13(a)), while samples with $x \geq 0.05$ (Figure 3.13(b-e)) shows dielectric relaxation in both impedance and modulus. It was found that the relaxation

time ($\tau = 1/2\pi f_{max}$, where f_{max} is the frequency corresponds to peak maximum of (Z'') and (M'') decreases with increasing composition (x). The presence of dielectric relaxation peaks in impedance and modulus at different frequency implies non-Debye relation process which is dominated by the short-range hopping of charge carriers. In the case of long-range Debye type relaxation process the relaxation peak of impedance and modulus should appear at the same frequency [55–57]. Inserting a constant phase element (CPE) in the equivalent circuit modeled the observed impedance behavior very well.

3.3.6.2 Magnetocapacitance and magnetoimpedance measurement

In order to understand the magnetodielectric (MD) coupling, magnetocapacitance (MC) and magnetoimpedance (MI) of the BFO-GMO solid solutions were measured at RT. It has been predicted that an intrinsic magnetoresistance (MR) could enhance the MD effect from inhomogeneities. In ceramics the MR is dominated by the spin-polarized tunneling across the grain boundary. Maxwell-Wagner effect combined with MR could be the mechanism for magnetocapacitance without magnetoelectric coupling [58, 59]. To rule out the MR related MD coupling effect, we carry out frequency dependent MC and MI at RT.

The change in MC was measured with and without magnetic field as: MC(H) = [C(H)-C(0)]/C(0), where C(H) is the capacitance at the magnetic field H and C(0) is the capacitance at the zero magnetic field. Figure 3.14 shows the MC of BFO_{1-x}-GMO_x ($0.0 \leq x \leq 0.1$) solid solutions at 100 Hz and 1 kHz in forward and reverse magnetic field (0-2 T) sweeps.

Our study was focused on the compositions away from the MPB. As can be seen, the undoped BFO (Figure 3.14(a)) shows very weak MC change and magnetic hysteresis, which agrees with its intrinsic magnetic ordering of BFO.

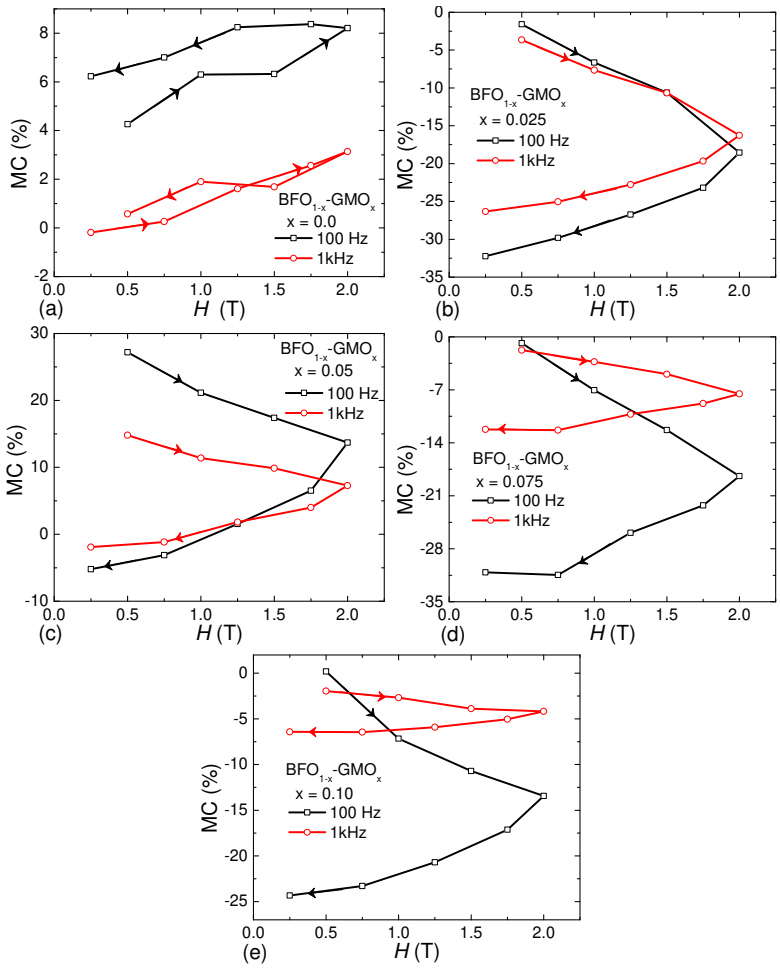

Figure 3.14: Magnetocapacitance (MC) of BFO_{1-x}-GMO_x with different percentage of x; (a) x = 0.0; (b) x = 0.025; (c) x = 0.05; (d) x = 0.075; (e) x = 0.10.

Samples with x= 0.025, 0.05, 0.075, and 0.10 (Figure 3.14(b-e)) shows about 20-25% MC and 25-30% magnetic hysteresis at 2 T and 100 Hz. A strong magnetodielectric (MD) effect could be useful for device applications. All the samples show reduced MC and hysteretic behavior at 1 kHz. The observed negative MC in samples with x= 0.025, 0.075, and 0.10 in forward and reverse field sweeps indicates the presence of antiferromagnetic dominated magnetic ordering at RT. The sample with x= 0.05 (Figure 3.14(c)) shows both the positive and negative MC change indicating the presence of both the ferromagnetic and antiferromagnetic

orderings, which can be explained by the competing interaction between the ferromagnetically ordered Gd spins with the antiferromagnetically canted Mn spins. The observation of magnetic hysteresis shows the presence of long-range ordered magnetic states. BFO-GMO solid solutions shows significant enhancement in MC effect compared to the pure BFO, which can be explained the suppression of spin cycloidal structure in BFO as a result of GMO substitution.

To establish the existence of intrinsic MD coupling, we carry out frequency dependent magnetoimpedance (MI) at RT. Figure 3.15 shows MI of BFO_{1-x}-GMO_x ($0.0 \leq x \leq 0.1$) solid solutions at 100 Hz and 1 kHz in forward and reverse magnetic field sweeps.

The change in MI was measured with and without magnetic field as: Z(H) = [Z(H)-Z(0)]/Z(0), where Z(H) is the impedance at the magnetic field H and Z(0) is the impedance at the zero magnetic field. BFO-GMO solid solution samples show significantly enhanced MI and magnetic hysteresis (Figure 3.15(b-e)) implying the existence of magnetodielectric coupling. The existence of magnetic hysteresis clearly indicates the presence of long-range magnetic ordering. The undoped BFO shows (Figure 3.15(a)) very small (2-3%) MI in forward magnetic field sweep at 2 T and 100 Hz and 1 kHz, while about 10% MI has been observed in reverse field sweep. Samples with x=0.025 (Figure 3.15(b)) shows about 50% MI in forward field sweep, whereas about 60% MI observed in reverse field sweep. Samples with x=0.05 and 0.075 show about 15 and 20% MI in forward and reserves field sweep, respectively. Samples with x= 0.025-0.075 (Figure 3.15(c-d)) show very similar MI behavior with frequency and magnetic hysteresis. Sample with x=0.10 (Figure 3.15(e)) shows about 4% MI in both forward and reverse field sweeps and the low MI effect can be explained due to the proximity of MPB. The observation of MC and MI at different frequencies clearly indicates the pres-

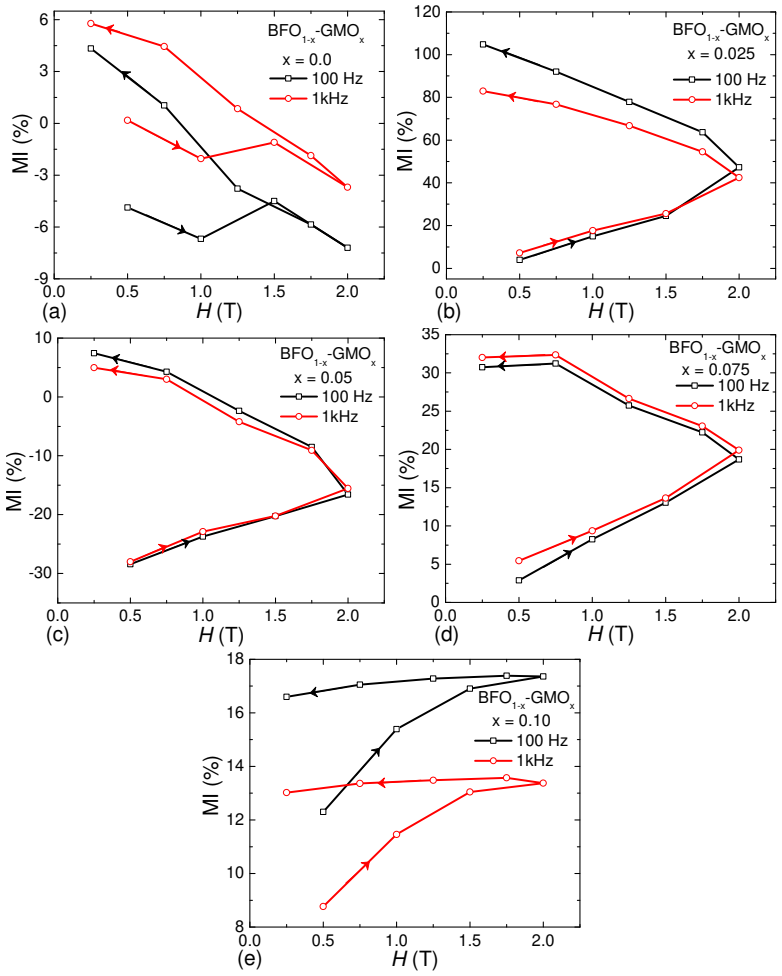

Figure 3.15: Magnetoimpedance (MI) of BFO_{1-x}-GMO_x with different percentage of x: (a) x = 0.0; (b) x = 0.025; (c) x = 0.05; (d) x = 0.075; (e) x = 0.10.

ence of enhanced magnetodielectric coupling in BFO-GMO solid solutions.

3.4 Summary

In summary, nanocrystalline solid solutions of BFO_{1-x}-GMO_x $0.0 \leq x \leq 0.2$ have been synthesized successfully by auto-combustion method. The analysis of structural property by Rietveld refinement showed the existence of morphotropic phase boundary at x=0.10, which is in agreement with the Raman spectroscopy

and HRTEM studies. The dielectric dispersion behavior fits very well with the modified Maxwell-Wagner model. The frequency dependent phase angle study showed the resistive nature of solid solutions at low frequency, whereas it showed capacitive behavior at higher frequencies. The temperature variation of dielectric permittivity showed dielectric anomaly at magnetic phase transition temperature and it was shifted towards the lower temperature with increasing GMO concentration indicating the lowering of magnetic phase transition towards lower temperature. The Nyquist plot showed the conduction mechanism is mostly dominated by grains and grain boundary resistance. The ac conductivity of all the samples followed the modified Jonscher model. The impedance and modulus spectroscopy showed a non-Debye like relaxation mechanism which can be modeled using a CPE in the equivalent circuit.The unsaturated ferroelectric polarization loops indicated the lossy ferroelectric behavior. The BFO-GMO solid solutions showed enhanced ferromagnetic-like behavior at RT. The observation of frequency dependent magnetocapacitance and magnetoimpedance clearly showed the existence of an intrinsic magnetodielectric coupling. The BFO_{1-x}-GMO_x solid solutions with x= 0.025-0.075 showed significantly high MC and MI compared to the pure BFO, which can be useful for practical device applications.

References

[1] Schmid H, Ferroelectrics **162** 317, (1994)

[2] Fiebig M Lottermoser T, Fröhlich D, Goltsev A V and Pisarev R V , Nature **419** 818, (2002)

[3] Wang J, Neaton J B, Zheng H, Nagarajan V, Ogale S B, Liu B, Viehland D, Vaithyanathan V, Schlom D G, Waghmare U V, Spaldin N A, Rabe K M, Wuttig M and Ramesh R, Science **299** 1719, (2003)

[4] Palai R, Katiyar R S, Schmid H, Tissot P, Clark S J, Robertson J, Redfern S A T, Catalan G, and Scott J F, Phys. Rev. B **77** 014110, (2008)

[5] Palai R, Schmid H, Scott J F and Katiyar R S, Phys. Rev. B **81** 064110, (2010)

[6] Palai R, Scott J F,and Katiyar R S Phys. Rev. B **81** 024115, (2010)

[7] Hur N, Park S, Sharma P A, Ahn J S, Guha S and Cheong S W, Nature **429** 392-395, (2004)

[8] Scott J 2007 Nat. Mater. **6** 256-257

[9] Pabst G W, Martin L W, Chu Y H, Ramesh R Appl. Phys. Lett. **90** 072902, (2007)

[10] Nagamuna H, Inoue Y and Okamura S Integrated Ferroelectrics **95** 242, (2007)

[11] Khomskii D, Physics **2** 20, (2009)

[12] Schrettle F, Lunkenheimer P, Hemberger J, Ivanov V Y, Mukhin A A, Balbashov A M and Loidl A, Phys. Rev. Lett. **102** 207208, (2009)

[13] Tripathy S N, Mishra K K, Sen S, Mishra B G, Pradhan D K, Palai R and Pradhan D K, J. Appl. Phys. **114** 144104, (2013)

[14] Tripathy S N, Pradhan D K, Mishra K K, Sen S, Palai R, Paulch M, Scott J F, Katiyar R S Pradhan D K, J. Appl. Phys. **117** 144103, (2015)

[15] Selbach S M, Tybell T, Einarsrud M and Grande T, Chem. Mater. **19** 6478, (2007)

[16] Tripathy S N, Mishra B G, Shirolkar M M, Sen S, Das S R, Janes D B, and Pradhan D K, Mater. Chem. Phys. **141** 423, (2013)

[17] Tripathy S N, *Ph. D Thesis* National Institute of Technology, Rourkela, (2014)

[18] Balzar D, J. Appl. Crystallogr. **28** 244, (1995)

[19] Subbarao E C Colloids and Surfaces A **133** 3-11, (1998)

[20] Negi P, Dixit G, Agrawal H M, Kumar H, Srivastava R C, Sati P C, Gupta V and Asokan K, Ferroelectrics **519** 200, (2017)

[21] Dar M A, Majid K, Batoo K M, and Kotnala R K, J. Alloy Compd. **632** 307-320, (2015)

[22] Rayssi C, Kossi S E, Dhahri J and Khirouni K, RSC Advances **8** 17139, (2018)

[23] Alkathy M, James Raju K C and Eiras J A, J. Phys. D: Appl. Phys. (2021)

[24] Iwamoto M, *Mawell-Wagner Effect* in Bhusan B. (Eds) *Encyclopedia of Nanotechnology* Springer, Dordrecht, (2015)

[25] Shen M, Ge S and Cao W, J. Phys. D: Appl. Phys. **34** 2935, (2001)

[26] Martinez, R, A Kumar, Palai R, Scott J F and Katiyar R S, J. Phys. D: Appl. Phys **44** 105302, (2011)

[27] Clausse M, Colloid Polym. Sci. **253** 10204, (1975)

[28] Kamiyoshi K I, Fujimura T and Yamakami T, Science reports of the Research Institutes, Tohoku University, Ser. A, Physics, chemistry and metallurgy, **19** 125-152, (1967)

[29] Martinez R, Palai R, Huhtinen H, Liu J, Scott J F and Katiyar R S Phys. Rev. B **82** 134104, (2010)

[30] Alkathy M S and James Raju K C, J. Mater. Sci: Mater Electron **27** 8957, (2016)

[31] Jonscher A K, Nature **264** 673, (1977)

[32] Pelaiz-Barramco A, Gutierrez-Amador M P, Huanosta A and Valenzuela R, Appl. Phys. Lett. **73** 2039, (1977)

[33] James A R, Prakash C and Prasad G, J. Phys. D: Appl. Phys. **39** 1635, (2006)

[34] Mahbood S, Prasad G and Kumar G S, Bull. Mater. Sci. **29** 347, (2006)

[35] Macdonald J R, J. Non-Cryst. Solids **210** 70, (1997)

[36] Das P S, Chakraborty P K, Behera B, Mohanty N K, Choudhary R N P, J. of Adv. Ceramics **3** 1, (2014)

[37] Jump F K, Prog. Solid-State **22** 111, (1993)

[38] Wang T H, Ding Y, Tu C S, Yao Y D, Wu K T, Lin T C, Yu H H, Ku C S and Lee H Y, J. Appl. Phys. **109** 07D907, (1993)

[39] Zhang J X *et al.*, Phys. Rev. Lett. **107** 147602, (2011)

[40] Park J W, Baek S H, Wu P, Winchester B, Nelson C T,Pan X O, Chen L Q, Tybell T and Eom C B, Appl. Phys. Lett. **97** 212904, (2010)

[41] Park T, Papaefthymiou G C, Viescas A J, Moodenbaugh A R and Wong S S, Nano Lett. **7** 766, (2007)

[42] Selbach S M, Tybell T, Einarsrud M, and Grande T, Adv. Mater. **20** 3692, (2008)

[43] Catalan G, Sardar K, Church N S, Scott J F, Harrison R J and Redfern S A T, Phys. Rev. B **79** 212415, (2009)

[44] Palai R, Huhtinen H, Scott J F and Katiyar R S, Phys. Rev. B **79** 104413, (2009)

[45] Dasari K, Wu J, Huhtinen H, Jadwisienczak W M and Palai R, J. Phys. D: Appl. Phys. **50** 175104, (2017)

[46] Dasari, Wang J, Guinel M J, Jadwisienczak W M, Huhtinen H, Mundle R, Pradhan A K and Palai R, J. Appl. Phys. **118** 125707, (2015)

[47] Anderson P W, Phys. Rev **115** 2, (1959)

[48] Anderson P W, Solid-State Phys **14** 99, (1963)

[49] Goodenough J B, Magnetism and the Chemical Bond, John Wiley and Sons, New York, (1963)

[50] Geertsman W and Khomskii, Phys. Rev. B **54** 3011, (1995)

[51] Raymond O, J. Appl. Phys. **97** 084107, (2005)

[52] Schmidt R, Ventura J, Langenberg E, Nemes N M, Munuera C, Varela M, Hernandez M, Leon C and Santamaria J, Phys. Rev. B **86** 035113, (2012)

[53] Gerhardt R, J. Phys. Chem. Solids **55** 1491, (1994)

[54] www.ameteksi.com/products/software/zsimpwin

[55] Sinclair D C and West A R, J. Appl. Phys. **66** 3850, (1989)

[56] Morrison F D, Sinclair D C and West A R, J. Appl. Phys. **86** 6355, (1999)

[57] Macdonald J R, Solid-State Ionics **176** 1961, (2005)

[58] Catalan G, Appl. Phys. Lett. **88**102902, (2006)

[59] Tang J, Feng L and Wiemann J A, Appl. Phys. Lett. **74** 2522, (1999)

Chapter 4

Conduction Mechanisms in BFO-GMO Multiferroics

In pure $BiFeO_3$ and all the combination of BFO_{1-x}-GMO_x was found that the transport mechanism is a Space-Charge-Limited mechanism. We performed our measurements in a temperature range from -173.15 - 226.85°C. We used the Fowler-Northeim Conduction Mechanism fitting, but it does not fit the data. The same happened with Schottky Barrier- and Pool-Frenkel-fitting. We have found in our previous work that the relaxation process occurring in our sample is of the kind of space charge polarization [1]. The charge carrier density and the general density of state decreases with increasing temperature but not the mobility of the samples suggesting a hopping mobility type of small polarons (A small polarons is an extra electron or a hole severely localized within a potential well that it creates by displacing the atoms that surround it) [2].

4.1 Introduction

Multiferroic materials offer great potential applications because of the combination of two or more ferroics properties like ferroelectricity, ferromagnetism and ferroelasticity [2–4]. Bulk $BiFeO_3$ is a single-phase multiferroic that has a very high ferroelectric (FE) transition (Curie temperature of 850°C) and weak antiferromagnetic (AFM) Neels-temperature (370°C) [5–8], it shows great promise because it can function at high temperature range [9,10]. Example of these appli-

cations are nonvolatile ferroelectric random-access memory, magnetic data storage, high-sensitivity ac magnetic field sensors and electrical tunable microwave devices like filters, oscillators and phase shifters [2,11,13]. We have to emphasize that $BiFeO_3$ is lead-free, and it will help to avoid toxicity in ferroelectric products. However, $BiFeO_3$ has a high leakage current density and it have been reported different conduction mechanisms in ion-substituted $BiFeO_3$ bulk and films. In recent years researchers have been trying to solve this problem by substitution of suitable elements at Bi/Fe-site of $BiFeO_3$ or to fabricate composites [14, 15]. Enhanced dielectric and magnetic properties of Gd-doped $BiFeO_3$ have been reported [16,17]. Not only Gd have been used, but rare-earth elements in general, because it helps to eliminate the impurity phase in $BiFeO_3$ materials and composites, and enhances its magnetic properties [18]. In our case we report the conduction mechanism behavior of $GdMnO_3$ doped $BiFeO_3$ with x = (0, 2.5, 5.0, 7.5, 10, 15 and 20%) synthesized by solid-state reaction technique. Because of the high conductivity in bulk $BiFeO_3$ it can be used to create a magneto-electric Access Memory (MERAM) [19] and integrated into microelectronic devices. [20] Ohmic-, Space charge conductivity- and Hopping-mechanism are present in all our samples and other conduction mechanism were not present because of the moderate field used.

The conduction mechanism found in the literature for $BiFeO_3$ and another similar perovskite are interface limited- (ILC) and bulk limited conduction (BLC). In Matsuo *et al* [21] Space Charge Limited Conductivity (SCLC) for $BiFeO_3$ and Ohmic conduction for BFMO was reported. Considering the fist one (ILC) we used the Schottky emission fitting. The dielectric constant values we extract from the slopes of these plots are three order of magnitude less than expected (ϵ_r= 0.028) and in our case is approximately ϵ_r=40 for this

sample in agreement with the literature [1, 22]. If the electronic mean free path in the insulator is less than the thickness of the dielectric film we have to fit Schottky emission modified for thicker samples [23], but we get the same result of the dielectric constant because the slope is the same as normal Schottky. Other possible mechanism was Fowler-Nordheim tunneling and we fitted this model to our data. Our temperature was not low enough for suppressing the thermionic emission. Therefore the thermionic emission is dominant at high temperature. [16] To identify electron effective mass and barrier height, is useful to measure the thermionic emission at high temperature and the tunneling current at low temperature, both at high electric field [18, 19]. In bulk limited conduction mechanism we fitted Ohmic conduction at low temperature and voltage, SCL-conduction at middle voltage, and at high voltage we fitted Pool-Frenkel (PFC) and Hopping conduction (HC). At high temperature we extract the hopping distance 2 microns (long-range hopping), the frequency of the thermal vibration (f=82MHz) and the effective mass m_{eff} which is similar to the mass of the electron(m_e) for 300, 400, and 500 K (m_{eff}= 1.036m_e). The effective mass and the mass of the electron being similar, is a result of the thickness of our samples (far beyond 4nm) [27,28], but it turned out that PFC does not describe the values of our data. In general we can read in the literature that in band to band transport the mobility is larger than 1cm^2/Vs, independent of electric field and decreases with increasing temperature while in hopping transport the mobility is smaller than 10^{-2}cm^2/Vs, depends on electric field and increases with increasing temperature. In our case the mobility is low, in order of 10^{-3}cm^2/Vs and inversely proportional to the temperature [16]. That means that the kind of mobility we have in our sample is a hopping mobility and of course a hoping transport and not a band transport. For semiconductors if the conductivity

$\sigma \geq 10^{-2}$ $\Omega^{-1}\text{cm}^{-1}$ is too conductive and for $\sigma \leq 10^{-8}\Omega^{-1}\text{cm}^{-1}$ is too insulating. Our samples values of the conductivity stay right between these values. We performed our measurement in a temperature range from 100-500 K.

4.2 Experimental details

The synthesis of nanoceramics solutions of BFO_{1-x}-GMO_x were made using analytical grade chemicals [1]. The whole process of self-combustion synthesis was described in the paper [1] and [3]. X-Ray line-profile analysis (XLPA) was used [14]. For getting the composition, the grain size and uniformity of the samples see Masso *et al* [1]. Dielectric parameter was measured at a wide range of frequency (100Hz - 1MHz) with the Hioki 3532-50 LCR. For the electrical characterization, the pellets were polished and silver paint was used for the electrodes. Then the silver paint was allowed to dry for 3 h at a temperature of 150°C. Current voltage measurement was carried out using the 2000 multimeter Keithley in a range of 0 - 100 volts. We varied the temperature using the Blue Wave temperature controller and the temperature variation was from 25 - 325°C for ac- and -175 - 225°C for dc-measurement.

4.3 Results and discussions

4.3.1 Current density and conduction mechanisms

In Figure 4.1 we can see the direct current (dc) behavior of the current density (J) vs electric field (E). All the samples showed a linear dependency of J vs E for low temperature and for high temperature-low electric field. In Figure 4.2 (a) we can see the ohmic-like behavior of the current at low voltage

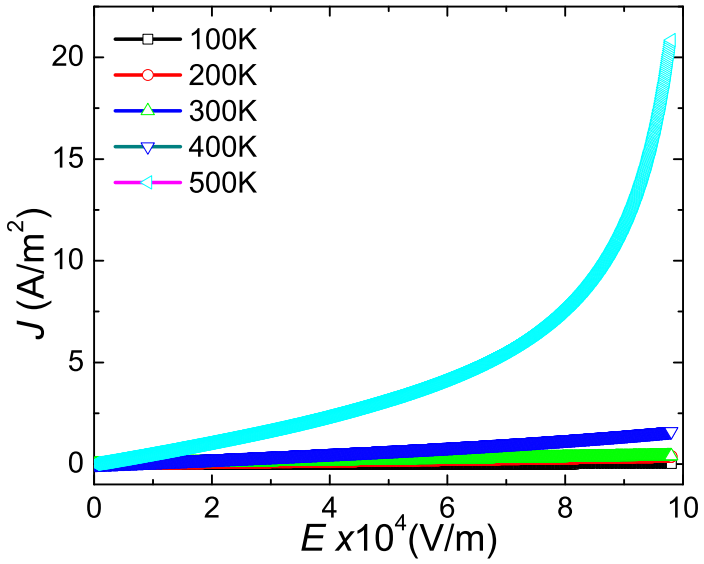

Figure 4.1: Current density vs Electric field in dc mode of BFO_{1-x}-GMO_x for x = 0.05.

(0-20V).

$$J = e\mu_0\eta E \tag{4.1}$$

For this ohmic-like behaviour the formula 4.1 was used for the fitting and calculation of the corresponding parameter. Where e is electron charge μ_0 is the mobility, η the carrier density and E the electric field. For higher electric field we found a linear behavior between J and E^2 (Figure 4.2 b) where we applied the formula 4.2 for the calculation of the mobility μ_0 where ϵ_s is the static dielectric permittivity (low frequency dielectric) and ϵ_0 is the dielectric permittivity in vacuum. Then we calculated the carrier density η of the samples at different temperatures with Ohm formula 4.1 (see Table 4.1). Using the extracted activation energy from the slope in Figure 4.5 and Figure 4.6 we calculated the general density of state of the charge carrier with the formula 4.6.

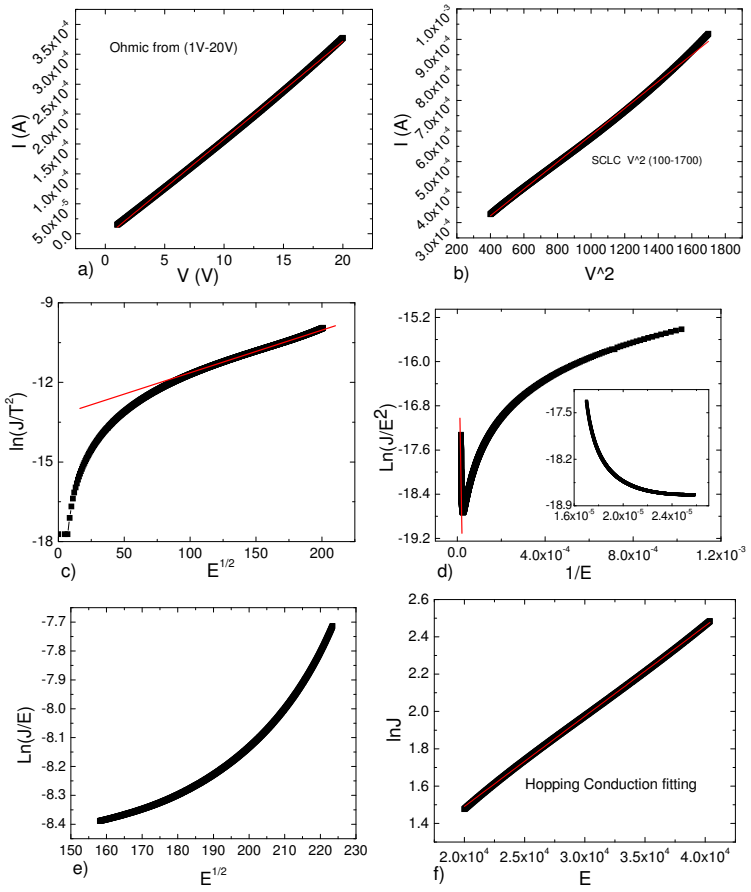

Figure 4.2: (a) Ohmic conductivity for low field; (b)SCL Conduction for higher field; (c) Schottky thermionic emission at very high field; (d) Fowler-Nordheim Conduction; (e) Pool-Frenkel conductivity; (f) Hopping conduction mechanisms for BFO_{1-x}-GMO_x.

$$J = (9/8)\mu_0\epsilon_s\epsilon_0 E^2/d \tag{4.2}$$

Other of the possible conduction mechanism is the Schottky emission. We fitted our data with the equation for Schottky emission [16]. Formula 4.3 describes this process.

$$J_{Sch} = A^* T^2 e^{\frac{-q(\Phi_b - \sqrt{\frac{qE}{4\pi\varepsilon_r\varepsilon_0}}))}{K_b T}} \tag{4.3}$$

where

$$A^* = \frac{4\pi q K_b^2 m^*}{h^3}$$

$$A^* = 120\frac{m^*}{m_0}$$

A* is the effective Richarson constant, m_0 the free electron mass, m^* the effective electron mass in the dielectric, $q\Phi_b$ the Schottky barrier high and

$$\varepsilon_r = \varepsilon_\infty = n^2$$

is the optic dielectric constant.

Plotting $ln(\frac{J}{T^2})$ VS $E^{1/2}$ we can extract the barrier high from the intercept, Figure 4.2 (c).

$$ln(\frac{J}{T^2}) = (\frac{-q\phi_b}{K_b T}) + \frac{\sqrt{\frac{q}{4\pi\varepsilon_r\varepsilon_0}}}{K_b T} E^{\frac{1}{2}}$$

The barrier high extracted from the plot is $\Phi_b = 0.57eV$ and the dielectric constant is $\varepsilon_r = 0.028$.

In Masso *et al.* and [22] the reported dielectric constant for $BiFeO_3$ at higher frequency is 40.

The difference of three order of magnitude between the calculated dielectric constant and the reported one, reveals that Schottky emission is not the appropriate conduction mechanism for our samples in spite of the barrier high obtained from the intercept of the plot being in range.

Simon *et al.* [23] indicated that if the electronic mean free path in the insulator is less than the thickness of dielectric film, the equation Standard Schottky emission must be modified because of the presence of traps to the Schottky mod-

ified emission, Formula 4.4. For $l < d$ we have:

$$J_{SchM} = \alpha T^{\frac{3}{2}} E \mu (\frac{m^*}{m_0})^{\frac{3}{2}}) e^{\frac{-q(\Phi_b - \sqrt{\frac{qE}{4\pi\varepsilon_r\varepsilon_0}})}{K_b T}} \tag{4.4}$$

Where

$$\alpha = 3 * 10^{-4} \frac{As}{cm^3 K^{3/2}}$$

and μ is the electronic mobility in the insulator. The other parameter are explained above.

In our case it does not make any difference with the normal Schottky equation, despite the thickness of our sample, since the slopes of both equations are the same, and it is from the slopes that the value of the dielectric constant is extracted.

For high electric field we fitted Fowler-Nordheim tunneling mechanism (Formula 4.5) reported in Yang *et al.* [17].

$$J_{FN} = \frac{q^2}{8\pi h \phi_b} E^2 e^{\frac{-8\pi(2qm_T^*)^{1/2}}{3hE} \phi_b^{\frac{3}{2}}} \tag{4.5}$$

where m_T^* is the tunneling effective mass in dielectric and h the Planck constant. To use this formula we need to do the measurement at very low temperature (less then 100 K). At such low temperature the thermionic emission is suppressed and the tunneling current is dominant. The linear curve is obtained from the plot (Figure 4.2 (d)) of: $ln(\frac{J}{E^2})$ vs $\frac{1}{E}$ and the slope is

$$slope = -6.83 * 10^7 \sqrt{\frac{m_T^*}{m_0} \phi_b^3}$$

,

If we want to know the electron effective mass and the barrier high in our

samples we measure the thermionic emission current at high temperature and the tunneling behaviour at low temperature but in both cases at high electric field [18, 19]. In our case the temperature range was not low enough and the electric field not high enough to use this method. At very high electric field some researchers have fitted the straight line marked in Figure 4.2 (d)) but in our case as we expanded the graph in these values of the electric field we do not get a straight line. See Figure 4.2 (d) insert. We determined that Fowler-Nordheim do not fit the experimental data (Figure 4.2 (d)).

We fitted Poole-Frenkel emission because this method is popular to identify the traps energy level in dielectric and a straight line is expected with the plot of $ln(\frac{J}{E})$ vs $E^{1/2}$, Figure 4.2 (e). In our case the fitting of our data do not give us the straight line for this kind of conduction. Therefore, our samples do not have a Poole-Frenkel conduction mechanism.

In Figure 4.2 (f) we can see the fitting of Hopping Conduction Mechanism for higher electric field. We get a straight line and from the fitting we have extracted, the hopping distance, the frequency of the thermal vibration (Formula 4.6) and with Formula (Formula 4.7) the effective mass of the electron.

$$J_h = qa\eta\nu e^{(\frac{qaE}{k_bT} - \frac{E_a}{k_bT})} \tag{4.6}$$

$$N_C = \frac{2(2\pi m^* k_b T)^{\frac{3}{2}}}{2^{\frac{5}{3}}\pi k_b T} \tag{4.7}$$

Where a is the mean hopping distance, η is the electron concentration in the conduction band, ν is the frequency of the thermal vibration of electron, and E_a the activation energy [16, 20]. The activation energy used in Formula 4.6 (E_a=0.74eV) comes from Figure 4.5 and Figure 4.6. All calculations were

carried out using our highest temperature (500 K) ensuring intrinsic conduction in the samples. We obtained a long-range hopping distance, from the slope of Formula 4.6, where $a = \frac{slope k_b T}{e} = 2\mu m$. The hopping distance a, of $2\mu m$, agrees with the average size of the grain. At the same time, the activation energy of 0.7 eV, necessary for the conduction process to occur, gives us an approximate electron wavelength of $2\mu m$. In this way, the average distance calculated between the traps is in accordance with the structural parameters and the value of the activation energy of our sample.

The charge carrier density $\eta = 1.91 * 10^{11} cm^{-3}$ from Formula 4.1 and the intercept value in the Formula 4.6 with y-axis allowed us to calculate the vibration frequency of the electrons in the traps that is $\nu = \frac{e^{\left(intercept + \frac{E_a}{k_b T}\right)}}{ea\eta} = 8.2GHz$. Formula 4.6 shows that the hopping current depends on the field energy Φ_E = qaE and the activation energy E_a. If $\Phi_E > E_a$, the hopping conduction decreases with increasing temperature [24] and when $\Phi_E < E_a$ the hopping conduction increases with the temperature. The graph of Figure 4.3 reveals that the conductivity increases with temperature. In our case, with E = 0.53 kV/cm we get Φ_E = 0.106 eV less than E_a = 0.74 eV.

4.3.2 Conductivity

Figure 4.3 shows that the value of direct conductivity increases on increasing temperature. The dc conductivity in pure $BiFeO_3$ go from $10^{-10}\Omega^{-1}cm^{-1}$ for 200K (-73°C) to $10^{-7}\Omega^{-1}cm^{-1}$ at 500K (225°C) and for BFO_{1-x}-GMO_x for x = 0.15% the values of the dc conductivity are between $10^{-7}\Omega^{-1}cm^{-1}$ for 200K and $10^{-3}\Omega^{-1}cm^{-1}$ for 500K. It also confirms the negative Temperature Coefficient Resistor (NTCR) behavior of the sample [24]. The conductivity increases considerably with $GdMnO_3$ doping and Gd substitution, which is due to the hop-

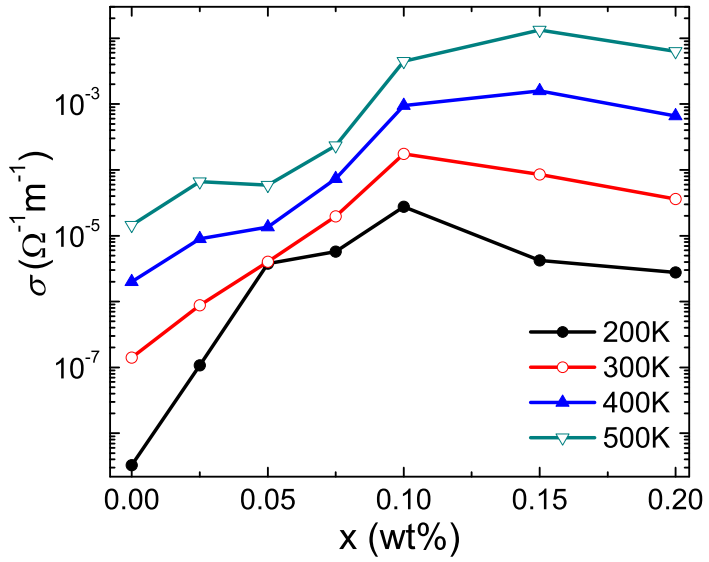

Figure 4.3: Direct conductivity vs concentration for all temperatures of BFO_{1-x}-GMO_x.

ping of charge carriers through available oxygen vacancies. In $GdMnO_3$ doped $BiFeO_3$ samples, the value of activation energy at evaluated temperatures shows a possible diffusion of oxygen ion vacancy through grain boundary [25].

Figure 4.4 displays a linear behavior of $\ln(\sigma_{ac}\text{-}\sigma_{dc})$ vs $\ln\omega^2$. This is an indicator, in small band gap semiconductors, that small polarons are involved in the carrier transport and this interaction facilitates the hopping conductivity in the sample [26]. In pure $BiFeO_3$ an electron-electron interaction is present, which makes it an electron material. In Mn_2O_3 the carrier interaction is an electron-phonon type, like the interaction seen in our samples of BFO_{1-x}-GMO_x [24, 27].

4.3.3 Activations energy and density of states

The graph in Figure 4.5 was used to determine the values of the Activation energies E_a of the samples using the Arrhenius equation of the resonance frequencies f_{max} (Relaxation Time τ) with the inverse of the temperature. For

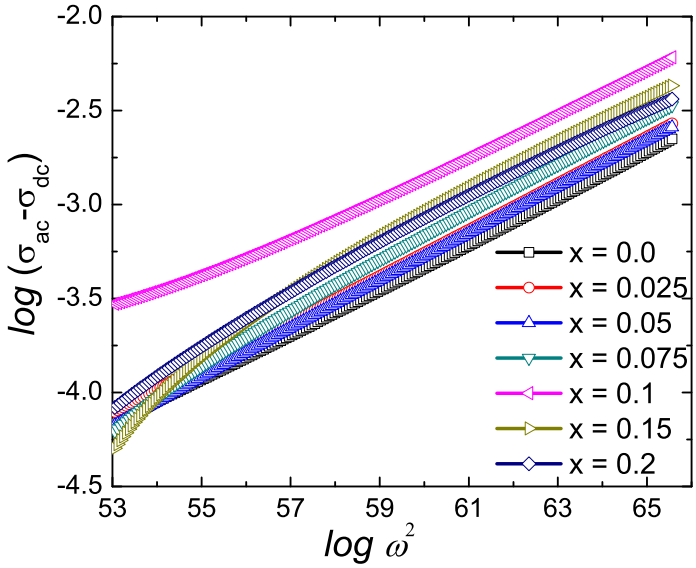

Figure 4.4: Linearity of log σ vs log ω^2 of BFO_{1-x}-GMO_x.

each temperature we extract f_{max} of the imaginary impedance vs frequency and we graphed τ=$1/f_{max}$ vs 1000/T to extract from the slope the E_a. The E_a of f_{max} is an indicator of how the polarization or orientation of the dipoles present in the material interact with the charge carrier. The greater the difference between E_a of f_{max} and E_a of the conductivity σ, bigger is the influence from the lattice polarization. This could be an indicator of the magneto-electric coupling of our samples.

Towards higher temperatures the conductivities σ(T) in Figure 4.6 merge into a frequency-independent curve, which represents the intrinsic dc conductivity. The activation energy for the intrinsic conductivity is frequency independent. The ac conductivity at low temperature, where the activation energy decreases with increasing frequency is frequency dependent. Therefore we can deduce a hopping type of carrier mobility. The conductivity in our sample is $6.31*10^{-3}\Omega^{-1}cm^{-1}$ for 550K (277°C), which is higher than the reported value

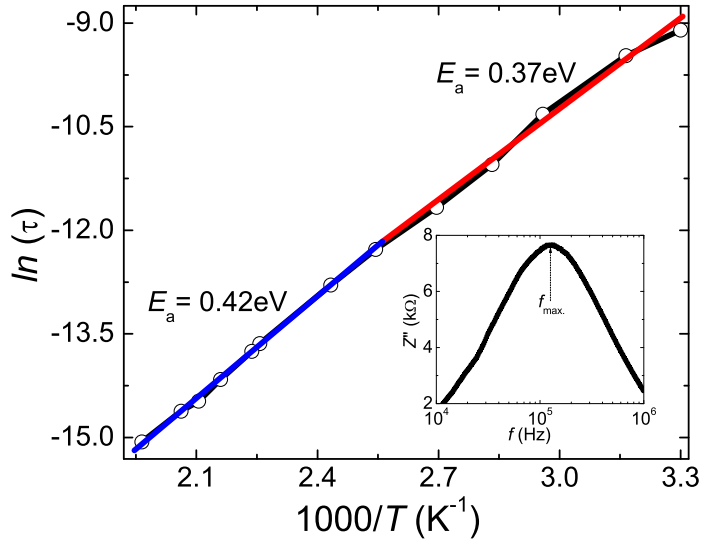

Figure 4.5: Activation Energy via relaxation time τ for high and low temperature of BFO_{1-x}-GMO_x for x = 0.05.

by Selbach*et al.* for pure BFO that is $10^{-5}\Omega^{-1}cm^{-1}$ close to the magnetic ordering temperature (370°C) [30]. Wefring *et al.* reported mobility in order $10^{-2}cm^2V^{-1}s^{-1}$ for 700°C [31]. In our BFO_{1-x}-GMO_x samples the mobility is less by one order of magnitude for 227°C (see Table 4.1). The hopping mobility increases with increasing temperature, therefore the mobility value of our BFO_{1-x}-GMO_x samples are in agreement with the literature.

Furthermore, the E_a calculated with both methods are very close for high temperatures but farther away for low temperatures and higher frequencies. This phenomena shows that hopping conductivity is predominant for low temperature and that a coupling between crystal and charge carrier exist, in other words magneto-electric coupling.

In Table 4.1 we can see how the free carrier density decreases and the carrier density of state in the conduction band (N_c) increases with increasing temperature. This process is described by Formula 4.8 where η is the free carrier density

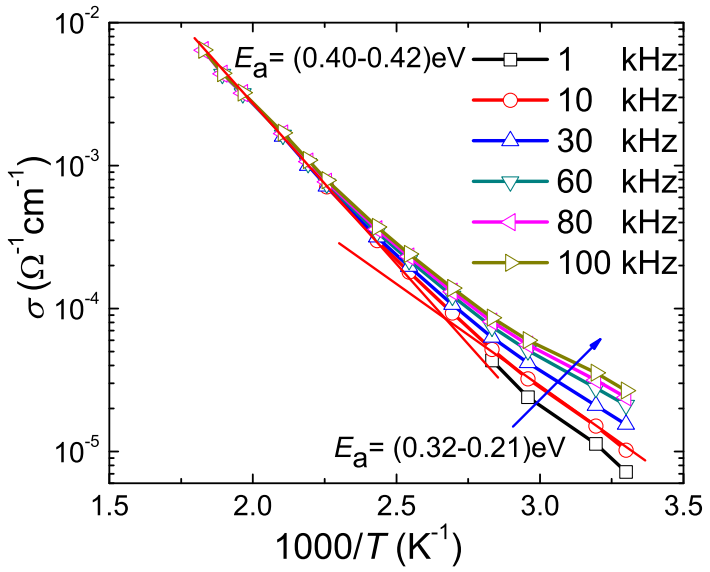

Figure 4.6: Activation energy via ac conductivity for different frequencies in BFO_{1-x}-GMO_x for x = 0.05.

Table 4.1: Density of state, charge carrier density, mobility, and effective mass.

Temp. (K)	N_s cm^{-3}	η cm^{-3}	μ_0 $cm^2V^{-1}s^{-1}$	$m*$ (m_e)
300	2.64*10^{19}	4.47*10^{11}	0.21*10^{-3}	1.035
400	4.07*10^{19}	2.54*10^{11}	1.23*10^{-3}	1.036
500	5.69*10^{19}	1.91*10^{11}	5.76*10^{-3}	1.036

E_a the activation energy, k_b the Boltzman constant and T the temperature in Kelvin. Despite this, the carrier density do not change in order of magnitude with temperature but with the Mn concentration in the sample. The oxygen vacancies form energy level 0.6 eV below the conduction band (CB) [9]. In our case the activation energies varies from E_a= (0.61 - 0.74)eV. At the same time the mobility of the samples increases with temperature suggesting a hopping type of mobility. In our case, we have already confirmed that hopping conduction mechanism is the relevant one for high electric field.

$$\eta = N_c e^{(-E_a/k_b T)} \tag{4.8}$$

4.3.4 Dielectric properties

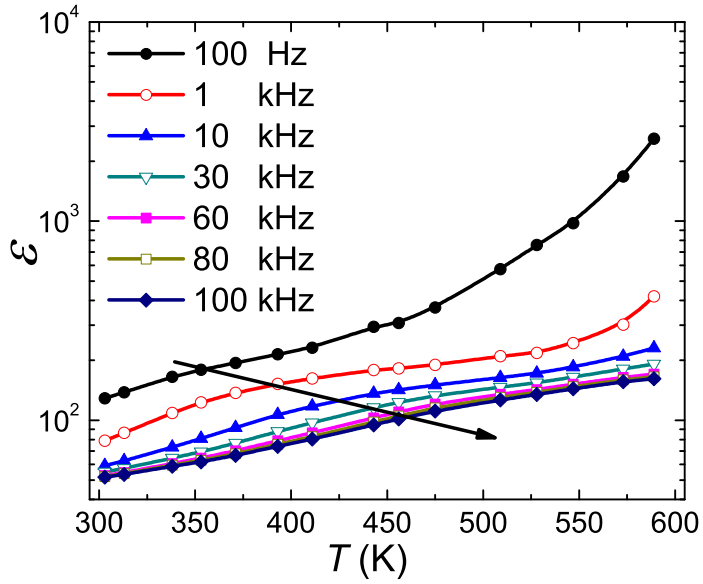

Figure 4.7: Dielectric vs Temperature for different frequencies in BFO_{1-x}-GMO_x for x = 0.05.

The dielectric constants measured are dominated by Maxwell-Wagner like effects for temperatures T>25°C and frequencies below 1 M*Hz*. The increasing of the dielectric with temperature reveals that the phase transition is over 600K (325°C) for all sample composition and with increasing temperature it will take more time to charge the capacitor for all frequencies. At lower temperatures the temperature dependence of the dielectric constant and loss reveals no anomalies outside the experimental errors, indicating the lack of phase transitions [41]. Our measurements were in the range of 300-575K (25-302°C). The dielectric increases with increasing temperature and with decreasing frequency responding to a normal dielectric behaviour. At RT the dielectric constant has values between 36

and 74 for concentrations x = 0.0 and x = 0.1 respectively [1]. The loss is high and frequency dependent indicating a predominance of hopping conductivity.

4.4 Summary

We can conclude that the transport mechanisms in our samples respond very strongly to an Ohmic-like conduction mechanism for low electric field, space charge limited current mechanism for moderate electric field, and hopping conduction mechanism for high electric field. We have interaction between the charge carrier and the crystal and a formation of small polarons are present. We demonstrated a hopping mobility and a very high loss in all the samples. The activation energies decreases with increasing frequencies because of the decrease in loss energy of the samples.

References

[1] R. Masso, S.N. Tripathy, F. A. Aponte, D. K. Pradhan, R. Martinez, and R. Palai, Materials Research Express, (2021)

[2] D. Emin, Physics Today, 35, 6, (1982)

[3] S. Pattanayak, R. Choudhary and R. Das, Journal Of Advanced Dielectric,4,2, (2014)

[4] T. Zhao, A. Scholl, F. Zavaliche, K. Lee, M. Barry, A. Doran, M. Cruz, Y. Chu, C.Ederer, N. Spalding, R. Das, D. Kim, S. Baek, C. Eom and R. Ramesh,Nat. Mater. 5, 823 (2006)

[5] R. Ramesh and N. Spaldin, Nat. Mater. 6, 21 (2007)

[6] S. Karimi, I. M. Reaney and Y. Han, J. Mater. Sci.44, 5102 (2009)

[7] S. Satpathy, N. Mohanty, A. Behera, K. Patra, B Behera and P. Nayak, Front. Mater. Sci., 7 295, (2013)

[8] S. Kiselev, R. Ozerov, and G. Zhdanov, Soviet Physics Doklady. 7 742, (1963)

[9] N. Spaldin, S. Cheong and R. Ramesh, Physics Today 63 38, (2010)

[10] Z. Zhong and H. Ishiwara, Appl. Phys. Lett. 95, 112902 (2009)

[11] G. Smolenskii and I. Chupis, Sov. Phys. Usp. 25, 475 (1982)

[12] J. Rehspringer, J. Bursik, D. Niznansky and A. Klarikova, J. Magn. Magn. Mater. 211, 291 (2000)

[13] A. Mousse, J. Herbert,(Chapman and Hall, London), p.390 (1990)

[14] J. Xu, G. Wang and Y. He, Mater. Lett. 63, 855 (2009)

[15] M. Vopsaroiu, M. Cain, G. Sreenivasulu, G. Srinivasan and A. Balbashov,Mater. Lett. 66, 282 (2012)

[16] A. Julian, S. Dalber and B. Elisa, J. Phys.: Conf. Series 200, 012134 (2010)

[17] A. Lahmar, S. Habouti, M. Dietze, C. Solterbeck and M. Es-Souni, Appl. Phys. Lett. 94,012903 (2009)

[18] F. Kubel and H. Schmid Acta. Crystallogr. B 46 698 (1990)

[19] M. Bibes and A. Barthlmy, Nature Mater 7425 (2008)

[20] G. Catalan and J F Scott, Adv. Mater. 21 2463 (2009)

[21] H. Matsuo, Y. Kitanaka, Y. Noguchi, M. Miyayama, J. of Asian Ceramic Sosieties, (2015)

[22] S. Godara, N. Sinhaa, G. Ray, B. Kumar, Journal of Asian Ceramic Societies 2, 416421, (2014)

[23] J. Simmons, Physical Review Letters, vol. 15, no. 25, pp. 967968, (1965)

[24] Fu. Chiu, Advances in Materials Science and Engineering, ID 578168, (2014)

[25] F. Chiu, Journal of Applied Physics, vol. 100, no. 11,Article ID 114102, 5 pages, (2006)

[26] D. Schroder, John Wiley and Sons, New York, NY, USA, 2nd edition, (1998)

[27] M. Stadele, F. Sacconi, A. Di Carlo, and P. Lugli, Journal of Applied Physics, vol. 93, no. 5, pp. 26812690, (2003)

[28] B. Brar,G. Wilk, and A. Seabaugh, Applied Physics Letters, vol. 67, no. 7, pp. 10311033, (1995)

[29] G. Pabst, L. W. Martin, Y. Chu, and R. Ramesh, Appl. Phys. Lett. 90, 072902 (2007)

[30] S. N. Tripathy, K. K. Mishra, S. Sen, B. G. Mishra, Dhiren K. Pradhan, R. Palai and D K. Pradhan, J Appl Phys 114, 144104 (2013)

[31] S. N. Tripathy, B. G. Mishra, M. M. Shirolkar, S. Sen, S. R. Das, D. B. Janes, and D. K. Pradhan, Mater. Chem. Phys. 141, **423** (2013)

[32] D. Balzar, J. Appl. Crystallogr. 28, **244** (1995)

[33] W. Brandt and J. Reinheimer, Physical review B, Vol2, 8, (1970)

[34] A. Floris,S. de Gironcoli, E. K. U. Gross, and M. Cococcioni, Phy.Rev B 84, 161102(R) (2011)

[35] S. Pattanayak, R. N. P. Choudhary and P. R. Das, J. Mater. Sci.: Mater. Electron. 24, 2767 (2013)

[36] C. Ang, Z. Yu and L. E. Cross,Phys. Rev. B 62, 228 (2000)

[37] H. Yang, M. Jain, N. Suvorova, H. Zhou, H. Luo, D. Feldmann,P. Dowden, R. DePaula, S. Foltyn, and Q. Jia, Appl. Phys. Lett. 91, 072911 (2007)

[38] F. Chiu, C. Lee, and T. Pan, Journal of Applied Physics, vol. 105, no. 7, Article ID 074103, 4 pages, (2009)

[39] S.M. Selbach, T. Tybell, M.-A. Einarsrud, T. Grande, Adv. Mater. 20, 3692 (2008)

[40] E. T. Wefring, M.-A. Einarsrud and T. Grande, Phy. Chem. Chemical Phy.17,9420-9428 (2015)

[41] J. Lu,A. Gunther,F. Schrettle, F. Mayr,S. Krohns, P. Lunkenheimer, A.Pimenov,V.D. Travkin,A.A. Mukhin, and A. Loidl,Eur. Phys. J. B 75, 451460 (2010)

Chapter 5

Conduction Mechanisms in BFO-DMO Multiferroics

In our sample BFO_{1-x}-DMO_x we have found a hopping conduction mechanism for higher electric field. We carried out our measurements in a temperature range of -173.15 - 226.85°C. We fitted Fowler-Northeim Conduction Mechanism, but it is not a good fit. The same happened with Schottky Barrier- and Pool-Frenkel-fitting. The hopping distance (a = 0.45μm.) and the frequency (ν = 59.3*$10^{12} Hz$) of the thermal vibration of the electron was calculated. We have found that the hopping conduction increases with the temperature. Our samples shows a Negative Temperature Coefficient Resistance NTCR behavior and the conductivity increases with Dy substitution which showed a possible diffusion of oxygen ion vacancy through the grain boundary. In our fittings of the Jonscher power law we demonstrated a localized kind of hopping in agrement with the results obtained for the conduction mechanism of the samples.

5.1 Introduction

Throughout this thesis we have defined the importance of $BiFeO_3$ in applications of novel multifunctional devices [1–11]. Tripathy *et al.* reported a study of the phase transition of BFO-DMO. This study shows a decrease in magnetic ordering temperature with increasing Dy doping as well as an increase in magnetization with $DyMnO_3$ substitution. We determined the conduction mechanism

of BFO_{1-x}-DMO_x and calculated the mean hopping distance and the thermal vibration frequency in the traps. After fitting Schottky emission, Fowler-Nordheim, and other well known mechanism we have found that at low temperatures and low voltage the mechanism that describes the conduction is an ohmic-like type mechanism. At medium voltages Space Charge Limited conduction and at high voltages Hopping Conduction mechanisms were detected. The conductivity in our sample is $10^{-3}\Omega^{-1}cm^{-1}$ for 370K which is higher than the value reported by Selbach *et al.* for pure $BiFeO_3$. On the other hand we can see how the activation energy (E_a), calculated with both methods has different values for both, low and high temperatures. This phenomena reveals that hopping conductivity is predominant for all temperatures, and a coupling between crystal and charge carrier do exist (magneto-electric coupling). We demonstrated that the general relaxation time increases with increasing $DyMnO_3$ concentration.

5.2 Experimental details

The synthesis of the samples of BFO_{1-x}-DMO_x were made using high purity chemicals. The description of the whole synthesis can be found in papers [1] and [3]. X-Ray line-profile analysis (XLPA) was used [14].

We followed a previously reported procedure to determine the composition, the grain size and uniformity of the samples [15].

The condition of all the experimental characterization was the same for all materials composition described in previous chapter for BFO_{1-x}-GMO_x.

5.3 Results and discussions

5.3.1 Current density and conduction mechanisms

Figure 5.1 shows the direct current (dc) behavior of the current density J vs electric field E. The behavior of all BFO_{1-x}-DMO_x samples are, for relatively low electric fields, similar to the result of BFO_{1-x}-GMO_x samples already reported in the previous chapter. In the samples we report herein, the linear dependency of J vs E for low temperature and any value of the electric field, and for high temperature but low electric field, is shown. That behavior is a ohmic-like one and Formula 5.1 was used for the fitting and calculation of the different parameters like the mobility and carrier density. Figure 5.2 (a) shows the ohmic-like behavior of the current at low voltage (0 - 50V) (Formula 5.1).

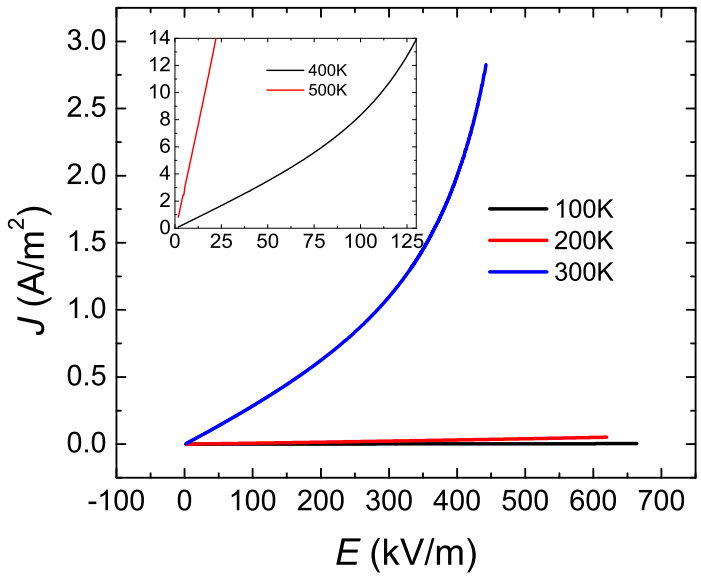

Figure 5.1: Current density vs electric field in dc mode of BFO_{1-x}-DMO_x for x = 0.1.

$$J = e\mu_0\eta E \tag{5.1}$$

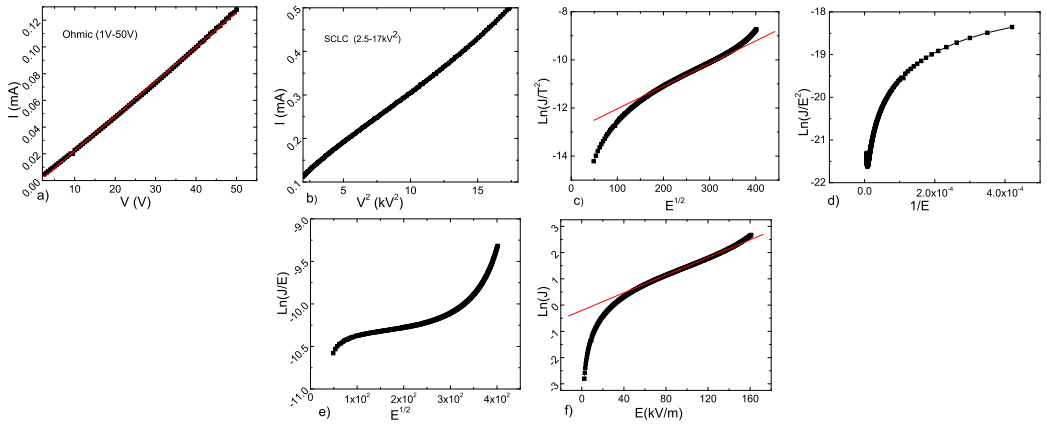

Figure 5.2: (a) Ohmic-like conductivity for low field; (b) SCL conduction for higher field; (c) Schottky thermionic emission at very high field; (d) Fowler-Nordheim conduction; (e) Pool-Frenkel conductivity; (f) Hopping conduction mechanism for BFO_{1-x}-DMO_x.

Where e is electron charge μ_0 is the mobility, η the carrier density and E the electric field. In these samples we also found similarities with the BFO_{1-x}-GMO_x samples from the previous chapter. For higher electric field we found a linear behavior between J and E^2 (Figure 5.2 (b)) where we applied Formula 5.2 for the calculation of the mobility μ_0. Where ϵ_s is the static dielectric permittivity (low frequency dielectric) and ϵ_0 is the dielectric permittivity in vacuum. Then we calculated the carrier density η of the samples at different temperatures using Formula 5.1 (see Table 5.2). Using the activation energy extracted from the slope in Figure 5.6 and Figure 5.7 we calculated the density of state of the charge carrier using Formula 5.8.

$$J = (9/8)\mu_0\epsilon_s\epsilon_0 E^2/d \tag{5.2}$$

Another possible conduction mechanism is the Schottky emission.

We fitted our data using the previously reported equation for Schottky emission [16], Formula 5.3.

$$J_{Sch} = A^* T^2 e^{\frac{-q(\Phi_b - \sqrt{\frac{qE}{4\pi\varepsilon_r\varepsilon_0}}))}{K_b T}} \tag{5.3}$$

where

$$A^* = \frac{4\pi q K_b^2 m^*}{h^3}$$

$$A^* = 120\frac{m^*}{m_0}$$

A* is the effective Richarson constant, m_0 the free electron mass, m^* the effective electron mass in the dielectric, $q\Phi_b$ the Schottky barrier high and

$$\varepsilon_r = \varepsilon_\infty = n^2$$

is the optic dielectric constant.

Plotting $log(\frac{J}{T^2})$ vs $E^{1/2}$ the barrier high from the intercept can be extracted, Figure 5.2 (c).

$$ln(\frac{J}{T^2}) = (\frac{-q\phi_b}{K_b T}) + \frac{\sqrt{\frac{q}{4\pi\varepsilon_r\varepsilon_0}}}{K_b T} E^{\frac{1}{2}}$$

The fitting in the graph shown in Figure 5.2 (c) is not linear. Therefore we can discard Schottky thermionic emission as the conduction mechanism for our BFO_{1-x}-DMO_x samples.

For high electric field we fitted Fowler-Nordheim tunneling mechanism (Formula 5.4) reported in Yang *et al.* [17].

$$J_{FN} = \frac{q^2}{8\pi h\phi_b} E^2 e^{\frac{-8\pi(2qm_T^*)^{1/2}}{3hE}\phi_b^{\frac{3}{2}}} \tag{5.4}$$

where m_T^* is the tunneling effective mass in dielectric, and h the Planck

constant. This formula requires the measurement to be performed at very low temperatures (less then 100K).

The thermionic emission is suppressed and the tunneling current is dominant at such low temperatures. The linear behaviour of $ln(\frac{J}{E^2})$ vs $\frac{1}{E}$ is shown in Figure 5.2 d).

and the slope is:

$$slope = -6.83 * 10^7 \sqrt{\frac{m_T^*}{m_0}\phi_b^3}$$

To determine the electron effective mass and the barrier high in our samples we need to measure the thermionic emission current at high temperature, and the tunneling behaviour at low temperature, in both cases at high electric field [18, 19].

In our case the temperature range was not low enough and the electric field not high enough to use this method.

At very high electric field, as shown in Figure 5.2 (d), we did not get a straight line. Therefore, Fowler-Nordheim conduction mechanism is not present in our samples.

We fitted Poole-Frenkel emission because this method is popular to identified the traps energy level in dielectric, and a straight line was expected with the plot of $ln(\frac{J}{E})$ vs $E^{1/2}$, Figure 5.2 (e). In our case the fitting of the data did not showed a straight line for this kind of conduction. Therefore, the samples do not have a Poole-Frenkel conduction mechanism.

Figure 5.2 (f) shows the fitting of Hopping Conduction Mechanism for higher electric field. A straight line is obtained, and from the fitting of the hopping equation the hopping distance was extracted 5.5. Using the diffusion equation, the frequency of the thermal vibration and using Formula 5.6 the effective mass

of the electron were determined.

$$J_h = qa\eta\nu e^{(\frac{qaE}{k_bT} - \frac{E_a}{k_bT})} \tag{5.5}$$

$$ln(J_h) - ln(qa\eta\nu) = (\frac{qa}{k_bT})E - (\frac{E_a}{k_bT})$$

$$N_C = \frac{2(2\pi m^* k_b T)^{\frac{3}{2}}}{2^{\frac{5}{3}}\pi k_b T} \tag{5.6}$$

Where a is the mean hopping distance, η is the electron concentration in the conduction band, ν is the frequency of the thermal vibration of electron, and E_a the activation energy [16, 20]. We used the activation energy E_a= 0.99eV from Figure 5.7.

All calculation were performed using the highest temperature (400 K). This way we considered intrinsic conduction in our samples. From the slope we obtained a long-range hopping distance $a = \frac{slope k_b T}{e} = 0.45\mu m$, and from the intercept we have $\nu = \frac{e^{\left(intercept + \frac{E_a}{k_b T}\right)}}{ea\eta} = 59.3 * 10^{12} Hz$ in the traps.

Formula 5.5 reveals that the hopping current depends on the field energy Φ_E = qaE and the activation energy E_a. If $\Phi_E > E_a$, the hopping decreases with increasing temperature [23] and when $\Phi_E < E_a$ the hopping conduction increases with the temperature. The graph in Figure 5.3 shows that the conductivity increases with temperature and for our samples, with E = 1,5kV/cm we get Φ_E = 0.10 eV less than E_a = 0.99 eV.

5.3.2 Conductivity

Figure 5.3 shows that the value of direct conductivity increases on increasing temperature, the same behavior we found in BFO_{1-x}-GMO_x. The dc conductiv-

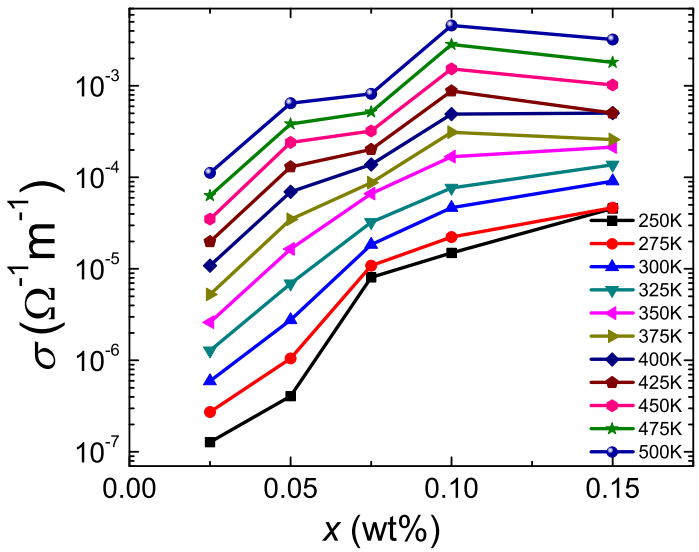

Figure 5.3: Direct conductivity vs concentration for all temperature of BFO_{1-x}-DMO_x.

ity in pure $BiFeO_3$ goes from $10^{-7}\Omega^{-1}cm^{-1}$ for 250K to $10^{-4}\Omega^{-1}cm^{-1}$ at 500K and for BFO_{1-x}-DMO_x for x = 0.10% the values of the dc conductivity are between $10^{-5}\Omega^{-1}cm^{-1}$ for 250K and $10^{-3}\Omega^{-1}cm^{-1}$ for 500K. It also confirms the Negative Temperature Coefficient Resistance (NTCR) behavior of the sample [24]. The conductivity increases with $DyMnO_3$ doping and Dy substitution, which is due to the hopping of charge carriers through available oxygen vacancies. In $DyMnO_3$ doped $BiFeO_3$ samples, the value of activation energy, at evaluated temperatures, shows a possible diffusion of oxygen ion vacancy through grain boundary [25].

Figure 5.4 shows for higher frequencies a linear behavior of $\ln(\sigma_{ac}\text{-}\sigma_{dc})$ vs $\ln\omega^2$. This is an indicator in small band gap semiconductors that small polarons are involve in the carrier transport at high frequencies and this interaction facilitates the hopping conductivity in the sample [26]. In pure $BiFeO_3$ we find an electron-electron interaction, so it is an electron material and in Mn_2O_3 an

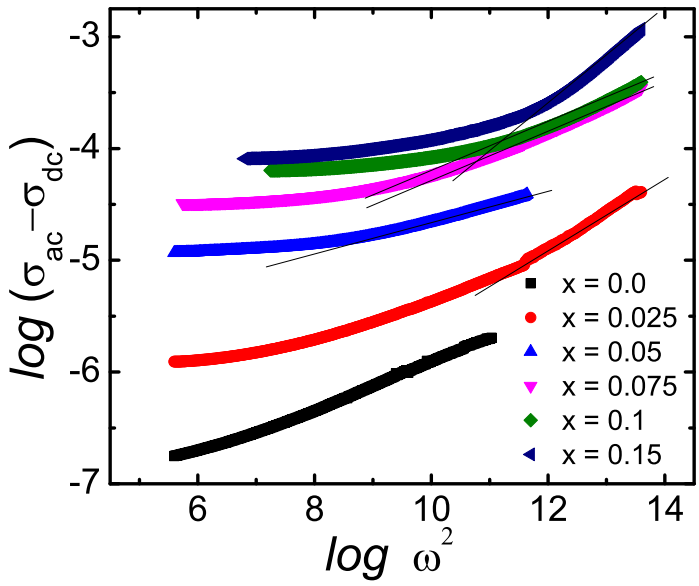

Figure 5.4: Linearity of log σ vs log ω^2 of BFO_{1-x}-DMO_x.

electron-phonon interaction like the interaction seen in our samples of BFO_{1-x}-DMO_x but only for high frequencies [24, 27].

Figure 5.5 shows the frequency behavior of conductivity of all samples at room temperature. We fitted the Jonscher power law [28] to define the different parameters that describe the kind of conductivity of our sample. The equation that describe the Jonscher power law is the Formula 5.7, where σ_{ac} is the total conductivity, σ_{dc} is the frequency independent conductivity, and the coefficient A and exponent n are temperature and material intrinsic property dependent. According to Funkel *et al.* [29] the samples have localized hopping. The value of the fitting parameters are in Table 5.1. The dispersion parameter n increases with increasing concentration x in BFO_{1-x}-DMO_x.

$$\sigma_{ac}(\omega) = \sigma_{dc} + A\omega^n \tag{5.7}$$

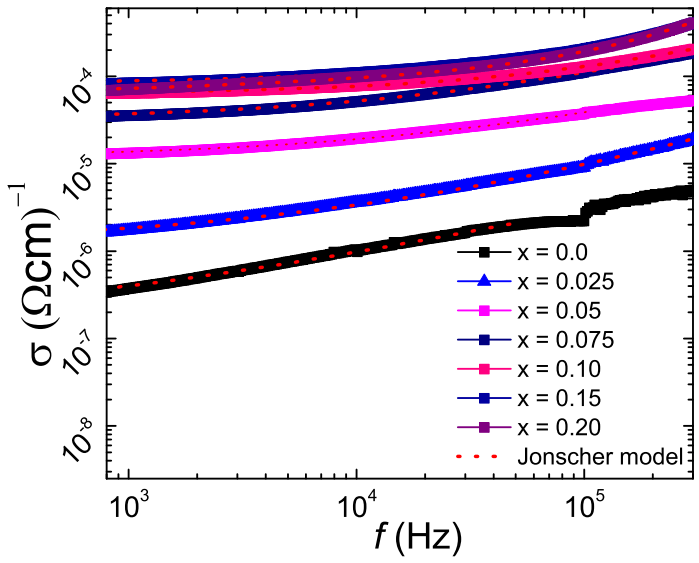

Figure 5.5: Power law of conduction for BFO_{1-x}-DMO_x.

Table 5.1: Fitted parameters of Jonscher power law

x	σ_{dc}	A	n
0.0	1.60*10^{-7}	9.22*10^{-10}	0.54
0.025	1.16*10^{-6}	5.91*10^{-10}	0.67
0.05	1.18*10^{-5}	6.21*10^{-9}	0.57
0.075	3.27*10^{-5}	1.28*10^{-8}	0.60
0.1	6.36*10^{-5}	3.57*10^{-9}	0.69
0.15	8.19*10^{-5}	3.31*10^{-10}	0.95
0.2	9.30*10^{-5}	1.14*10^{-10}	1.00

5.3.3 Activations energies and density of state

In Figure 5.6 we have calculated the values of the activation energies E_a of the samples with the Arrhenius equation of the resonance frequencies f_{max} (Relaxation Time τ) with the inverse of the temperature. For each temperature we extracted f_{max} of the imaginary impedance vs frequency and we made a graph of τ=1/f_{max} vs 1000/T to extract from the slope the E_a. The E_a of f_{max} is an indicator of how the polarization or orientation of the dipoles present in the

material interact with the charge carrier. The larger the difference between E_a of f_{max} and E_a of the conductivity σ, the bigger is the influence from the lattice polarization.

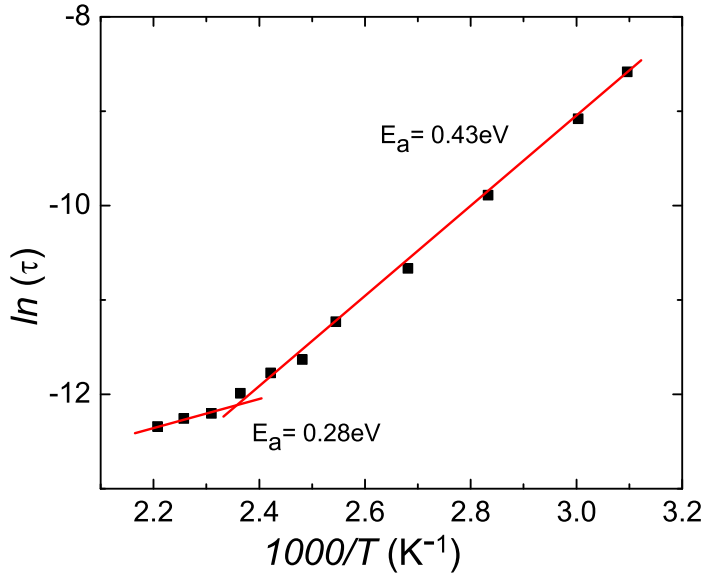

Figure 5.6: Activation Energy via relaxation time τ for high and low temperature of BFO_{1-x}-DMO_x for x = 0.1.

Towards higher temperatures the conductivities σ(T) in Figure 5.7 merge into a frequency-independent curve, which represents the intrinsic dc conductivity. That effect is not so well defined as in BFO_{1-x}-GMO_x. The graph shows how for the intrinsic conductivity the activation energy is almost frequency independent but not for the ac conductivity at low temperature. At low temperature the activation energy decreases with increasing frequency. Therefore, we can deduce a hopping type of carrier mobility. This confirms the type of conductivity we have obtained from the power law fitting. The conductivity in our sample is $10^{-3}\Omega^{-1}\text{cm}^{-1}$ for 370K (97°C) and is higher as the pure BFO reported by Selbach *et al.* who found a value of the conductivity $10^{-5}\Omega^{-1}\text{cm}^{-1}$ close to the

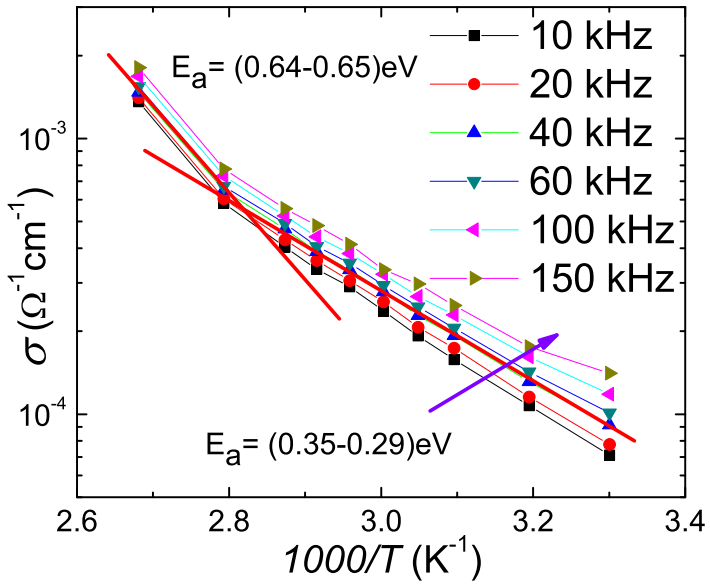

Figure 5.7: Activation energy via ac Conductivity for different frequencies in BFO_{1-x}-DMO_x for x = 0.1.

magnetic ordering temperature (640K or 367°C) [30].

Mobility in order $10^{-2}cm^2V^{-1}s^{-1}$ for 700°C was reported in Wefring *et al.* [31]. In our BFO_{1-x}-DMO_x samples the mobility is two orders of magnitude larger than the one reported by Wefring for 227 *C 227°C (see Table 5.2).

The hopping mobility increases with increasing temperature. Therefore, the mobility value in BFO_{1-x}-DMO_x samples are in agreement with the literature.

On the other hand we can see how the activation energy E_a, calculated with both methods have different values for low and high temperatures. This phenomena reveals that hopping conductivity is predominant for all temperatures and a coupling between crystal and charge carrier exist (magneto-electric coupling).

Table 5.2 shows how the free carrier density decreases and the carrier density of state in the conduction band (N_c) increases with increasing temperature. This process is described by the equation 5.8 where η is the free carrier density, E_a the activation energy, k_b the Boltzman constant, and T the temperature in Kelvin.

Table 5.2: Density of state, charge carrier density, mobility, and effective mass.

Temp. (K)	N_c cm^{-3}	η cm^{-3}	μ_0 $cm^2V^{-1}s^{-1}$	$m*$ (m_e)
300	$0.72*10^{20}$	$3.64*10^{12}$	0.91	2.69
400	$1.11*10^{20}$	$1.61*10^{12}$	30.09	1.51

Despite this, the carrier density does not change in order of magnitude with temperature, but with the Mn concentration in the sample. The oxygen vacancies form energy level 0.6 eV below the conduction band (CB) [9]. In our case the activation energies varies from E_a = (0.93-0.10)eV. At the same time the mobility of the samples increases with temperature, suggesting a hopping type of mobility. Hopping conduction mechanism prevails in our samples for high electric field.

$$\eta = N_c e^{(-E_a/k_b T)} \tag{5.8}$$

5.3.4 Dielectric properties

The dielectric constants measured are dominated by Maxwell-Wagner like effects for room temperature and frequencies below 1 MHz. The dielectric values increases with increasing concentration [x] for different frequencies. The dielectric has a local minimum for Sample 5 (x = 0.10). At this concentration the sample is no more a single-phase material. For these concentration the samples reveals two phases, one for $BiFeO_3$ and the other for $DyMnO_3$. The loss is high and frequency dependent indicating a predominance of hopping conductivity.

Figure 5.9 shows that for low frequencies the samples behave like a perfect resistor but for higher frequencies the phase angle takes negative values like a capacitor.

Figure 5.10 shows how the BFO_{1-x}-DMO_x dielectric decreases inversely proportional to the frequency. This behavior is characteristic of a ferroelectric. To

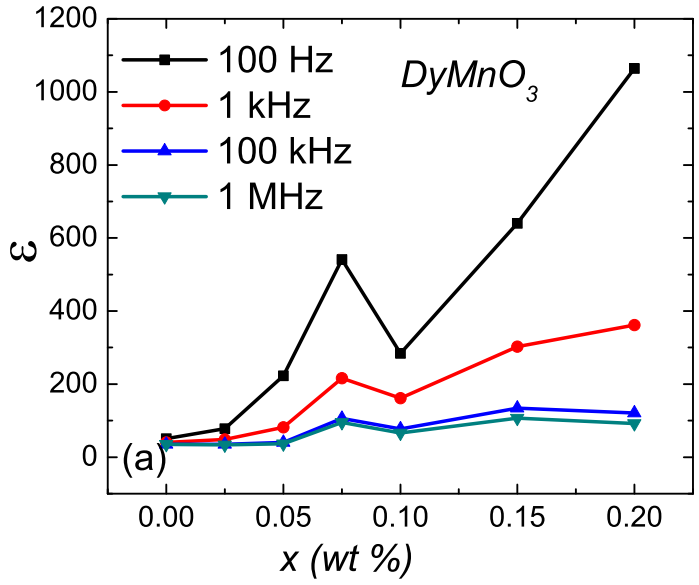

Figure 5.8: Dielectric vs $DyMnO_3$ concentration for different frequencies in BFO_{1-x}-DMO_x.

obtain the total relaxation time of the sample, data adjustments were made with different models. The Maxwell-Wagner modified model (MWM) is the one that describes the behavior of the data with greater precision.

$$\epsilon'(f) = \epsilon_\infty + \tfrac{1}{2}(\epsilon_s - \epsilon_\infty)b + Af^{-n} \tag{5.9}$$

and

$$b = 1 - \frac{sinh[(1-\alpha)ln(2\pi f\tau)]}{cosh[(1-\alpha)ln(2\pi f\tau + sin(\frac{1}{2}\alpha\pi))]},$$

From the fitting of MWM the parameters in Table 5.3 were taken.

Where x is the concentration, ϵ_s is the dielectric constant at low frequencies, ϵ_∞ is the dielectric constant at high frequencies, α is the measure of the polydispersity of the system [32, 33], τ is the total relaxation time, and n the dispersion parameter of frequency. Table 5.3 shows how the general relaxation time increases with increasing concentration x.

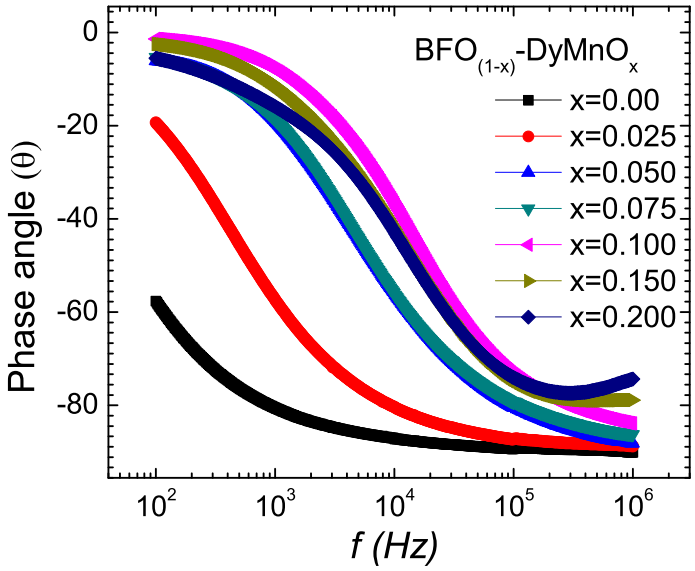

Figure 5.9: Phase angle vs frequency in BFO_{1-x}-DMO_x.

Table 5.3: Maxwell-Wagner modified values

x	ϵ_s	ϵ_∞	α	n	τ(ms)
0.0	220	37	0.43	0.59	0.19
0.025	78	33	0.50	1.0	0.65
0.05	81	27	0.61	1.0	0.02
0.075	186	90	0.50	0.8	0.03
0.1	191	65	0.43	1.0	0.05
0.15	347	113	0.41	1.0	0.06
0.2	355	106	0.28	0.9	0.08

5.4 Summary

Our research group has achieved an improvement in the multiferroic properties of $BiFeO_3$ by doping it with $DyMnO_3$, improving the piezoelectric, magnetic and magnetoelectric properties. We studied the solid solution BFO_{1-x}-GMO_x and its conduction mechanisms in this material that has an improvement in the magnetoelectric properties of its parents BFO and DMO. The magnetic ordering

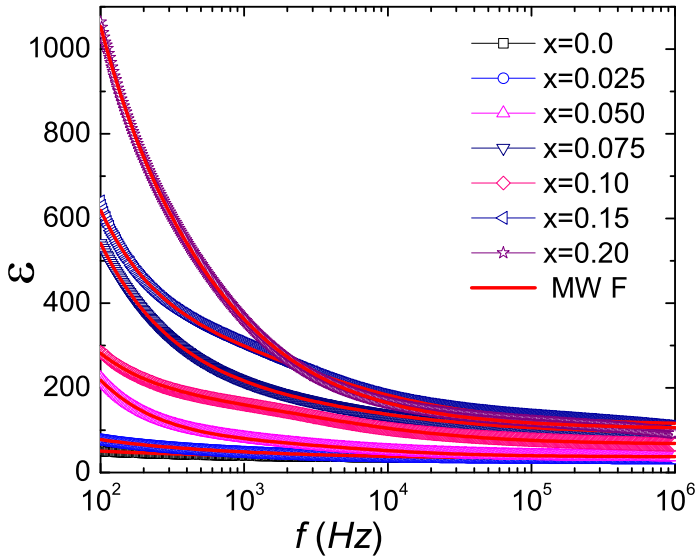

Figure 5.10: Maxwell Wagner fitting vs frequency in BFO_{1-x}-DMO_x.

temperature T_N in our samples decreases with increasing DMO doping. The conduction mechanism in our samples is an ohmic-like one at low temperature and voltage. At medium electric field the samples have a Space Charge Limited conduction with a conductivity of $10^{-3}\Omega^{-1}\text{cm}^{-1}$ for 370K (97°C). The samples have couplings between crystal structure and charge carrier causing a hopping conductivity through all temperatures and electrical fields. The activation energies decreases with increasing frequencies because of the decrease in loss energy of the samples.

References

[1] R. Masso, S.N. Tripathy, F. A. Aponte, D. K. Pradhan, R. Martinez, and R. Palai, (2021)

[2] S. Pattanayak, R. Choudhary and R. Das, Journal Of Advanced Dielectric,4,2, (2014)

[3] T. Zhao, A. Scholl, F. Zavaliche, K. Lee, M. Barry, A. Doran, M. Cruz, Y. Chu, C.Ederer, N. Spalding, R. Das, D. Kim, S. Baek, C. Eom and R. Ramesh,Nat. Mater. 5, 823 (2006)

[4] R. Ramesh and N. Spaldin, Nat. Mater. 6, 21 (2007)

[5] S. Karimi, I. M. Reaney and Y. Han, J. Mater. Sci.44, 5102 (2009)

[6] S. Satpathy, N. Mohanty, A. Behera, K. Patra, B Behera and P. Nayak, Front. Mater. Sci., 7 295, (2013)

[7] S. Kiselev, R. Ozerov, and G. Zhdanov, Soviet Physics Doklady. 7 742, (1963)

[8] N. Spaldin, S. Cheong and R. Ramesh, Physics Today 63 38, (2010)

[9] Z. Zhong and H. Ishiwara, Appl. Phys. Lett. 95, 112902 (2009)

[10] G. Smolenskii and I. Chupis, Sov. Phys. Usp. 25, 475 (1982)

[11] J. Rehspringer, J. Bursik, D. Niznansky and A. Klarikova, J. Magn. Magn. Mater. 211, 291 (2000)

[12] S. N. Tripathy, K. K. Mishra, S. Sen, B. G. Mishra, Dhiren K. Pradhan, R. Palai and D K. Pradhan, J Appl Phys 114, 144104 (2013)

[13] S. N. Tripathy, B. G. Mishra, M. M. Shirolkar, S. Sen, S. R. Das, D. B. Janes, and D. K. Pradhan, Mater. Chem. Phys. 141, **423** (2013)

[14] D. Balzar, J. Appl. Crystallogr. 28, **244** (1995)

[15] S. N. Tripathy, Dhiren. K. Pradhan, K. K. Mishra, S. Sen, R. Palai, M. Paulch, J. F. Scott, R. S. Katiyar, and Dillip K. Pradhan, J.Appl. Phys. 117, 144103, (2015)

[16] Fu. Chiu, Advances in Materials Science and Engineering, ID 578168, (2014)

[17] H. Yang, M. Jain, N. Suvorova, H. Zhou, H. Luo, D. Feldmann,P. Dowden, R. DePaula, S. Foltyn, and Q. Jia, Appl. Phys. Lett. 91, 072911 (2007)

[18] F. Chiu, Journal of Applied Physics, vol. 100, no. 11,Article ID 114102, 5 pages, (2006)

[19] D. Schroder, John Wiley and Sons, New York, NY, USA, 2nd edition, (1998)

[20] F. Chiu, C. Lee, and T. Pan, Journal of Applied Physics, vol. 105, no. 7, Article ID 074103, 4 pages, (2009)

[21] A. Khler and H. Bssle. Wiley-VCH Verlag GmbH and Co. KGaA, Boschstr. 12, 69469 Weinheim, German,(2015)

[22] M. Pope and C.E. Swenberg, Electronic Processes in Organic Crystals and Polymers, Monographs on the Physics and Chemistry of Materials, 2nd edn, Oxford University Press, Oxford,(1999)

[23] F. Chiu, W. Chiang, Materials, , 8, 5795-5805 (2015)

[24] S. Pattanayak, R. N. P. Choudhary and P. R. Das, J. Mater. Sci.: Mater. Electron. 24, 2767 (2013)

[25] C. Ang, Z. Yu and L. E. Cross,Phys. Rev. B 62, 228 (2000)

[26] W. Brandt and J. Reinheimer, Physical review B, Vol2, 8, (1970)

[27] A. Floris,S. de Gironcoli, E. K. U. Gross, and M. Cococcioni, Phy.Rev B 84, 161102(R) (2011)

[28] A.K. Jonscher, Nature 264, 673, (1977)

[29] Funke K. Jump. Prog Solid-State Ch 1993, 22: 111195, (1993)

[30] S.M. Selbach, T. Tybell, M.-A. Einarsrud, T. Grande, Adv. Mater. 20, 3692 (2008)

[31] E. T. Wefring, M.-A. Einarsrud and T. Grande, Phy. Chem. Chemical Phy.17,9420-9428 (2015)

[32] M. Clausse, Colloid Polym. Sci. 253 10204 (1975)

[33] K. I. Kamiyoshi, T. Fujimura, T. Yamakami, Science reports of the Research Institutes, Tohoku University. Ser. A, Physics, chemistry and metallurgy, 19, pp 125-152, (1967)

Chapter 6

Conclusion and Future Work

$BiFeO_3$ (BFO) is one of the rarest and Pb-free multiferroics at RT, however, it shows weak ME and MD coupling. In order to enhance the ME coupling, in the present work BFO1-x-GMOx and BFO1-x-DMOx solid solutions with different concentrations (x= 0.0, 0.05, 0.075, 0.1, 0.15, and 0.2) were systematically investigated.

In this thesis, we report the synthesis and suitable approach to improve the magnetoelectric (ME) coupling of $BiFeO_3$ by fabrication of BFO_{1-x}-GMO_x and BFO_{1-x}-DMO_x solid solutions for $0.0 \leq x \leq 0.2$ by auto-combustion method. The materials have been systematically characterized and examined to study the possibility of the compositional driven structural phase transition and its correlation with the ME coupling. Detail of the structural, microstructural, thermal, dielectric, ferroelectric, magnetic, magneto-dielectric and magneto-impedance properties has been shown in the light of the bring down of magnetic ordering temperature of $BiFeO_3$ towards room temperature as a function of $GdMnO_3$ and $DyMnO_3$ concentration. [1–6] The dielectric and electrical properties as a function of the magnetic field indicated the signature of ME coupling in samples with increased $GdMnO_3$ and $DyMnO_3$ composition, suggesting an optimization of functional properties of lead-free doped $BiFeO_3$. In pure $BiFeO_3$ and all the combinations of BFO_{1-x}-GMO_x and BFO_{1-x}-DMO_x the transport mechanism is a Space-Charge-Limited mechanism and a Hopping kind of conductivity for higher voltage and temperature. We carried out our I-V measurement in a temperature range from 100 - 500 K.

This study determined that the relaxation process occurring relaxation process occurring in our samples are of the kind of space charge Polarization. The charge carrier density and the density of state decreases with increasing temperature but not the mobility of the samples suggesting a hopping mobility type of small polarons in BFO_{1-x}-GMO_x and in BFO_{1-x}-DMO_x .

BFO-GMO (x = 0.025, 0.05, and 0.075) and BFO-DMO (x = 0.05) showed enhanced ME effect compared to the pure BFO. We conclude that the present work was somewhat successful in enhancing the ME coupling in BFO, hence achieved our main objectives. For all the practical applications, devices need to be in thin film form. [7–12]

As future work, we propose to grow BFO_{1-x}-GMO_x and BFO_{1-x}-DMO_x thin films by pulsed laser deposition (PLD). We are convinced that the thin films will show strong and enhanced magnetoelectric effect. PLD technique will maintain the stoichiometry of bulk material in the thin film. The most important thing would be the study of the mismatch (strain effect and epitaxial effect) between the different substrates and our material and how this affects the electrical and magnetoelectric characteristics in the thin film.

References

[1] S. N. Tripathy, K. K. Mishra, S. Sen, B. G. Mishra, Dhiren K. Pradhan, R. Palai and D K. Pradhan, J Appl Phys 114, 144104 (2013)

[2] S. N. Tripathy, Dhiren K. Pradhan, Karuna K. Mishra, Shrabanee Sen, Ratnakar Palai, Marian Paulch, J. F. Scott, RS. Katiyar and D K. Pradhan. J Appl Phys 117, 144103 (2015)

[3] S. N. Tripathy, B. G. Mishra, M. M. Shirolkar, S. Sen, S. R. Das, D. B. Janes, and D. K. Pradhan, Mater. Chem. Phys. 141, **423** (2013)

[4] F. Schrettle, P. Lunkenheimer, J. Hemberger, V. Yu. Ivanov, A. A. Mukhin, A. M. Balbashov, and A. Loidl, Phys. Rev. Lett. 102, 207208 (2009)

[5] C.H. Yang, T.Y. Koo and Y.H. Jeong, Solid-State Communications 134, 299 (2005)

[6] S. M. Selbach, T. Tybell, M. Einarsrud, and T. Grande, Chem. Mater.19, 6478 (2007)

[7] M. Fiebig, T. Lottermoser, D. Meier and M. Trassin, Nature Reviews Materials, Vol 1, 16046 (2016)

[8] W. Eerenstein, N. D. Mathur and J. F. Scott, Nature, Vol 442, 17 (2006)

[9] D. Pang, C. He, X. Li, S. Han,S. Pan, X. Long,Ceramics International 42, 9347-9353 (2015)

[10] M.M. Kumar, A. Shrinivas, S.V. and Suryanarayana. J Appl Phys 87, 85562 (2000)

[11] T.L. Ivanova and V.V. Gagulin. Ferroelectrics 10, 265:2416 11 (2002)

[12] V.S. Sunder, A. Halliyal, A.M. Umarji. J Mater Res 10, 13016 (1995)